Integrated Subharmonic Planar Schottky Diode Mixers for Submillimetrewave Applications

Rollin, Jean Marc

Award date:
2006

Awarding institution:
University of Bath

Integrated Subharmonic Planar Schottky Diode Mixers for Submillimetre-wave Applications

Jean Marc Rollin

A thesis submitted for the degree of Doctor of Philosophy

University of Bath
Department of Physics
November 2006

(on the engine 2007

ProQuest LLC
789 East Eisenhower Parkway
P.O. Box 1346
Ann Arbor, MI 48106-1346

Abstract

The growing demand for submillimetre wave (SMW) circuits is spurred not only by the needs of traditional science applications such as radio astronomy and atmospheric remote sensing but also by military and commercial applications such as compact range radar. Several approaches to device and circuit fabrication have been developed and in the past 20 years, many successful SMW components have been built for operation up to THz frequencies. However, they all suffer one or more drawback, such as low reliability and repeatability, lengthy and difficult assembly and reliance on mechanical tuners. The first part of the work described here has been the development of high yield, high quality and high repeatability antiparallel Schottky diodes entirely fabricated at the University of Bath. After producing Schottky diodes having state of the art characteristics, the main focus of the research was the development of a process to monolithically integrate the anti-parallel Schottky diode in a 200 GHz RF mixer circuit. Throughout this research, advantage has been taken of the recent development of advanced computer aided design tools that are suitable for simulating both linear and nonlinear parts of the submillimetre mixer to design and fabricated a fixed-tuned integrated mixer at 183 GHz.

Acknowledgements

I would like to thank Dr. Steve Davies for offering me the opportunity to conduct my research work within his group. His guidance, support, friendship and passionate conversation on wine and football made this challenging journey much easier.

I would also like to thank the department of Physics, especially to Tim Von Sel, Wendy Lambson, Barry Chapman, Bob Draper for their help and their kindness.

I would like to thank Byron Alderman and the entire group at the Rutherford Appleton for they valuable help in the measurement and characterisation of my different diodes and mixers. I would like to give a special recognition to Bertrand Thomas and Alain Maestrini for their invaluable time and help in training me in their state-of the-art simulation technique for the simulation of Schottky diodes and mixer design.

Obviously, a great thank you to "My Homeboys" Greg and Antonio who were always there to share friendship, hard work and good times. Thank you guys it was a blast.

J aimerais remercier ma famille, ma maman, Jean-Pierre ma soeur Sandrine et mon frère Brice pour avoir toujours été là à mes cotés et de m'avoir offert leur soutien et leur amour tout au long de mes études. Merci d'avoir crue en moi et à mes rêves de devenir un jour un physicien quand tout le monde avait dès ma jeune enfance renoncée a la possibilité que je puisse faire des longues études.

Finally I would like to dedicate this thesis to my wife Gisa and my sons Kenji and Keo. Gisa, thank you for giving me the love, inspiration and strength during all those years and for letting me fulfilled my dreams. Thank you for your support when I was spending most of my weeks days and nights at the University. I love you and I love the family we have built together. This thesis is for you and the kids.

CHAPTER INDEX

Chapter 1

Introduction

The growing demand for millimetre wave (MMW) and submillimetre-wave (SMW) electronic devices is spurred by the needs of radio astronomy, atmospheric remote sensing and compact range radar. These applications require broadband and sensitive receivers demonstrating high reliability and repeatability, easy fabrication and assembly and high operating frequencies. The aim of this chapter is first to present in detail the existing and future applications which require high quality mixers. Section 1.2 explores the different technologies needed to fabricate a complete receiver system. Finally the objectives and summary of the rest of this thesis are presented.

1.1 Applications of Heterodyne receivers at MMW and SMW

The millimetre- and submillimetre-wave region spans from 300 GHz to 3 THz. This region is often described as the most scientifically useful yet the least explored region of the electromagnetic spectrum. This section reviews the main applications operating at THz frequencies.

1.1.1 Radio Astronomy

Spectroscopy and remote sensing at terahertz frequencies have been for more than 25 years the sole niche applications in the millimetre and submillimetre region. These applications have been the main drivers to improve the design, performance and quality of receivers. Receivers for radio astronomy must have high spectral resolution, large instantaneous bandwidth and the best possible sensitivity, therefore often requiring cryogenically cooled detectors.

Submillimetre-wave spectroscopy can be used to study spectral lines occurring due to rotational transitions of simple non-symmetric molecules such as ^{12}CO, ^{13}CO, HCO^{+}, CN and others found in interstellar medium. These molecules are generally sparse and found only in trace quantities in interstellar clouds mainly composed of hydrogen. Analysis of the spectral line structure can be used to determine temperature, density and motions of the material making up the molecular cloud. A number of submillimetre telescopes are in operation such as the James Clerk

Maxwell Telescope (JCMT) [1.1] and the Caltech Submillimeter Observatory in Hawaii, along with those under construction, e.g. the Atacama Large Millimeter Array (ALMA)[1.2].

The JCMT is the world's largest facility designed specifically to make observations in the submillimetre region of the spectrum. At an altitude of 4092 m, near the summit of Mauna Kea, Hawaii, it is above 97 % of the water held in the atmosphere. The facility operates instruments in four frequency bands, A (215 – 275 GHz), B (318 – 373 GHz), C (430 – 510 GHz) and D (630 – 710 GHz). Most of the heterodyne observations are concerned with the early stages of star formation, including formation rate, planets not yet formed from dust disks and extragalactic observations.

The Atacama Large Millimeter Array (ALMA) is an international project to develop in the Chile's Andes Mountains a telescope array to study the universe. The array consists of an astronomical interferometer formed from 50 movable antenna dishes, each measuring 12 m wide. At its largest configuration the array will be equivalent to a telescope varying from 150 m to 14 km enabling astronomers to zoom in and out on different parts of the universe. The receivers will cover frequencies from 31.3 to 950 GHz with 10 separate bands. The initial priority will be made on the band-3 84 to 116 GHz, band-6 211 to 275 GHz, band-7 275-373 GHz and band-9 602 to 720 GHz, before covering a continuous spectrum. A correlator will combine all the information received from the antennas and will be able to process 1.6×10^{16} operations per second. For operation of a coherent interferometer, a phase stable reference signal, the local oscillator, has to be distributed. ALMA generates the mm-wave and submm-wave local oscillator reference by phase locking the difference frequency from two infrared lasers, distributed to the different antennas via optical fibres. ALMA is the largest ground based telescope project for the next decade. The first measurements are scheduled to start in 2008 and the entire system completion is scheduled for 2011.

Several space missions are planned by ESA and NASA to carry heterodyne receivers for detection of submillimetre wavelength radiation through astronomical observations. HERSCHEL, to be launched in early 2007, will observe the formation of galaxies and stars and the chemical composition of the Earth's atmosphere. PLANCK, to be launched with HERSCHEL, will map the Cosmic Microwave

Background with improved sensitivity and test inflationary models of the early universe. The space-borne Far InfraRed and Submillimetre Telescope (FIRST) is planned for launch in 2007 and carries the Heterodyne Instrument for FIRST (HIFI). This will cover at least the frequency range 492 GHz to 1113 GHz and will provide sensitive observations with resolving powers ranging from less than $5 \times 10^5 - 1.2 \times 10^7$. The instrument is optimised for the measurement of weak, broad spectral lines of distant galaxies and for performing fast line surveys of galactic objects [1.3].

1.1.2 Atmospheric Remote Sensing

There are many applications in the millimetre-wave to observe the Earth and its atmosphere. The first analyses were acquired by Cosmos 243, a Russian satellite launched in 1968. It was able to scan frequencies at 3.5, 8.8, 22.2 and 37 GHz to measure the concentration of water vapour in the atmosphere. In 1987, the first near 100 GHz receiver was launched with the SSM/I project (Special Sensor Microwave Imager). It was able to detect the wind speed on the surfaces of the oceans, the concentration and type of ice, and soil humidity. The observation frequencies were at 19.4, 22.3, 37 and 85.5 GHz. All these systems had the advantage over IR measurements of being able to work in any type of weather conditions.

Heterodyne receivers have been used to monitor the global distribution of both ozone O_3 and chlorine monoxide (ClO), which is a rate-limiting molecule in ozone destruction.

There are two methods employed for observing and attaining this data. The first option is by looking vertically through the atmosphere from ground based receivers. e.g. French Observatory in Bordeaux to study the ozone concentration at 100 GHz.

The second method is by looking tangentially through the upper atmosphere with varying inclination, using satellite based receivers.

The latter method (known as limb-sounding), is a proven choice for observations investigating chemical and physical processes involved in ozone depletion and other reactions caused by air pollution. Many spectral lines that are observable at high altitude are not visible to ground based telescopes. The altitudes range over which these measurements are made is typically 15-85 km. In NASA's Upper Atmosphere Research Satellite (UARS), a multi-channel instrument (63, 183 and 205 GHz) is designed to measure ClO (25-45 km), O_3 (15-80 km) and H_2O (15-85 km) combined with pressure calculated from O_2 emission [1.4]. The European Submillimetre-wave

Atmospheric Sounder (SUMAS) has been operated on board a research aircraft at 10 km. This instrument is equipped to measure, amongst others, the ClO molecular emission line at 649 GHz [1.5, 1.6, 1.7]

European Space Agency (ESA) remote sensing projects using submillimetre receivers MASTER, using a 1-m-diameter antenna covering frequency bands up to 500 GHz, and SOPRANO, using a 2.2 m diameter antenna covering frequency bands up to 950 GHz, will observe various atmospheric species including H_2O, O_3, HNO_3, ClO, BrO.

1.1.3 Chemical and Biological Warfare Agent Detection

Terahertz technology is still waiting for a mass-market application. A possible first step in this direction comes from the defence market. In a paper by Woolard [1.8], terahertz spectroscopy is discussed with defensive military applications in mind.

The recent proliferation of chemical and biological agents as instruments of warfare and terrorism has led the US Department of Defence to show considerable interest in the development of early warning systems for these agents. An adequate defence would necessitate the ability to rapidly detect and identify both known and unknown threat agents. Fig. 1.1 shows a block layout of a ground- or air-based active sensor looking at a cloud of dry bio-particles.

Very recent spectroscopic studies at millimetre- and submillimeter-wave have indicated that DNA (and possibly other cellular material) possesses large numbers of unique resonances due to localised phonon modes. Data is presented in [1.8] showing that in the 300-750 GHz frequency range, unique contributions are visible from these localised phonons, arising from DNA base-pair interactions. These contributions are absent from far infrared data. Technological challenges must be met before terahertz early warning systems are viable but considerable advancement of the terahertz field would almost certainly result from military backing.

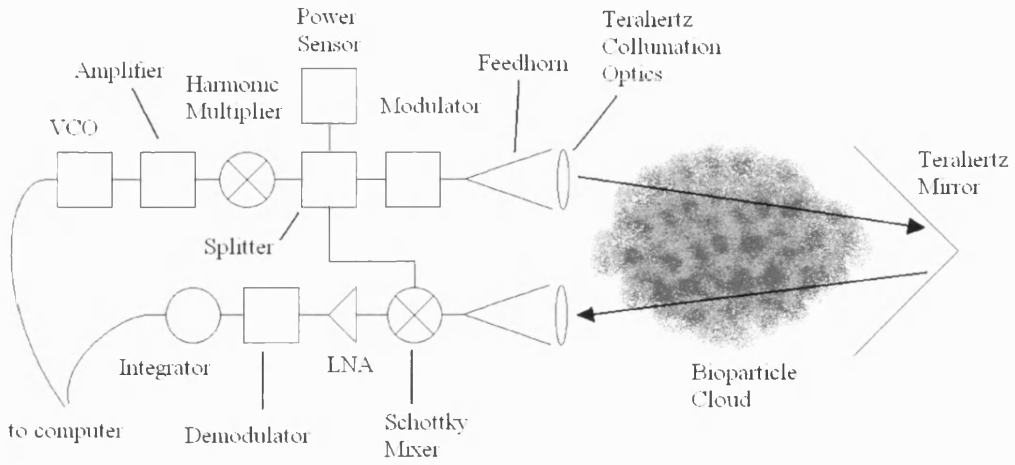

Fig. 1.1 Schematic diagram of potential bioparticle cloud detector [1.8].

1.1.4 Communication Systems

The demand is growing rapidly worldwide for wideband telecommunications. The main driver for this technology is the replacement of HDMI or DVI cables with a high data rate wireless connection. This broadband connection will allow broadcast of HD television as well as multimedia content to different terminals around the house; Fig. 1.2 gives a pictorial suggestion of how such a system may be used. Both Philips and IBM have recently presented at the IWPC conference their road maps for a 5 Gbit/s architecture plan to be deployed by 2010. The presented system will work at 60 GHz and will require a beam steering design to provide multipoint access as well as high data rates. The high absorption effect of the atmosphere and narrow beam widths make these wavelengths well suited to intra-building, secure, high speed, wireless communication links. Millimetre-wave gallium arsenide (GaAs) or Silicon Germanium (SiGe) Monolithic Microwave Integrated Circuits (MMIC's) are a key component of the broadband and high data rate wireless local-area networks that are being investigated.

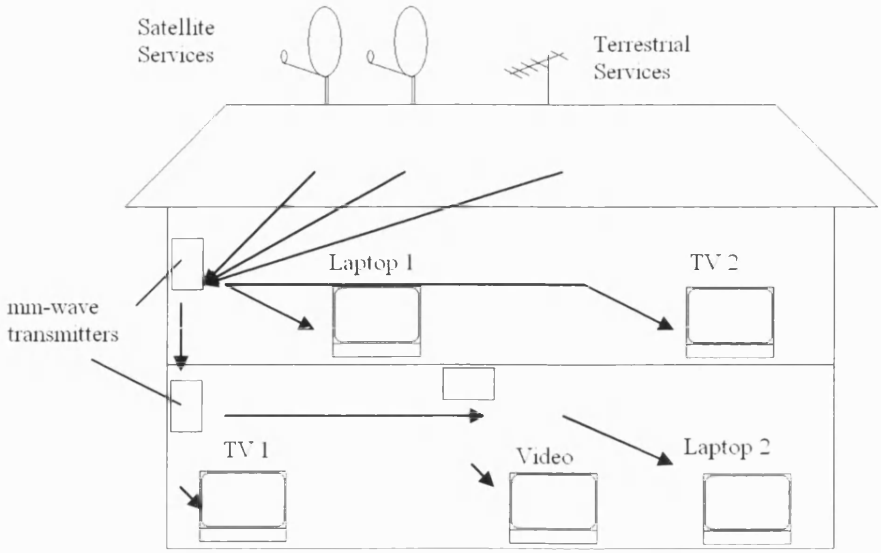

Fig. 1.2 Millimeter wave video transmission system.

1.1.5 Plasma Diagnostics

Many properties can be deduced by looking at the absorption, scattering and phase shift of mm-wave radiation through a plasma, [1.9, 1.10]. The plasma electron density (P_e) and temperature can be found through absorption of a certain frequency (f_p) given by

$$f_p = 8.974\sqrt{P_e}\ . \tag{1.1}$$

An electron density of 10^5 cm^{-3} pushes f_p into the sub-mm range and hence diagnostic tools need to cover this range [1.11].

1.1.6 Explosives and Weapon Detection

Following the 9/11/2001 terrorist attack and recent events around the world, a large effort has been made to increase the security in public places such as airports or subways. The US Homeland Security is funding different projects for THz imaging. At mm-wavelengths most clothing material has a very low absorption factor and hence appears 'see-through'. Weapons such as plastic or ceramic knives and explosives can be revealed at frequencies of 100 GHz and above. Increasing the frequency enables the system to detect smaller object, however a trade-off exists due to the signal to noise ratio reduction at high frequency. All materials have different reflectivity and emissivity; concealed items can be detected even if they are at the same physical temperature as the underlying skin. There are essentially two modes of

terahertz imager. Passive imagers using natural blackbody radiation of the subject, combined with reflections from the thermal background. The second method is active imaging; in this method the subject is illuminated with a source of terahertz energy and the reflected signal is detected.

A UK team [1.12, 1.13] have recently completed trials of a real time mm-wave imager at 33 GHz. Constructed at QinetiQ, Malvern, UK, the trials in both laboratory and a real airport and subway environment resulted in the successful detection of ceramic and plastic weapons although plastic explosives were more difficult to locate.

1.1.7 Other Commercial Applications

Commercial applications at millimetre-wave frequencies are largely driven by the availability of low-cost MMICs. SiGe and CMOS processes have been shown to reach 60 GHz for receiver applications. Automotive radars are being installed on Mercedes and Volkswagen vehicles. These first radars only provide active cruise control. Future systems need to detect smaller targets such as pedestrians and provide information on the different lanes on an highway. Such systems will require multiple mixer devices, patch antennas and beam-steering antennas to do the detection. THz imaging, automotive radar and high data rate systems will potentially be available in the next 5 to 10 years and will provide the first commercial applications at millimetre-wave.

1.2 Elements of the Heterodyne Receiver

A block diagram of a heterodyne receiver is shown in Fig. 1.3. This typical configuration is found in many systems such the one described in the previous section, e.g. a radio telescope. First the signal is collected by an antenna and redirected to the diplexer. The diplexer spatially combines the signal (RF) and the local oscillator (LO). The mixer electrically mixes the RF and LO, generating a nearly exact copy of the RF spectrum at the intermediate frequency (IF), where the IF frequency is the difference between the RF signal and the LO $f_{IF} = |f_{RF}-f_{LO}|$. The IF is then amplified so further processing is possible. The RF signals need to be down-converted to an IF frequency due to limitation of electronics to process or to directly study the signal at high frequency. Any signal above 100 GHz needs to be

down-converted before being analysed. The best sensitivity for these receivers is achieved by careful choice in the mixer technology. The following section gives a detailed description of the different technologies use for the receiver block.

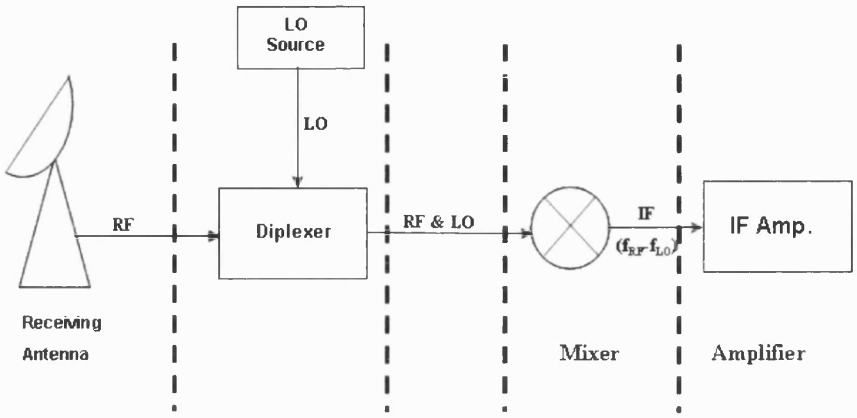

Fig. 1.1 Schematic layout of a submillimeter receiver.

1.2.2 Antenna

An important component in any receiver system or communication system is the antenna. An antenna will convert a wave propagating in free-space to a wave propagating on a transmission line, or vice versa. A large variety of antennas exist but in many cases the antenna has to be tuned and designed for a specific application and system. Some of the most common types are summarised here.

Wire antennas were the first type of antenna used by Hertz and Marconi. They are still used, but at low frequencies (HF and UHF). These are easy to fabricate, easy to feed and are lightweight.

Patch or printed antennas are a relatively new type of antenna. They consist of a printed conductor on a microstrip. In this research this type of antenna is used to transfer the power from the RF and LO waveguide to the stripline and to the diode. Printed antennas usually have low gain and are not broadband.

Reflector antennas consist of a parabolic (or dish) antenna. The dish collects incoming radiation onto a small antenna referred to as the feed, which typically is an aperture antenna. These antennas generally have very high gain but are large and unwieldy. This antenna can cover the all radio frequency spectrum. At submillimetre frequencies, the antenna dish must be built with very high accuracy, requiring

surface roughness of less 15 μm on a 10 meter in diameter dish, e.g. Heinrich Hertz telescope.

Aperture antennas are flared sections of waveguide or open-ended waveguide. These antennas are commonly used at millimetre wave frequencies. In this research a 200 GHz Pickett potter feed horn antenna was used during measurement of the mixer.

1.2.3 LO Power Source

Microwave sources are an essential part of any receiver system. However, in the region of 100 GHz to 10 THz useable solid state sources do not exist and only microwave tube sources can deliver high power. Solid-state sources are low power and low frequency but are small in size, low cost and compatible with MMIC. Microwave tubes can deliver high power and high frequencies but are often bulky and waveguide based.

The following section presents the most common type of RF sources.

1.2.3.1 Gunn Diodes

Gunn diodes are the most common source of millimetre-wave power, and are used as the local oscillator in receiver applications. Gunn diodes directly convert a DC bias to RF power in the frequency range of about 2 to 100 GHz. Low power at frequencies above 100 GHz up to terahertz frequencies can be reached using Gunn diode oscillators combined with frequency multipliers. Output powers in the region of 32 mW have been demonstrated at about 200 GHz [1.14]. Fundamental to the operation of a Gunn diode oscillator is the Negative Differential Region (NDR) in its IV characteristic. Tuning of the external circuit can change the resonant frequency of these transit-time devices and various modes of operation are possible. DC to RF conversion efficiencies in the region of 1.2 % have been reported for devices with operating frequencies exceeding 100 GHz [1.15, 1.16].

1.2.3.2 Transistor Oscillators

Transistor oscillator designs generally work at low frequencies and have lower output power compared to Gunn oscillators. Transistor oscillators have the advantage over Gunn diode of being readily compatible with MMIC circuits, allowing integration with FET amplifiers and mixers on a monolithic circuit. Frequency, phase

locking and modulation are also more easily achieved with transistor oscillator circuits.

GaN high electron mobility transistors (HEMT) have been used as solid state sources and are showing great potential to deliver high power up to W-band. InP HEMT have been also demonstrated to produce powers around 60 mW at 94 GHz with high efficiency, [1.17] and a large programme funded by the US Department of Defense aims to deliver 150 W of power over a 2 to 20 GHz band. The high power is achieved by combining powers at the device level or circuit level.

Other devices such as heterojunction bipolar transistors (HBT's) and field effect transistors (FET's) have also been used to generate signals of the order of one to two hundred gigahertz.

1.2.3.3 Microwave Tubes

Microwave tubes involve the interaction of an electron beam with an electromagnetic field inside a metal vacuum envelope. A hot cathode is used to generate the stream of electrons by thermionic emission. The electrons are extracted and focused to the region where the desired interactions with the RF field take place. A collector located at the opposite side of the cathode provides the current path back to the power supply. Two categories of microwave tube exist. Linear-beam configuration: the electron beam traverses a length of tube and is parallel to the electric field, e.g. Klystron. Crossed-field: the field is perpendicular to the accelerating electric field, e.g. Gyratron.

These microwave tube sources can deliver high power (10-100 kW), up to high frequencies but due to the need of ultra high vacuum, heavy biasing and high voltage power supplies microwave tube are generally very large and bulky.

1.2.4 Mixer

At the heart of any receiver or transceiver system lies the mixer circuit. The heterodyne mixer makes use of a nonlinear device, which is commonly a diode. The heterodyne mixer circuit enables the conversion of a high frequency signal to lower frequency where electronic devices are available to analyse and study the RF signal. The down-conversion to lower frequency using a nonlinear mixer requires a local

oscillator source at a frequency close to the RF signal. The RF and LO signals coupled to the mixer generate the sum and the difference of those frequencies. Due to its nonlinear response, the mixer will give rise to different mixing products, with a special product being the difference between the RF signal and the LO: the intermediate frequency (IF). After filtering the unwanted products from the mixer, the IF signal is amplified before being analysed. IF frequencies of a few GHz are commonly used, where low noise amplifiers are available. Chapter 3 presents the different types of nonlinear devices composing the mixer and the different circuit architectures available for high frequency down-conversion.

1.3 Project originality and thesis overview

1.3.2 Project Originality

Over the past three decades the mixing element of choice for most millimetre- and submillimetre wavelength receivers has been the GaAs Schottky barrier diode. During the first fifteen years the configuration of choice for the mixing element was the whisker-contacted diode. The whisker diode configuration and geometry has the advantage of providing extremely low parasitic capacitance to the diode, which is the major reason for its excellent performance at SMW. However, as presented in Chapter 3 the contact is fragile and thus not reliable when stressed or shocked. The assembly is also cumbersome. The integration of single or multiple diodes with the surrounding circuit is also very difficult. In the mid 1980s different research laboratories around the world developed planar Schottky diodes. The planar Schottky diode uses standard wafer processing, which is suitable for integration of the diode with surrounding circuits or multiple diodes. The diode geometry provides rugged, reproducible and reliable Schottky contacts. Planar Schottky diodes capable of down-converting signals up to THz frequencies need to exhibit very low parasitic capacitance and very low series resistance. Today only a few places in the world produce such diodes and they are extremely expensive for submillimetre-wave applications. Discrete planar Schottky diodes are traditionally flip-chip mounted on the RF circuit. This packaging has considerable parasitics that make their performance uncompetitive compared with whisker-contacted diodes.

The overall focus of this research was to develop a mixer that has low cost, good sensitivity, high reliability and repeatability and quick and easy fabrication and assembly.

The first part of this research was to develop a reliable process to fabricate submillimetre Schottky diodes with very low parasitic capacitance, low ideality factor and low series resistance.

The second part concerned integration of the planar Schottky diode with the RF circuit to greatly reduce the parasitics introduced during the flip-chip mounting, thus improving the performance of the heterodyne mixer. The mixer's substrate thickness was reduced down to a few tens of microns to reduce the high dielectric loss at high frequencies.

1.3.3 Thesis overview

In the following chapters, the design, modelling, fabrication and measurements of GaAs planar Schottky diodes as well as two different integrated mixers are presented. This introductory chapter has highlighted existing and potential terahertz applications and introduced the circuit topologies of typical sub-millimetre frequency receivers.

Chapter 2 contains fundamental theory relating to the Schottky devices conventionally used within sub-millimetre wave mixer circuits and the theory of fundamental and subharmonic mixers.

Chapter 3 reviews different nonlinear devices as well as different mixer configurations developed by various research groups.

Chapter 4 presents the design and modelling of planar Schottky diodes to produce high frequency mixers. The second part presents the modelling of the first generation of integrated Schottky diodes. The final section presents the modelling of a 183 GHz integrated fixed tuned mixer developed in collaboration with RAL, LERMA Observatory of Paris and LISIF University of Paris 6.

Chapters 5 and 6 review the processing schemes developed during this research to fabricate planar Schottky diodes. The second and final parts present the fabrication scheme respectively for the first integrated device and 183 GHz fixed tuned mixer.

Chapter 7 contains results of the planar Schottky diode tested at DC. The RF mixing results using the diode fabricated during this research are compared with modified commercial diodes from United Monolithic Semiconductor (UMS). The final section reviews the DC and RF mixer tests carried out on the first generation integrated mixer and 183 GHz fixed tuned mixer.

Suggested improvements and concluding remarks for future work form the basis of Chapter 8.

References

[1.1] S. R. Davies, *et al.*, , "A 210–280 GHz SIS heterodyne receiver for the James Clerk Maxwell Telescope. Part I: Design and performance." *International Journal of Infrared and Millimeter Waves*, **13**, pp. 647-658, 1992.

[1.2] ALMA home page: http://www.mma.nrao.edu/

[1.3] N. Mandolesi and F. Villa, "FIRST/Planck mission", *IMTC/99 Proceedings of the 16th IEEE Instrumentation and Measurement Technology Conference*, vol. 2, part 2, pp. 975-980, 1999.

[1.4] C. A. Reber, "The Upper Atmosphere Research Satellite (UARS)", *Geophysical Research Letters*, vol. 20, no. 12, pp. 1215-1218, June 1993.

[1.5] T. Wehr, S. Crewell, K. Kunzi, J. Langen, H. Nett, J. Urban and P. Hartogh, "Remote sensing of ClO and HCl over northern Scandinavia in winter 1992 with an airborne submillimeter radiometer", Journal of Geophysical Research, vol.100, no. D10, pp. 20957-20968, Oct. 1995.

[1.6] G. Dobson, *et al.*, "Measurements of the amount of ozone in earths atmosphere and its relation to other geophysical conditions," *Proc. Roy. Soc. London*, vol. A122, 1929, pp. 456-486.

[1.7] J. W. Waters, "Submillimeter-wavelength heterodyne spectroscopy and remote sensing of the upper atmosphere," *Proc. of the IEEE*, vol.80, no.11, pp. 1679-1701, November 1992.

[1.8] D. Woolard, R. Kaul, R. Suenram, A. H. Walker, T. Globus and A. Samuels, "Terahertz electronics for chemical and biological warfare agent detection", IEEE MTT-S International Microwave Symposium Digest, 1999, pp. 925-928.

[1.9] A. Mardon, "Applications of millimeter waves," M*illimeter and Submillimeter Waves*, Ed. F. A. Benson, Illife Books Ltd., pp. 525-527, 1969.

[1.10] S. Xuemin, "Electron cyclotron absorption measurements in a tokamak plasma using the five channel E-band millimetre-wave system," *Proc. Int. Conf. on Microwave and Millimeter-Wave Technology ICMMT*, 18-20, August 1998, pp. 623-625.

[1.11] P. Woskoboinikow, "Development of gyrotrons for plasma diagnostics," *Review of Scientific Instruments*, vol. 57, no. 8, pt. 2, pp. 2113-2118, August 1986.

[1.12] O. Minin, "Quasioptical mm-wave concealed weapon detection systems: review," *Proc. Int. Symp. the 7th Korea-Russian Science and Technology KORUS*, vol. 3, June 28 – July 6, 2003, pp. 60-64.

[1.13] K. J. Murphey, *et al.*, "Millimeter-wave aviation security scanner," *Proc. Int. Conf. 36th Annual Security Technology*, 20-24 October, 2002, pp. 162-166.

[1.14] A. Rydberg, "High efficiency and output power from second- and third-harmonic millimeter-wave InP-TED oscillators at frequencies above 170 GHz", IEEE Electron Device Letters, vol. 11, no. 10, pp. 439-41, Oct. 1990.

[1.15] H. Eisele, A. Rydberg and G. I. Haddad, "Recent advances in the performance of InP Gunn devices and GaAs TUNNETT diodes for the 100-300-GHz frequency range and above", IEEE Transactions on Microwave Theory & Techniques, vol. 48, no. 4, pt. 2, pp. 626-631, April 2000.

[1.16] H. Eisele and G. I. Haddad, "Efficient power combining with D-band (110-170 GHz) InP Gunn devices in fundamental-mode operation", IEEE Microwave & Guided Wave Letters, vol. 8, no. 1, pp. 24-26, Jan. 1998.

[1.17] P. M. Smith *et al.*, "W-band high efficiency InP-based power HEMT with 600 GHz f_{max}," *IEEE Microwave and Guided Wave Letters*, vol. 5, no. 7, pp. 230-232, July 1995.

Chapter 2

Diode and Mixer Theory

A complete analysis of mixer performance requires good knowledge of all the diode parameters and the embedding impedances presented to the diode at all LO harmonics and mixing frequencies. For the mixer to work efficiently its active device, the Schottky diode, must perform within certain parameters. A general rule, however, is that the device should have a low series resistance, a low *ideality factor* and low resistance ohmic contacts. Methods are discussed in later chapters on how to improve device performance in a mixer such as optimising the diode anode geometry, the doping concentration of semiconductor layers and the thickness of those layers. Understanding the behaviour of the diode capacitance and the diode series resistance at all LO harmonics and mixing frequencies was key in optimising the diode design and assessing mixer performance.

2.1 Diode Theory

Before considering the diode theory described by Schottky and Mott it is important to look at the early work done on the point-contact diode. In October 1906 Greenleaf Whittier Pickard received a patent on a method for receiving radio signals that included a silicon point-contact diode. These detectors were far superior to the coherer invented by Edouard Branly in 1880 and used by Marconi in 1901 to established the first transatlantic radio link [2.1]. Although it was not known how the point-contact diode worked, the device was still manufactured. It was not until 1938 that Schottky [2.2] created a theory to describe the rectifying behaviour of a metal-semiconductor contact resulting from the depletion region and potential barrier that is formed between them. Early work done by Mott [2.3] described the metal semiconductor interface in terms of energy band diagrams and included the effect of impurity atoms in a semiconductor. Metal semiconductor interface behaviour is also described in [2.4], [2.5].

The energy band structure of a metal and an *n* type semiconductor are shown in Fig. 2.1. The electrons in the semiconductor have more energy than those in the metal. When the two materials are brought into intimate contact, charges flow from the

semiconductor to the metal. The vacuum level (E_0) must be continuous, causing the conduction and the valence band to "bend". The unequal work functions in the metal and semiconductor give rise to an electrostatic barrier at their interface, and at thermal equilibrium Fermi levels on both sides line-up leading to the formation of a Schottky barrier $q\Phi_b$.

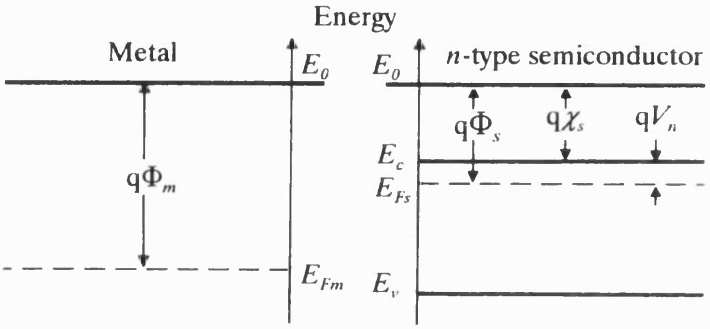

Fig. 2.1 Shows the band structure of a metal and semiconductor before intimate contact. Φ_m and Φ_s are the work functions of the metal and semiconductor respectively, E_{Fm} and E_{Fs} are the Fermi levels in the metal and semiconductor respectively, E_v and E_c are the energy levels of the valence and conduction bands respectively, χ_s is the electron affinity of the semiconductor, V_n is the difference between the semiconductor Fermi level and the conduction band and E_0 is the zero or vacuum level [2.6].

Fig. 2.2 shows the ideal case for a n-GaAs diode (a) with no bias applied, (b) when a forward bias voltage is applied and (c) when a reverse bias voltage is applied across the junction. The field formed by the positive ions left behind in the semiconductor and electrons at the surface of the metal is directly proportional to the number of electrons that passed from the semiconductor to the metal and this is generally determined by the specific materials used.

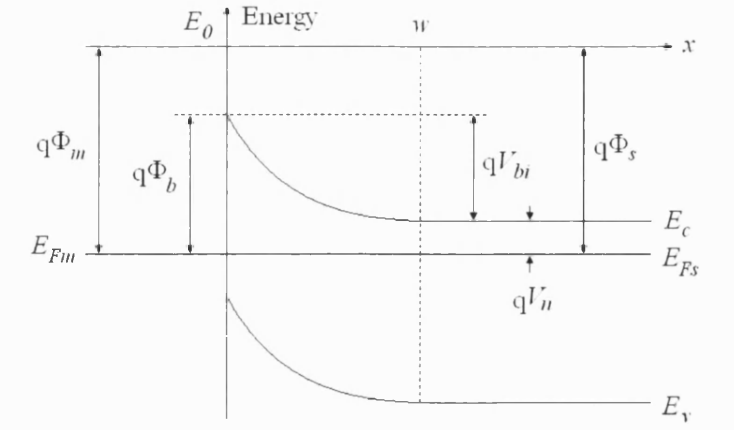

(a)

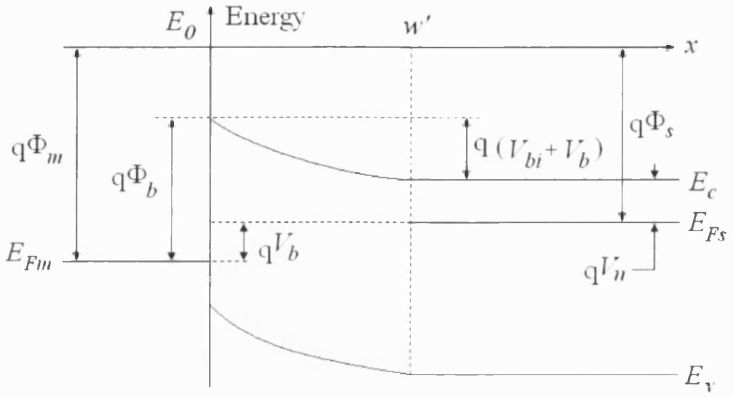

(b)

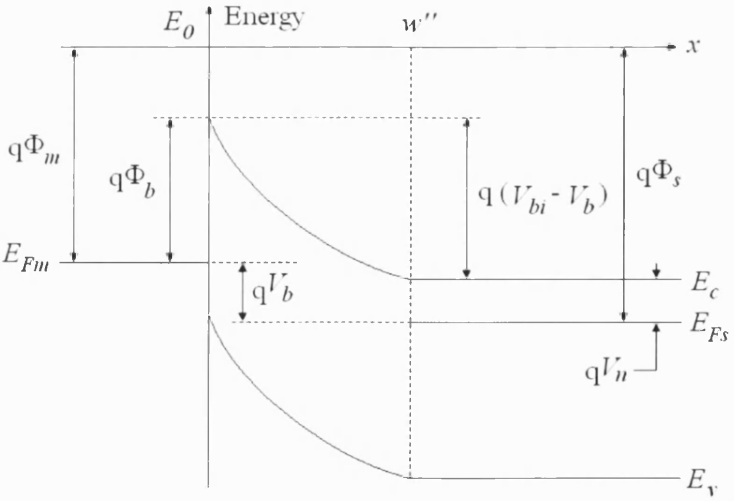

(c)

Fig. 2.2 Energy band diagram of metal and *n* type semiconductor in (a) thermal equilibrium (b) with an applied forward bias voltage V_b and (c) with a reverse bias voltage V_b. Φ_b is the potential of the barrier and V_b is the external bias applied to the junction, V_{bi} is the built-in voltage and w, w' and w'' are the depletion region widths at equilibrium, with forward bias and with reverse bias [2.6].

The barrier height is different for various metals but is always determined by [2.7]

$$\Phi_b = V_{bi} - V_n \tag{2.1}$$

where V_n is given by

$$V_n = \frac{kT}{q} \ln \frac{N_c}{N_D} \tag{2.2}$$

where k is the Boltzmann constant, T is the temperature, q is the charge on an electron, N_c is the density of states in the conduction band of the semiconductor (equal to 4.7 x 10^{17} cm^{-3} in GaAs at 300 K) and N_D is the doping density of the GaAs epilayer.

An example of barrier height for different metals on silicon and gallium arsenide is given in Fig. 2.3.

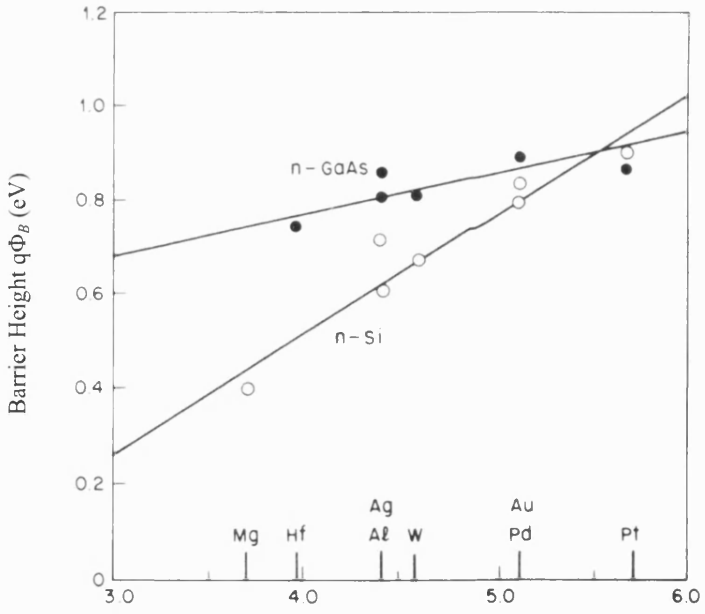

Fig. 2.3 Barrier height for metal-silicon and metal-gallium arsenide contacts, [2.7].

The depletion approximation assumes that no conduction electrons exist in the region denoted by bent energy bands ($0 < x < w$ in Fig. 4.2) and the resulting charge is due entirely to positive donor ions. The depletion region width, w, is given by [2.6]

$$w = \left[\frac{2\varepsilon_s}{qN_D} (V_{bi} - V_b) \right]^{1/2} \tag{2.3}$$

where ε_s is the total permittivity of the semiconductor, V_{bi} is the built-in potential and V_b is the applied bias voltage.

The diode junction capacitance C_j of an anode of area A_0 is therefore given by

$$C_j = A_0 \sqrt{\frac{q \varepsilon_s N_D}{2 (V_{bi} - V_b)}} \tag{2.4}$$

which can be used to determine N_D , V_{bi} and hence Φ_b from a plot of $1/C_j^2$ versus V_b.

A more detailed analysis of the depletion region shape is given in [2.8] where anode edge effects at high frequencies are found to play an important role in the voltage modulation. The space charge per unit area from the ionised donors in the depletion region is given by

$$Q_{sc} = qN_D w. \tag{2.5}$$

By calculating the net charge of the depletion region the capacitance of the Schottky contact can be found [2.9]

$$C_j = \frac{\varepsilon_s A_0}{w} \left(1 + b \frac{w}{R_0} \right) \tag{2.6a}$$

where R_0 is the radius of the diode anode. The second term in the parentheses is a first order correction factor for frequencies corresponding to millimetre wavelengths and b is a numerical constant equal to 1.5. At submillimetre wavelengths a second correction factor is added given by [2.10]

$$C_j = \frac{\varepsilon A_0}{w}\left(1 + b_1 \frac{w}{R_0} + b_2 \frac{w^2}{R_0^2}\right) = \frac{\varepsilon A_0}{w}\gamma_c \qquad (2.6b)$$

where $b_1 = 1.5$ and $b_2 = 0.3$. The correction factor, γ_c, can vary typically from 1.0 ($w = 0$) to 1.5 ($w = t_e = R_0/3$) during an LO pump cycle.

The previous equations assume ideal surface state, and therefore no chemical reactions or physical strains created between the metal and the semiconductor or impurities or oxide film is present at the surface. In practice the Schottky barrier is found not to be dependent on the work function of the metal but pinned by the surface states of the semiconductor. Typical values of ϕ_{bn} are all close to 0.8 eV independently of the metal used.

2.2 Diode Current Considerations

The current transport mechanism for low-doped GaAs or at low bias is mainly dominated by emission of electrons over the barrier, called thermionic emission. For higher doping concentration, or at higher bias, the depletion region is reduced and the major current transport occurs by tunnelling through the barrier called tunnelling field emission.

2.2.1 Barrier Current Transport Mechanisms

2.2.1.1 Thermionic Emission

Two main theories exist over the process which sets the limit of current through emission over the barrier. *Diffusion theory* suggests the current is limited to drift and diffusion of carriers in the depletion region. *Thermionic-emission theory* suggests that the current is set by the rate of transfer of carriers from the semiconductor to the metal and that diffusion is negligible. Fig. 4.4 demonstrates the basic current mechanisms.

A synthesis of the two theories was formed by Crowell and Sze [2.7] suggesting a continuum of the two mechanisms. This meant that the current from drift and diffusion should equal that of the thermionic emission and as a result, at low bias conditions, the current across the junction should be

$$J_b = \left[A^{**} T^2 \exp\left(-\frac{q\Phi_b}{kT} \right) \right] \left[\exp\left(\frac{qV_b}{kT} \right) - 1 \right] \tag{2.7a}$$

$$J_b = J_s \left[\exp\left(\frac{qV_b}{kT} \right) - 1 \right] \tag{2.7b}$$

where A^{**} is the modified Richardson constant which, at moderate doping levels (10^{16} to 10^{17} cm^{-3}) and low bias, will be a constant value.

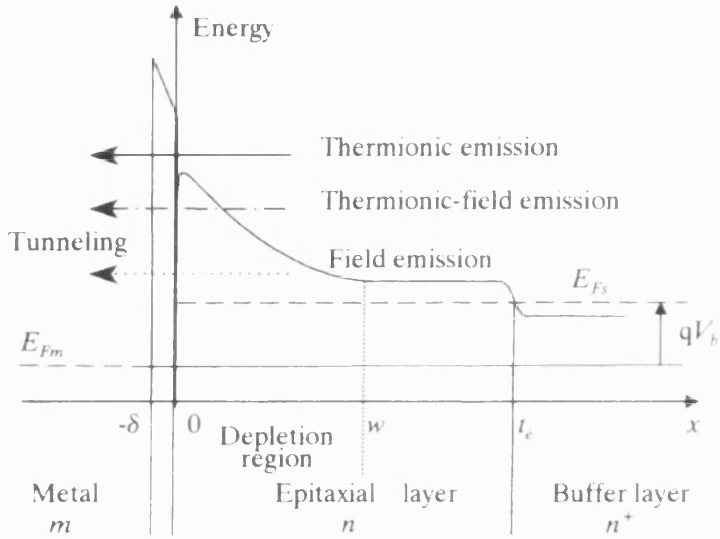

Fig. 2.4 Energy band diagram of a forward biased Schottky contact showing the main contributors to conduction across the barrier where t_e is the total epilayer thickness. The energy level spike between $-\delta < x < 0$ can arise from a non-perfect interface between the metal and the *n* layer of the semiconductor, e.g. presence of an oxide layer, [2.6].

The Richardson constant is a measure of the thermionic emission of carriers across the Schottky barrier. The modified Richardson constant accounts for quantum mechanical reflection and phonon scattering given by [2.11]. For GaAs the value is around 8.4 A cm^{-2} K^{-2} although this value will change with higher bias and or temperature, [2.6, 2.12].

2.2.1.2 Barrier Tunnelling

There are two main components to the tunnelling of carriers through the barrier [2.11, 2.13]. These occur at high doping densities and low temperature. *Field emission* occurs when the barrier is so thin, due to high doping and low temperature, that

carriers may quantum-mechanically tunnel through the barrier. Alternatively, if the temperature is increased then the energy of the carrier is such that they see a very thin and much lower barrier and the probability of tunnelling is greatly increased. This is *thermionic-field emission* and is regulated by the fact that at higher temperatures only a small amount of carriers may hold this higher energy. This results in a temperature dependent balance between the two mechanisms. Obviously if the temperature is above a certain threshold then all carriers will have enough energy to scale the barrier and the process becomes purely thermionic emission. Forward current density due to tunnelling is given by [2.14]

$$J_b = J_s \exp\left(\frac{V_b}{E_0}\right) \tag{2.8a}$$

where

$$E_0 = E_{00} \coth\left(\frac{qE_{00}}{kT}\right) \tag{2.8b}$$

and

$$E_{00} = \frac{h}{4\pi}\left(\frac{N_{De}}{m^* \varepsilon_s}\right)^{1/2}. \tag{2.8c}$$

J_b is the current density across the barrier, h is the Planck constant, $m^* = m_r m_o$ is the effective mass of the electrons in the n type semiconductor material and ε_s is the permittivity of the n type semiconductor material. J_s is the tunnelling saturation current which is a function of the temperature, barrier height and other semiconductor properties.

The Schottky diodes fabricated during this project used low doped GaAs n-type epilayers (N_D = 4.0 x 10^{17} cm^{-3}), and operated at room temperature or below. With these conditions the tunnelling current can be neglected for a device working at room temperature with a doping concentration under $10^{17}cm^{-3}$. However, the *ideality factor* was introduced to help describe the junction behaviour at various temperatures and doping levels and is given by [2.15]

$$\eta = \frac{q}{kT}\frac{\partial V_b}{\partial(\ln J_b)} \tag{2.9}$$

where an ideality of one indicates pure thermionic emission and any increase above one is a deviation from the ideal model. Therefore the I/ V characteristic can be defined as

$$I_b = I_s\left[\exp\left(\frac{qV_b}{\eta kT}\right)-1\right] \tag{2.10}$$

where I_s is the saturation current given by

$$I_s = A_0 A^{**} T^2 \exp\left(-\frac{q\Phi_b}{kT}\right). \tag{2.11}$$

2.2.2 Ohmic Contacts

Ohmic contacts have been widely studied from as far back as the first work of Schottky in 1938. The physics involved is well understood but the fabrication process is still under investigation to get lower contact resistance and more reliable contacts [2.16, 2.17].

In order to have an ohmic contact, the semiconductor must be highly doped (1.0x 10^{18} cm^{-3}); it is the n^+ layer of the semiconductor. In such circumstances, the tunnelling current will dominate.

The contact resistance R_c is given by the figure of merit:

$$R_c \equiv \left(\frac{\partial J}{\partial V}\right) \tag{2.13}$$

Because the current is mainly tunnelling, then R_c becomes:

$$R_c = \exp\left[\frac{4\pi\sqrt{m^*}\varepsilon_s}{h}\left(\frac{\Phi_b}{\sqrt{N_{De}}}\right)\right]. \tag{2.14}$$

2.2.2.1 Fabrication of Ohmic contacts

Any metal in contact with a highly doped GaAs surface will produce an ohmic contact. The doping concentration of the GaAs, as seen above, needs to be high. A high level of doping is not easily achievable by growth or doping techniques and is not a cost effective option. The most common approach to fabricate ohmic contacts

on moderately doped GaAs (10^{16} to $4x10^{18}$ cm^{-3}) is to alloy an appropriate metal to dope the surface layer. The metals used to dope *n* GaAs are Si, Ge, Sn and Te. Zn, Cd, Be and Mg are used to dope *p* GaAs.

The most common metal combination used to make ohmic contacts on moderately doped *n* GaAs is Ge-Au. The gold and germanium are applied in a proportion that represents the eutectic alloy (88 % Au, 22 % Ge by weight), this eutectic melts at 360 °C. During the alloying and cooling period, the germanium will diffuse to free gallium sites, and acts as a dopant, while the gallium will have migrated into the gold. The amount of gold and germanium need to be accurately deposited because too much gold could get more gallium than there is germanium available to replace it. If this occurs, the resulting gallium vacancies can cause a high resistance region. Also experimental results show that the reliability of ohmic contact systems with a Ti diffusion barrier layer are greatly superior to that of traditional AuGe/Au [2.18]. For this reason, a diffusion barrier of Ti or W is often used and is placed between the Au-Ge eutectic and the gold overcoat. Such a gold overcoat has several advantages. Alloyed Au-Ge metallisation has poor sheet resistance and is difficult to probe and wire-bond. Also, the resistance of the probe to metal contact is overly sensitive to probe pressure and an overlaying layer of gold greatly alleviates these problems.

Ni or In can be used to enhance the fabrication of ohmic contacts or decrease the contact resistance [2.16]. The Ni is used to act as a wetting agent and aids in the diffusion of Ge in to the GaAs. The nickel is commonly used in a ratio of 28 nm for every 100 nm of AuGe [2.17].

2.3 Mixer Theory

A mixer is essentially a multiplier and any non-linear device can be used as a multiplier, and hence as a mixer. Fig. 2.5 shows a heterodyne receiver system block diagram, the output of which has components at the sum and difference frequencies of the input signals.

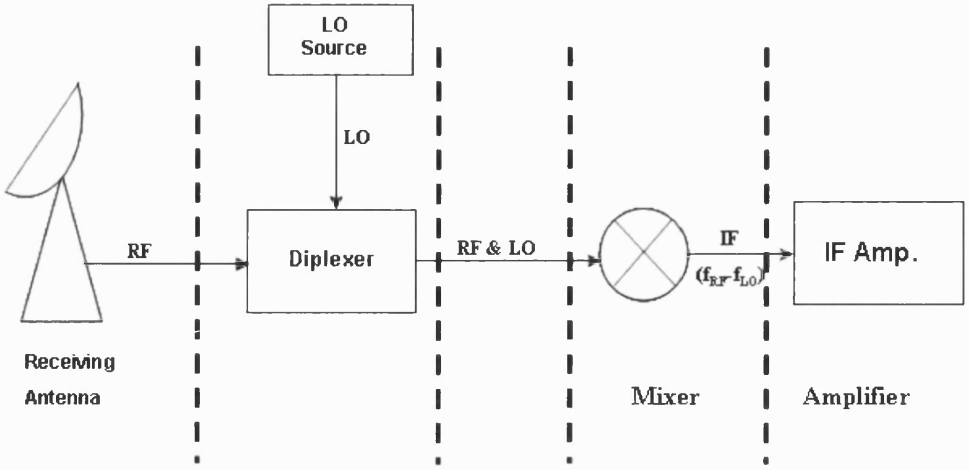

Fig. 2.5 Heterodyne receiver block diagram.

The input signals consist of a radio frequency signal (RF) received from an antenna and a reference signal from a local oscillator (LO). A diplexer spatially combines the two signals. The output contains the sum and the difference frequencies of the input signals. The difference or intermediate frequency can be extracted through a low-pass filter and then amplified by a low noise amplifier. This configuration has much better sensitivity and noise characteristics than direct detection. At a low IF, it is possible to fabricate highly selective filter circuits for the IF system. The heterodyne system can also be tuned over a wide RF band by simply changing the LO frequency. The fundamental mixer is the most commonly used configuration at millimetre-wavelengths to provide the lowest possible conversion loss and the maximum possible sensitivity. The sub-harmonic mixer is the configuration adopted for this project; the advantages of such a configuration over a fundamental mixer are discussed later in this chapter.

2.3.1 Fundamental mixer

Although the mixer configuration used in this research was based on an anti-parallel diode pair design, single diode mixers are often used in millimetre-wave receiver applications and are fundamental to model all mixers, especially the sub-harmonic mixers.

The Schottky barrier diode was examined in section 2.1. The equivalent circuit of the diode, including non-linear junction capacitance and resistance, plus linear series resistance, is shown in Fig. 2.6.

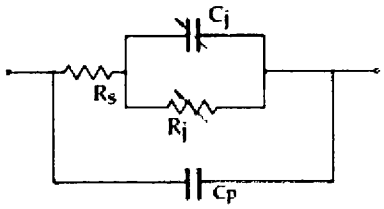

Fig. 2.6 Equivalent circuit model of Schottky diode [2.22].

This circuit represents the intrinsic diode junction, where *Cj* and *Rj* are respectively the voltage-dependent capacitance and resistance components of the Schottky diode. The other elements will be discussed in Chapter 3 and represent the series resistance R_s and the parasitic capacitance C_p.

The junction *I/V* characteristic is given by:

$$I_b = I_s\left[\exp\left(\frac{qV_b}{\eta kT}\right)-1\right] \tag{2.10}$$

For a conventional single diode mixer, consider the application of a voltage waveform *V* such as:

$$V = V_0 + v \tag{2.11}$$

where V_0 is a DC bias voltage and v is a small AC signal voltage.

For V_b=*V* equation 2.10 can be expanded in a Taylor series about V_0 as follows:

$$I(V) = I_0 + v\frac{dI}{dV} + \frac{1}{2}v^2\frac{d^2I}{dV^2} + ... \tag{2.12}$$

where I_0=$I(V_0)$ is the DC bias current.

The first derivative can be evaluated as

$$\frac{dI}{dV} = \alpha I_s e^{\alpha V_0} = \alpha(I_0 + I_s) = G_d = \frac{1}{R_j} \tag{2.13}$$

where $\alpha=q/\eta kT$ and Rj and G_d represent the junction resistance and the dynamic conductance of the diode respectively.

The second derivative is

$$\frac{d^2I}{dV^2} = \alpha^2 I_s e^{\alpha V_0} = \alpha^2(I_0 + I_s) = \alpha G_d = G'_d \tag{2.14}$$

Equation 2.12 becomes

$$I(V) = I_0 + vG_d + \frac{1}{2}v^2 G'_d + ... \tag{2.15}$$

Consider the use of equation 2.15 for the single ended mixer circuit with an applied voltage $v = v_{LO}\cos(\omega_{LO}t) + v_S\cos(\omega_S t)$. The diode current will consist of constant DC current I_0 and RF and LO signals of frequencies ω_{LO} and ω_S, due to the term which is linear in v. The v^2 term will give rise to the following output current I_2:

$$\begin{aligned} I_2 &= \frac{G'_d}{2}\left(v_S\cos(\omega_S t) + v_{LO}\cos(\omega_{LO}t)\right)^2 \\ &= \frac{G'_d}{2}\left({v_S}^2\cos^2\omega_S t + 2v_S v_{LO}\cos\omega_S t\cos\omega_{LO}t + {v_{LO}}^2\cos^2\omega_{LO}t\right) \\ &= \frac{G'_d}{2}\left[{v_S}^2 + {v_{LO}}^2 + {v_S}^2\cos 2\omega_S t + {v_{LO}}^2\cos 2\omega_{LO}t\right. \\ &\left. + 2v_S v_{LO}\cos(\omega_S - \omega_{LO})t + 2v_S v_{LO}\cos(\omega_S + \omega_{LO})t\right] \end{aligned} \tag{2.16}$$

Equation 2.16 shows that the current through the diode contains frequencies that correspond to the sum and the difference between the frequency of the signal (w_S) and the frequency of the local oscillator (ω_S). The most important of these for a mixer is the Intermediate Frequency (IF) which arises from $\omega_{IF} = \omega_S - \omega_{LO}$ or $\omega_{IF} = \omega_{LO} - \omega_S$, respectively the upper sideband (USB) and lower sideband (LSB).

The other terms $2\omega_S$ and $2\omega_{LO}$ are at much higher frequencies and can be filtered out with a low-pass filter. For a given LO frequency, there will be two RF frequencies that will mix down to the same IF frequency.

If the RF frequency is $\omega_S = \omega_{LO} + \omega_{IF}$, the output frequencies of the mixer will be

$$w_S \pm w_{LO} = \begin{cases} 2\omega_{LO} + \omega_{IF} \\ \omega_{IF} \end{cases}$$

If the RF frequency is $\omega_s = \omega_{LO} - \omega_{IF}$, the output frequencies will be

$$w_S \pm w_{LO} = \begin{cases} 2\omega_{LO} - \omega_{IF} \\ -\omega_{IF} \end{cases}$$

The latter output is called the image response of the mixer and it is indistinguishable from the direct response [2.19]. These frequencies are shown in Fig. 2.7.

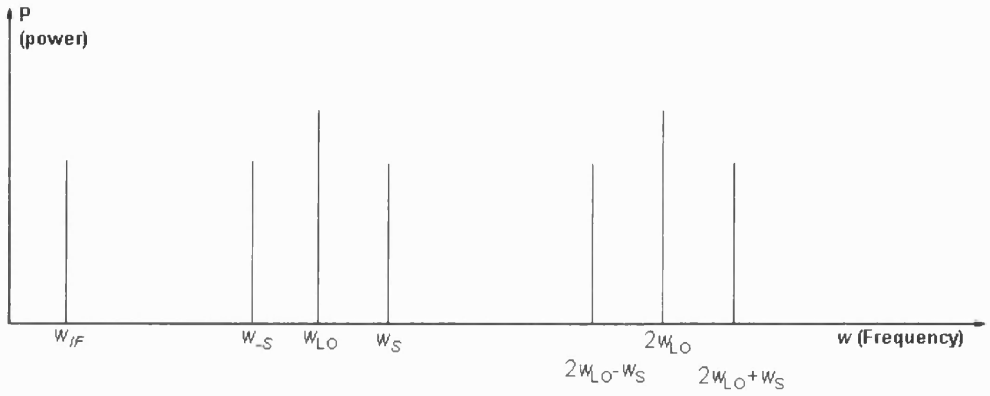

Fig. 2.7 Small-signal mixing frequencies ω_S, ω_{IF} and LO harmonics [2.20].

2.3.2 Sub-harmonic mixer

As discussed in Chapter 1, for many applications, it is difficult, expensive and inconvenient to generate a fundamental frequency local oscillator signal at sub-millimetre wavelengths. To overcome this problem, quite often, a nonlinear mixing element is pumped with half the LO frequency and the RF signal is mixed with the second harmonic of the LO generated in the nonlinear device. Although it is possible to have subharmonic mixing using a single diode, the fundamental mixing response is greater than the second harmonic response in such a mixer. As a result, the conversion loss in such a mixer is greater. Instead, a two diode mixer (anti-parallel configuration), as shown in Fig. 2.8 gives better performance in terms of conversion loss and noise performance. If the diodes are identical, this configuration has three main advantages:

1) reduced conversion loss by suppressing the fundamental mixing products;
2) lower noise figure through suppression of local oscillator noise sidebands and suppression of direct video detection;
3) inherent self-protection against large peak inverse voltage burnout.

This configuration was described by Cohn et al [2.20]. As previously seen the application of a voltage waveform:

$$V=V_{LO}\sin(\omega_{LO}t)+V_{RF}\sin(\omega_S t) \tag{2.17}$$

to the asymmetric diode I-V characteristic results in the diode current having all the frequencies $m f_{LO} \pm n f_S$ (Fig.2.8a). However, in the case of an antiparallel diode pair, as shown in Fig. 2.8b, the diode current contains frequencies for which $m+n$ is an odd integer. The terms for which $m+n$ is even, (i.e., even harmonics, fundamental mixing products ($\omega_s - \omega_{LO}$) and ($\omega_s + \omega_{LO}$), and the DC term), flow only within the diode loop. From Fig. 2.8b, the instantaneous current through the diodes can be written as:

$$i_1 = -i_s\left(e^{-\alpha V}-1\right) \tag{2.18}$$

$$i_2 = i_s\left(e^{\alpha V}-1\right) \tag{2.19}$$

where α is the diode slope parameter given as $\alpha = \frac{q}{\eta kT}$ ($\alpha \approx 38\ V^{-1}$ for a typical high-quality GaAs Schottky barrier diode). Similarly, the differential conductance for each diode may be written as

$$g_1 = \frac{di_1}{dV} = \alpha i_s e^{-\alpha V} \tag{2.20}$$

$$g_2 = \frac{di_2}{dV} = \alpha i_s e^{\alpha V} \tag{2.21}$$

The composite time varying differential conductance g is simply the sum of the individual differential conductance terms:

$$\begin{aligned} g &= g_1 + g_2 \\ &= \alpha i_s\left(e^{\alpha V}+e^{-\alpha V}\right) \\ &= 2\alpha i_s \cosh \alpha V \end{aligned} \tag{2.22}$$

From the above expression, it is clear that g has even symmetry with V, as shown in Fig. 2.8b, and the number of conductance pulses per LO cycle in the antiparallel diode circuit is twice that for a single diode circuit. When this diode pair is pumped with the LO, it modulates the conductance of the diode. Substituting $V = V_{lo}\cos\omega_{lo}t$ into (2.22) yields the following result

$$g = 2\alpha i_s \cosh(\alpha V_{lo} \cos\omega_{lo} t) \tag{2.23}$$

which may be expanded in the following series:

$$g = 2\alpha i_s \left[I_0(\alpha V_{lo}) + 2I_2(\alpha V_{lo}) \cos 2\omega_{lo} t + 2I_4(\alpha V_{lo}) \cos 4\omega_{lo} t + \ldots \right] \tag{2.24}$$

where $I_n(\alpha V_{lo})$ are modified Bessel functions of the second kind. Notice that the conductance components consist of a dc term plus even harmonics of the LO frequency, ω_{lo}. When the applied voltage is

$$V = V_{lo} \cos\omega_{lo} + V_s \cos \omega_s t,$$

the current expression will be:

$$i = g(V_{lo} \cos\omega_{lo} t + V_s \cos\omega_s t) \tag{2.25}$$

$$\begin{aligned} i = {} & A\cos\omega_{lo} t + B\cos\omega_s t + C\cos 3\omega_{lo} t + D\cos 5\omega_{lo} t + E\cos(2\omega_{lo} + \omega_s)t \\ & + F\cos(2\omega_{lo} - \omega_s)t + G\cos(4\omega_{lo} + \omega_s)t + H\cos(4\omega_{lo} - \omega_s)t + \ldots \end{aligned} \tag{2.26}$$

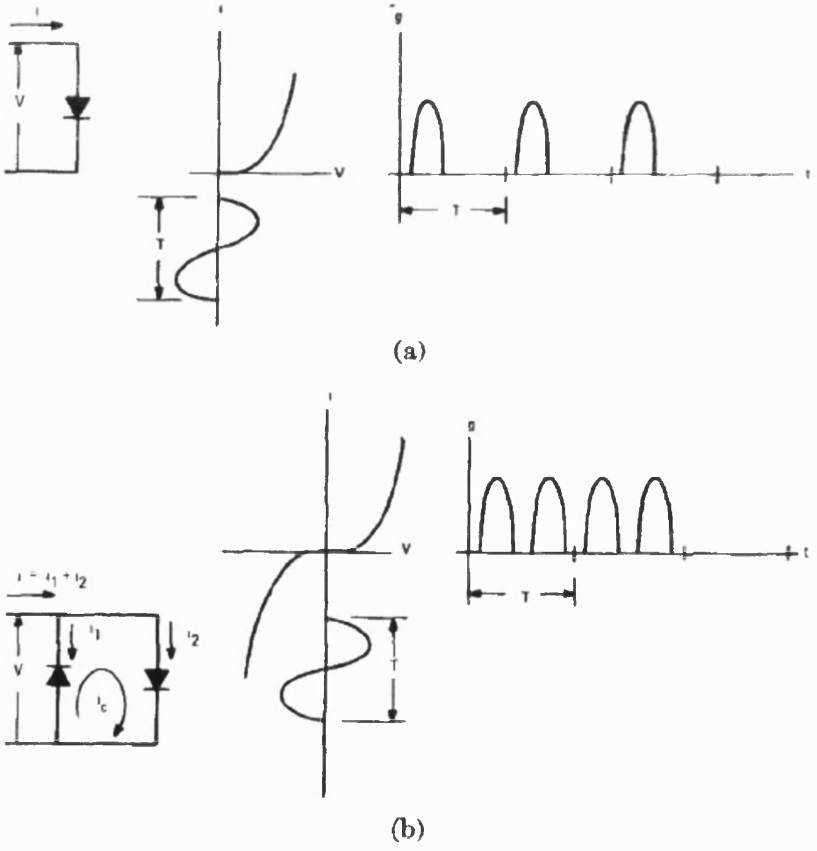

Fig. 2.8 Mixer circuit. (a) Single diode mixer. (b) Antiparallel diode pair mixer [2.20].

It can be seen that the total current only contains frequency terms $mf_{lo} \pm nf_s$ where $m + n$ is an odd integer; i.e., $m + n = 1,3,5....$

In Fig. 2.8b a circulating current i_c is also indicated. This current arises from the fact that Fourier expansions of the individual currents i_1 and i_2 reveal that certain components of each current are oppositely phased. Because of their opposite polarity, these components cancel as far as the external current i is concerned and simply circulate within the loop formed by the two diodes. From Fig. 2.8b, one can mathematically describe this circulating current as

$$i_c = (i_2 - i_1)/2 = i_s[\cosh \alpha V - 1] \tag{2.27}$$

and substituting

$$V = V_{lo}\cos\omega_{lo}t + V_s\cos\omega_s t \tag{2.28}$$

into the expansion for the hyperbolic cosine yields

$$\begin{aligned} i_c &= i_s\left[1 + \frac{(V_{lo}\cos\omega_{lo} + V_s\cos\omega_s t)^2}{2!} + ... - 1\right] \\ &= \frac{i_s}{2}\left[V_{lo}{}^2\cos^2\omega_{lo}t + V_s{}^2\cos^2\omega_s t + 2V_{lo}V_s\cos\omega_{lo}t\cos\omega_s t + ...\right] \\ &= \frac{i_s}{2}\left\{\frac{V_{lo}{}^2 + V_s{}^2}{2} + \frac{V_{lo}{}^2}{2}\cos 2\omega_{lo}t + \frac{V_s{}^2}{2}\cos 2\omega_s t\right. \\ &\left. + V_{lo}V_s[\cos(\omega_{lo} - \omega_s)t + \cos(\omega_{lo} + \omega_s)t] + ...\right\} \end{aligned} \tag{2.29}$$

from which it can be seen that the circulating current only contains frequencies $mf_0 \pm nf_0$, where $m + n$ = even integer

Thus the anti-parallel pair has the advantage of suppressing fundamental and other odd harmonic mixing products and also the even harmonics of the LO. However, it should be kept in mind that the degree of suppression degrades with the imbalance in the diode pair. It should also be noted that the degradation of receiver noise figure due to LO noise sidebands whose separation from the LO (f_{LO}) equals IF (f_{IF}), generate IF noise which only circulates within the diode loop when they mix

fundamentally with the LO; second harmonic mixing of these noise sidebands with the virtual LO ($2f_{LO}$), produces noise which is not within the IF amplifier pass band.

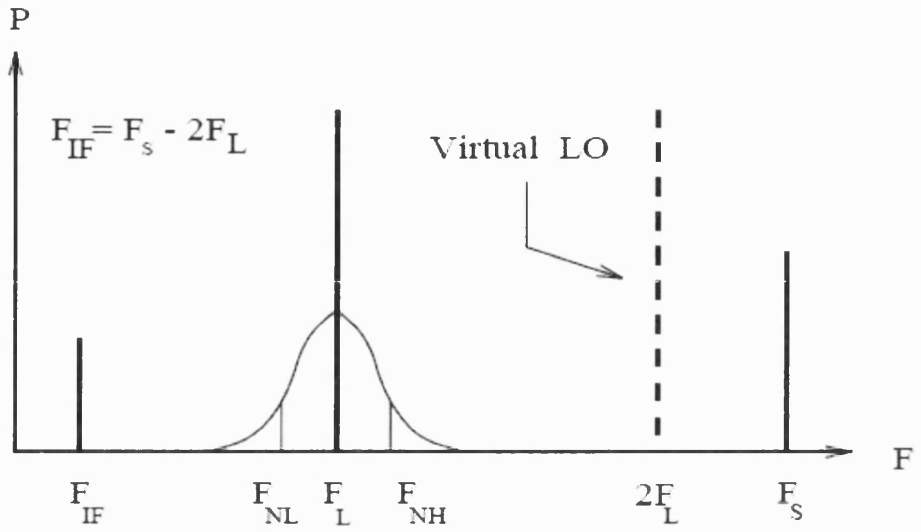

Fig. 2.9 Mixer circuit. (a) Single diode mixer. (b) Antiparallel diode pair mixer [2.20].

Finally, the anti-parallel diode circuit has inherent self-protection against peak inverse voltage, because a reverse biased diode is always in parallel with the forward biased diode, which limits the reverse bias swing to less than the breakdown voltage of the diodes.

2.4 Conversion Loss and Noise Temperature Calculations

The small-signal conversion loss and noise properties of a mixer can be determined in two steps. First, the large-signal voltages and currents produced at the diodes by the LO are determined, and from them the diode conductance and capacitance waveforms. Then, the small-signal conversion loss, input and output impedances, and noise temperature are obtained using linear mixer analysis. Throughout this section the notation and explanation were developed by Held and Kerr [2.21]

2.4.1 The Pumped Diode

The steady-state of the mixer circuit (Fig. 2.10) can be described in terms of the Fourier coefficients of the voltage v_j and current i_e for the large-signal response.

The intrinsic diode C_j and g_d is non-linear and is characterised in the time domain, while the diode series resistance R_s and the embedding impedance Z_e are linear and best represented in the frequency domain.

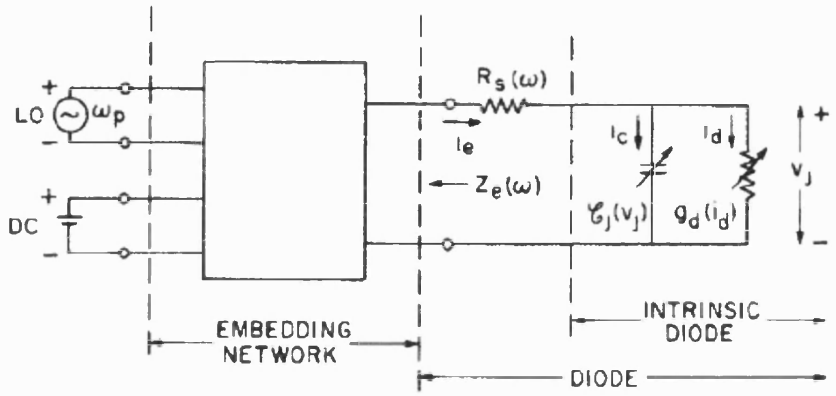

Fig. 2.10 Equivalent circuit of the mixer [2.21].

At the diode the current can be expressed as

$$i_d = i_0\left[\exp(\alpha v_j) - 1\right] \tag{2.30}$$

and

$$i_c = C_j \frac{dv_j}{dt} \tag{2.31}$$

where

$$C_j = C_{jo}\left(1 - \frac{v_j}{\phi}\right) \tag{2.32}$$

and

$$\alpha = \frac{q}{\eta kT}. \tag{2.33}$$

From (2.30), the incremental conductance of the diode is

$$g_d = \frac{di_d}{dv_j} = \alpha(i_d + i_0) \approx \alpha i_d \tag{2.34}$$

The embedding network requires that

$$V_k = -I_{ek}\left[Z_e(kw_p) + R_s(kw_p)\right] \quad k=\pm 2, \pm 3, \ldots, \pm\infty \tag{2.35}$$

$$V_{\pm 1} = V_p - I_{e\pm 1}\left[Z_e(\pm w_p) + R_s(\pm w_p)\right] \tag{2.36}$$

$$V_0 = V_{dc} - I_{e0}\left[Z_e(0) + R_s(0)\right] \tag{2.37}$$

where V_p and V_{dc} are the LO and dc-bias voltages, respectively. The frequency dependence of R_s is due to the skin effect.

A methods for solving the non-linear mixer problem, commonly called the reflection algorithm has been described by Kerr. This algorithm is used in Chapter 4 to determine the conversion loss of diodes having different diameters. In this algorithm the linear and non-linear parts of the circuit are separated, and a specific procedure is used to bring the separate calculations into convergence [2.22].

After the determination of the LO waveforms at the diode the quantities $i_d(t)$, $g_g(t)$ and $C_j(t)$ can be calculated and can be expressed as Fourier series:

$$i_d = \sum_{k=-\infty}^{\infty} I_k \exp(jkw_p t), \qquad I_k = I^*_{-k} \tag{2.38}$$

$$g_d = \sum_{k=-\infty}^{\infty} G_k \exp(jkw_p t), \qquad G_k = G^*_{-k} \tag{2.39}$$

$$C_j(t) = \sum_{k=-\infty}^{\infty} C_k \exp(jkw_p t), \qquad C_k = C^*_{-k} \tag{2.40}$$

These quantities, together with the embedding impedance $Z_e(w)$, determine the small-signal properties of the mixer.

2.4.2 Small-Signal Analysis

The time waveforms for the junction capacitance and conductance are found by substituting $V_k(t)$ from the large-signal analysis into (2.32) and (2.34). The subscript notation for the sideband quantities follows that of Saleh [2.23]; subscript m indicates frequency $w_0 + mw_p$, where w_p and w_0 are the LO and IF frequencies.

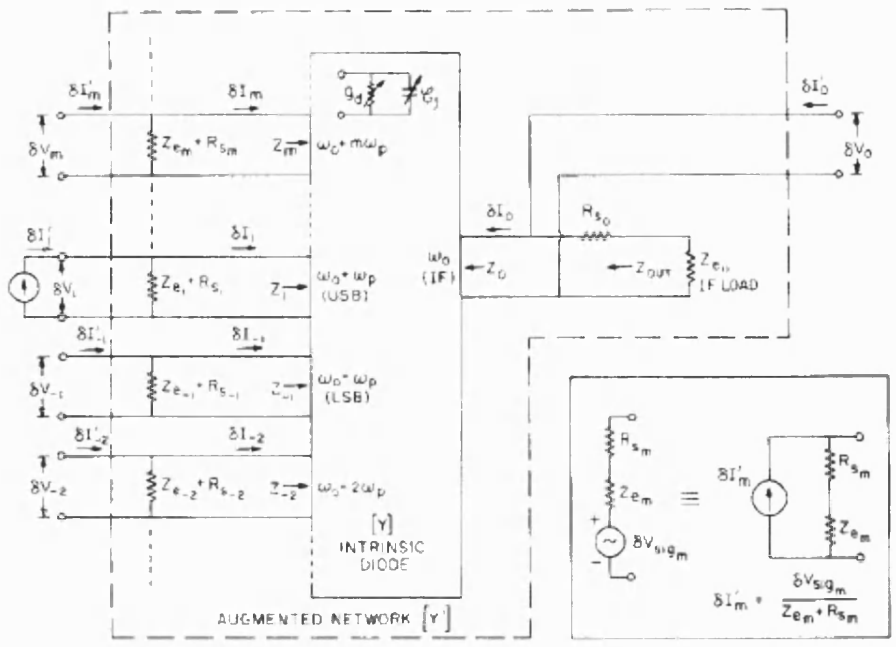

Fig. 2.11 Small signal representation of the mixer as a multi-frequency linear multi-port network [2.21].

Fig. 2.11 shows the matrix which interrelates the various sideband frequency components of the small-signal current and voltage. The voltage and current δV_m and δI_m at port m are the small-signal components at frequency (ω_0 + mω_p) appearing at the intrinsic diode; each port represents one sideband frequency. The conversion matrix Y is the admittance matrix of the intrinsic diode. The augmented network includes all the sideband embedding impedances Z_{em} and is characterised by the augmented admittance Y'. During normal mixer operation the equivalent signal current generator $\delta I'$ is connected to port 1 of the augmented network, the other ports being open-circuited.

The conversion admittance matrix Y is a square matrix defined by

$$\delta I = Y \delta V \tag{2.41a}$$

where

$$\delta I = [\ldots, \delta I_1, \delta I_0, \delta I_{-1}, \ldots]^T \tag{2.41b}$$

and

$$\delta V = [\ldots, \delta V_1, \delta V_0, \delta V_{-1}, \ldots]^T \tag{2.41c}$$

$$
Y \equiv \begin{array}{c} \text{row } \# \\ \vdots \\ 1 \\ 0 \\ -1 \\ \vdots \end{array}
\begin{bmatrix}
 & \vdots & \vdots & \vdots & \\
\cdots & Y_{11} & Y_{10} & Y_{1-1} & \cdots \\
\cdots & Y_{01} & Y_{00} & Y_{0-1} & \cdots \\
\cdots & Y_{-11} & Y_{-10} & Y_{-1-1} & \cdots \\
 & \vdots & \vdots & \vdots & \\
\cdots & 1 & 0 & -1 & \cdots
\end{bmatrix}.
$$

column #

Using the notation given by Salem Y is given by

$$Y_{mn} = G_{m-n} + j(w_0 + mw_p)C_{m-n} \tag{2.42}$$

where G_k and C_k are the Fourier coefficients of the diode conductance and capacitance defined in (2.39) and (2.40).

An augmented Y-matrix can be defined which includes the external terminating impedances Z_{em}. This augmented network Y' does not contain signal sources, the sources are replaced by equivalent current sources $\delta I'_m$ connected across (Z_{em} + R_{sm}). The multiport network and the current sources are outlined by respectively the broken line and inset of Fig. 2.11. The ports of the augmented network are all normally open-circuit.

For the augmented network

$$\underline{\delta I'} = \underline{Y'}\,\underline{\delta V} \tag{2.43}$$

and

$$Y' = Y + diag\left[\frac{1}{Z_{em} + R_{sm}}\right] \tag{2.44}$$

Inverting (2.43) gives

$$\underline{\delta V} = \underline{Z'}\,\underline{\delta I'} \tag{2.45a}$$

where

$$\delta V_i = Z_{ij}'\,\delta I_j' \tag{2.45b}$$

Although an exact representation of the mixer requires an infinite matrix, the highest frequency terms are generally considered to be short circuited by the diode junction capacitance and the capacitances in the diode mount. Previous research [2.24] has shown that limiting the model to frequencies below the fourth harmonic is sufficient for the accurate analysis of typical mixers. The small-signal analysis presented in this section and described by Held and Kerr takes into account the embedding

impedances seen by the diode at any finite number of sidebands and LO harmonics, the voltage-variable junction capacitance and the correlation between the various frequency components of the junction shot noise. However this analysis does not include the correlation of the frequency components of the series resistance noise. This assumption is accurate for devices working at room temperature and up to 220 GHz. For cryogenic or high frequency operation, greater accuracy can be achieved by taking into account the hot-electron noise in the series resistance [2.24]

2.4.3 Conversion Loss

The conversion loss of a mixer is given by:

$$L = \frac{P_{RF}}{P_{IF}} \tag{2.46}$$

This represents the ratio of the available signal power to the IF power delivered to the load. The conversion loss can be expressed as :

$$L = \frac{1}{4|Z'_{01}|^2} \frac{|Z_{e0} + R_{s0}|^2}{\mathrm{Re}[Z_{e0}]} \frac{|Z_{e1} + R_{s1}|^2}{\mathrm{Re}[Z_{e1}]} \tag{2.47}$$

2.4.4 Mixer Noise

The properties of noise in a mixer were well understood early in their history, but a workable accurate noise model was not generated until 1975 [2.21]. Noise in room-temperature millimetre-wave mixers consists almost entirely of shot and thermal noise generated by the mixer diode. The shot noise is shown to have down-converted components which are correlated with one another. Other effects such as hot electron noise and inter-valley scattering noise in GaAs may dominate for large currents or at very high frequencies (above 300 GHz) [2.23]-[2.25] .

An equivalent circuit model of the diode including noise sources is shown connected to the embedding network in Fig. 2.12. Here, $\overline{v_T^2}$ represents the thermal noise source and $\overline{i_S^2}$ the shot noise source.

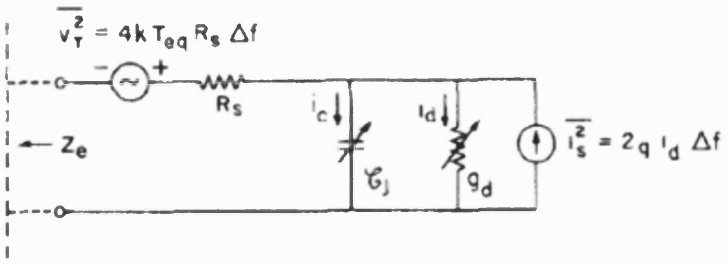

Fig. 2.12 Equivalent circuit model including noise sources [2.22].

Shot Noise:

The diode shot noise given by (2.48) is a function of the instantaneous flow of current i_d across the barrier produce by the LO. Since $i_d(t)$ is periodic, the shot noise current can regarded as a stationary white noise current, modulated in amplitude.

Thermal Noise:

The thermal noise is generated in the series resistance of the diode and it can be regarded as a noise current $\overline{i_T^2}$ derived from $\overline{v_T^2}$ across the terminals of the intrinsic diode. Since R_S is assumed to be time invariant, therefore the thermal noise will have no correlated components.

The total mixer noise temperature is given by:

$$T_M = \frac{\langle \delta V_{N0}^2 \rangle}{4k\Delta f} \frac{|Z_{e1} + R_{s1}|^2}{|Z'_{01}|^2 \,\mathrm{Re}[Z_{e1}]} \tag{2.48}$$

2.4.5 Practical Measurement of Noise Temperature and Conversion Loss

Throughout this research the measurements presented in Chapter 7 were made by acquiring the mixer output power. The noise temperature and conversion loss can be obtained from two measurements made with black body RF loads at two different temperatures. With a liquid nitrogen Temperature black body (T_{cold} = 77 K), the mixer output temperature is designated T_{IFcold}, and with a room temperature black body (T_{hot} = 295 K) the mixer output temperature is designated T_{IFhot}. Assuming no RF loss between the black body and the mixer and a perfect IF impedance match, the output temperature from the mixer is

$$T_{IF(\text{hot or cold})} = \frac{\left[T_M + T_{(\text{hot or cold})}\right]}{L_S} \tag{2.49}$$

where T_M is the mixer noise temperature and L_S is the conversion loss. The mixer noise temperature may be calculated by first defining a Y-factor

$$Y = \frac{T_{IFhot}}{T_{IFcold}} = \frac{(T_{hot} + T_M)}{(T_{cold} + T_M)} \tag{2.50}$$

so that

$$T_M = \frac{(T_{hot} - YT_{cold})}{(Y-1)} \tag{2.51}$$

The conversion loss is simply the ratio of the change in input temperature to the change in output temperature which may be calculated from

$$L_S = \frac{(T_{hot} - T_{cold})}{(T_{IFhot} - T_{IFcold})} \tag{2.52}$$

The noise temperature and conversion loss calculated from mixer output temperature measurements will both be in double sideband values as there is no image rejection in this design. The single sideband values will be approximately twice the double sideband values for both noise temperature and conversion loss.

References – Chapter 2

[2.1] J. Lavergnat, "Radio wave propagation : Principles and techniques,"*Wiley*, 2000.

[2.2] W. Schottky, "Semiconductor theory in the blocking layer," *Naturwissenschaften*, vol. 26, p. 381, December 1938 (translated).

[2.3] N. F. Mott, "Note on the contact between a metal and an insulator or semiconductor," *Proc. Cambridge Philos. Soc.*, vol. 34, pp. 568-572, October 1938.

[2.4] H. A. Bethe, "Theory of the boundary layer of crystal rectifiers," *MIT Radiat. Lab. Rep.*, November 1942, pp. 387-399.

[2.5] A. M. Goodman, "Metal-semiconductor barrier height measurement by the differential capacitance method-one carrier system," *Journal of Applied Physics*, vol. 34, no. 2, pp. 400-409, February 1962.

[2.6] M. T. Faber, J. Chramiec, M. E. Adamski, "Microwave and millimeter diode frequency multipliers," *Artech House, Inc, MA*, 1995.

[2.7] S. M. Sze, "Physics of semiconductor devices," *New York: John Wiley and Sons*, 1969.

[2.8] J. T. Louhi, A. V. Raisanen, "Dynamic shape of the depletion layer of a submillimeter-wave Schottky varactor," *IEEE Transactions on Microwave Theory and Techniques*, vol. 44, no. 12, pp. 2159-2164, December 1996.

[2.9] J. T. Louhi, A. V. Raisanen, "On the modelling and optimization of Schottky varactor frequency multipliers at submillimeter wavelengths," *IEEE Trans. On Microwave Theory and Techniques*, vol. 43, no. 4, pp. 922-926, April 1995.

[2.10] J. T. Louhi, "The capacitance of a small circular Schottky diode for submillimeter wavelengths," *IEEE Microwave and Guided Wave Lett.*, vol. 4, pp. 107-108, 1994.

[2.11] C. R. Crowell, S. M. Sze, "Current transport in metal-semiconductor barriers," *Solid-State Electronics*, vol. 9, pp. 1035-1048, 1966.

[2.12] C. R. Crowell, "Richardson constant and tunneling effective mass for the thermionic and thermionic-field emission in Schottky barrier diodes," *Solid-State Electronics*, vol. 12, pp. 55-59, 1969.

[2.13] C. Y. Chang, S. M. Sze, "Carrier transport across metal-semiconductor barriers," *Solid-State Electronics*, vol. 13, pp. 727-740, 1970.

[2.14] F. A. Padovani, R. Stratton, "Field and thermionic-field emission in Schottky barriers," *Solid-State Electronics*, vol. 9, pp. 428-440, 1966.

[2.15] S. J. Pilkington, *et al.*, "On the Richarson constant of intimate metal-GaAs (111)B Schottky diodes grown by molecular beam epitaxy," *J. Appl. Phys.*, vol. 74, no. 10, pp. 6256-6260, November 1993.

[2.16] WaiFai Yee and H. A. Naseem, "Formation Of Ohmic Contacts To n-GaAs via Heterojunction By Using Indium And Gold" *IEEE*, pp.614-617, 1990.

[2.17] Zhang Wang-rong, Li Zhi-guo, Mu Fu-chen,Wang Li-xin,Sun Ying-hua, Cheng Yao-hai, Chen Jian-xin, Shen Guang-di, "A Rapid Evaluation for Degradation Activation Energy of n-GaAs Ohmic Contacts With and Without TiN diffusion barrier layers", *IEEE proceedings of 8th OPFA 2001*, Singapore,pp.134-137.

[2.18] R. Williams, " Modern GaAs processing methods", Artech House, 1990

[2.19] S.A. Maas, Microwave Semiconductor Devices, 2nd edition, Artech House, 1993.

[2.20] Marvin Cohn, James E. Degenford and Burton A. Newman, "Harmonic Mixing with an Antiparallel Diode Pair", *IEEE transactions on microwave theory and techniques*, vol. MTT-23, N°8, August 1975.

[2.21] D.N. Held and A.R. Kerr, "Conversion Loss and Noise of Microwave and Millimeter-wave Mixers: Part 1 – Theory; Part 2 – Experiment," *IEEE Trans. Microwave Theory Tech.*, MTT-26, pp.49-61, 1978.

[2.22] Stephen A. Maas, " Microwave mixers ", Artech House Inc., 1986

[2.23] A. A M. Saleh, *Theory of resistive Mixers,* Cambridge, MA : MIT Press, 1971.

[2.24] T.W. Crowe and Robert J. Mattauch, "Conversion Loss in GaAs Schottky-Barrier Mixer Diodes", *IEEE Transactions on Microwave Theory and techniques*, Vol. MTT-34, No. 7, July 1986

[2.25] B. Thomas," Etude et réalisation d une tête de reception heterodynes en ondes submillimetrique pour l etude des atmospheres et surfaces de planetes", These de Doctorat, Université Paris 6, 2004.

Chapter 3

Literature Review

The millimetre and submillimetre region of the spectrum is of increasing importance for a wide variety of applications. Scientific, military and commercial applications drive terahertz technology to achieve more mature, broadband and robust devices. This chapter describes the development of nonlinear devices and RF mixers over the last 30 years. The first section presents the different types of detector and describes the transition from whisker diode to today's integrated planar diode. The final section presents the evolution of mixer receivers over the past three decades.

3.1 THz and millimetre-wave mixing elements

Below 100 GHz, electronic devices such as amplifiers, oscillators and mixers are widely available. SiGe offers today a path to fabricate low cost RF transceiver modules. State of the art SiGe HBT's can deliver competitive performance; cutoff frequencies of 130 GHz and maximum oscillation frequencies of 160 GHz has been proven [3.1]. However, since ultimately the speed of a device is directly related to how fast the carrier can be "pushed", silicon-based devices are regarded as slow. The electron and hole velocity under applied electric field for silicon is rather small and limited to about 10^7 cm/s. On the other hand, superconducting tunnel junctions (SIS-junctions), Hot Electron Bolometer (HEB) and III-V compounds semiconductor benefit from far higher mobilities and saturation velocities making them the best choice for high frequency devices. This section presents a few of the major component technologies that have been developed for translating the functionality of lower frequency electronics into the terahertz band.

3.1.1 SIS junctions

Superconductor-insulator-superconductor (SIS) tunnel junctions are the most sensitive heterodyne mixer elements for frequencies from 36 GHz to 950 GHz both in waveguide [3.2] and quasi-optical designs [3.3]. The current flow mechanism in an SIS junction is based on the photon-assisted tunnelling process discovered by Dayem and Martin [3.4] in the early 1960s. The most common SIS junctions are

formed by two niobium (Nb) superconductor contacts separated by an aluminium oxide (AlO_x) insulator. The nonlinear I-V characteristic of the SIS junction is created by the sharp onset of tunnelling of single electron quasi-particles through the insulating barrier.

The first receivers using this effect were developed by groups at the Bell Laboratories, Holmdel and the California Institute of Technology, Pasadena [3.5]

In 2004 Moon-Hee Chung presented a fixed-tuned SIS mixer operating across the 120-180 GHz band with a receiver temperature between 32-131 K [3.6]. Wenlei Shan [3.2] in 2005 reported the design and measurements of a fixed-tuned Nb-based SIS for the Band 8 of ALMA. The mixer (shown in Fig. 3.1) demonstrates a minimum double-sideband receiver noise temperature of 108K at the centre and noise temperatures less than 167 K over the whole 385-500 GHz (Band 8).

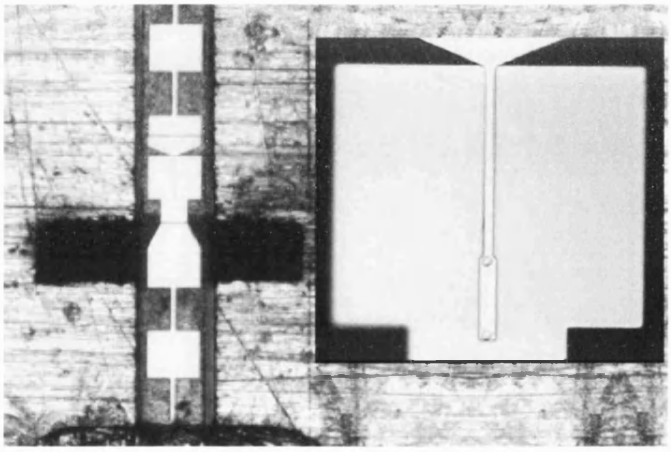

Fig. 3.1 Mounted SIS mixer chip in waveguide block. RF and LO signals are coupled via half-reduced high waveguide. The zoom shows in more detail the twin SIS junction [3.2].

Above 700-750 GHz, which defines the superconducting gap frequency of Nb for good niobium films [3.7], Nb matching circuits for SIS receivers become lossy [3.8]. To extend receiver capabilities beyond the gap frequency of niobium, several directions of research are being explored. Compound superconductors such as NbN [3.3] and TiNbN [3.9] have been investigated for use in SIS junctions, with the goal of replacing the traditional Nb-based structure. However, as with any superconducting material, NbN and TiNbN also have frequency limitations due to the respective superconducting gap frequencies, with limits around 1.21 and 1.23 THz, respectively.

3.1.2 Hot Electron Bolometer mixer

An alternative to the SIS junction for frequencies above 1 THz is the superconducting hot electron transition-edge bolometer (HEB). HEB operation is based on the strong variation of resistance with temperature for a superconductor near its transition temperature.. The bolometer consists of an extremely small microbridge of niobium, niobium-nitride, or niobium-titanium-nitride. Due to the size required, only e-beam lithography techniques can be applied to define in the device the small microbridge structure. Fig 3.2 presents a phonon cooled NbN HEB device [3.10].

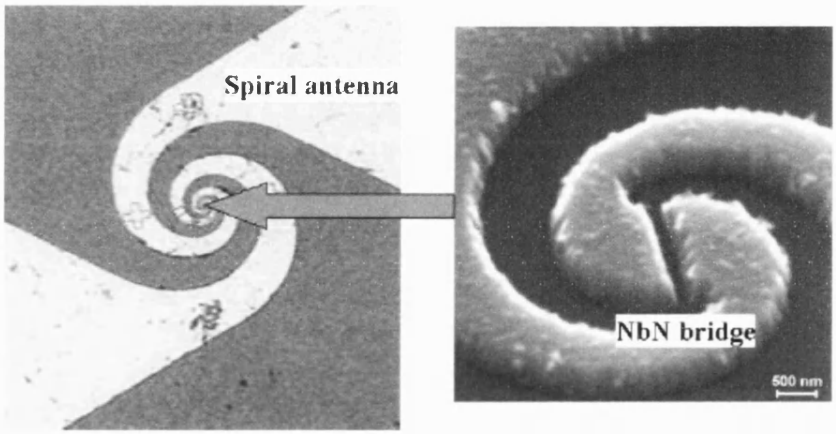

Fig. 3.2 Photograph of a phonon cooled NbN HEB device. The width and length of the NbN bridge are 1.5 μm and 0.15 μm respectively [3.8].

The RF is coupled via a spiral antenna and absorbed by the device, which raises the temperature and the resistance. By biasing the Hot Electron Bolometer it gives a high sensitivity due to the steep Δtemperature/Δresistance slope around the critical temperature of the superconductor. Using this steep transition, extremely sensitive low noise mixers may be achieved. Two varieties of HEB exist, the phonon cooled HEB [3.10], [3.11], [3.12] and diffusion cooled HEB [3.12]. In the first one, heat transfer is dominated by electron-phonon interactions. The second one relies on an electron-electron interaction mechanism.

Both of these superconducting heterodyne devices exhibit the best sensitivity at submillimetre frequencies; unfortunately they require to be cooled down with helium liquid to extremely low temperature to operate. This is an major limitation for

applications requiring compact system. For this reason GaAs devices have been for fifty years the best solid-state technology for compact and room temperature operation and have set the standard for performance.

3.2 From Whisker to planar diodes

For applications where the sensitivity of room temperature detectors is adequate (e.g. planetary science or *in situ* measurement of plasmas), the Schottky diode mixer is the preferred downconverter.

Solid-state semiconductor diodes emerged in the 1940s as superior substitutes to vacuum tubes for use as mixers. In the mid 1960s, GaAs had replaced the Si crystals yielding superior high frequency characteristics. The first devices were made by contacting the GaAs wafer with sharply pointed whisker wires to form point-contact diodes. After establishing the contact, forward bias through the diode generated enough heat to weld the whisker and the semiconductor [3.13]. In 1965 Young and Irvin [3.14] introduced the "honeycomb", a novel contacting technique taking advantage of the progress in vacuum metal deposition and photolithography. An n-type GaAs wafer, covered by a layer of 0.4 μm of SiO_2 was patterned to open an array of diodes having diameters of 3-5 μm. The SiO_2 was etched away and gold was electroplated into the array with 20 μm centre spacing (Fig. 3.3). In this configuration the Schottky diodes share one large common ohmic contact, located on the underside of the chip.

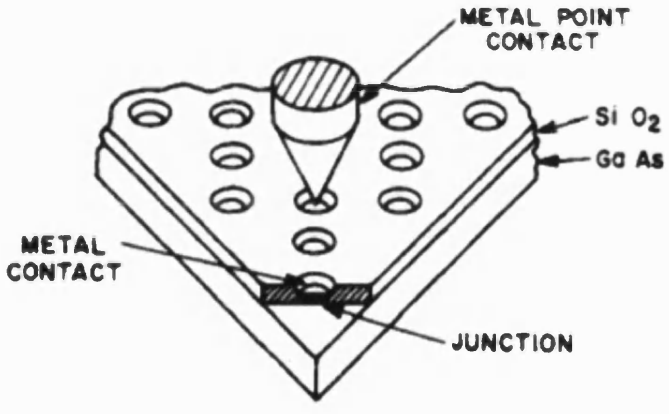

Fig. 3.3 Structure of honeycomb diode[3.15].

The honeycomb Schottky diode produced devices with high quality, predictability, and repeatability, as required for space applications. Over the years, several groups

have fabricated high quality whisker-contacted diodes for operation up to THz frequencies (e.g. University of Virginia, The National Micro-electronics Research Center (NMRC) in Ireland and Tohoku University in Sendai Japan).

In 1977 Kelly [3.16] reported a honeycomb Schottky diode with anodes of diameter 1 μm, having series resistance R_s=10.5 Ω, parasitic capacitance C_{j0}=4.8 fF, ideality of η=1.12, achieving SSB receiver noise temperature T_{rec}=1200 K at 170 GHz. In 1991 the same group presented micron size diodes with sputtered tungsten anodes. These devices were found to be much more stable at high temperature than those having platinum anodes, yielding a significant reliability advantages[3.17].

The Semiconductor Device Laboratory at the University of Virginia has been for more than thirty years a major contributor to advances in Schottky diode technology. A first submicron anode was presented by Bishop and Mattauch in 1988 [3.18]. The Schottky diodes were fabricated on n-type GaAs. First SiO_2 was pyrolytically deposited on the substrate and micron sizes holes were defined in the oxide using photolithography. A small amount of SiO_2 was left to protect the GaAs surface prior to deposition of the anode metallisation. The back of the substrate was thinned down to a thickness of 150 μm and the ohmic contact metallisation (SnNi/Ni/Au) was electroplated. The chip was alloyed at 350 °C for 20 second to form the ohmic contact. The remaining SiO_2 was removed and anodes were formed on the exposed GaAs by electroplating platinum. These diodes were reported to have R_s=12 Ω and C_{j0}=4.5 fF.

As early as 1972 submicron diameter diodes were reported [3.19] (shown in Fig. 3.4).

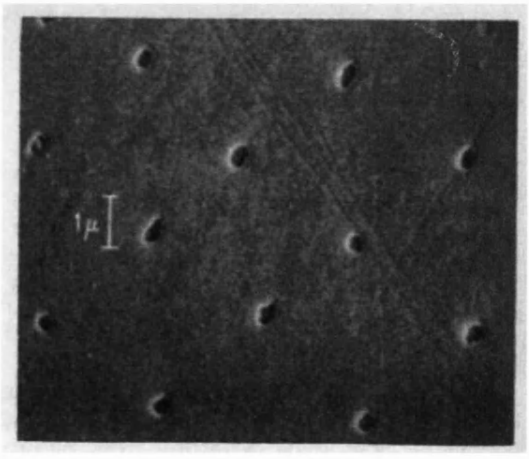

Fig. 3.4 SEM photograph of Schottky barrier diodes on GaAs [3.19].

In 1990 using deep-UV lithography and reactive ion etching Crowe et al [3.20] produced a whisker device with an anode diameter of 0.5 μm, R_s=30 Ω and C_{j0}=0.5 fF. This device, shown in Fig. 3.5, achieved a cut-off frequency of over 10 THz.

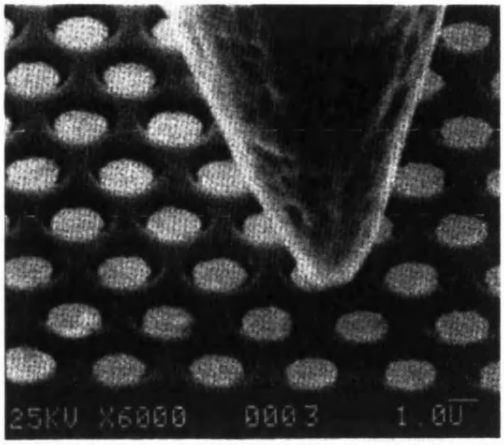

Fig. 3.5 SEM of a honeycomb Structure [3.20].

Although whisker-contacted diodes have been widely used and have provided low conversion loss up to 2.5 THz, they are inherently complex to manufacture and to integrate.

In the mid 1980s a number of laboratories published several different design of a whiskerless diode, adopting a more modern planar diode structure. The main advantages of this planar structure are a more robust design for space missions, simpler component assembly, greater flexibility in the design of the mixer circuits and the possibility of higher levels of system integration. Small area whisker-contacted diodes required great skill and effort to contact and were impossible to incorporate into integrated circuits such as device arrays.

In 1985 McKinney et al [3.21] reported on the design of a whiskerless Schottky diode. In this new design (Fig. 3.6), the ohmic contact pad and anode pad are located on the same side. This geometry decrease the series resistance by reducing the distance between the anode and the ohmic contact. To reduce the shunt capacitance, the area under the finger and anode pads were exposed to proton beam bombardment to insulate the doped GaAs. This resulted in a robust planar device.

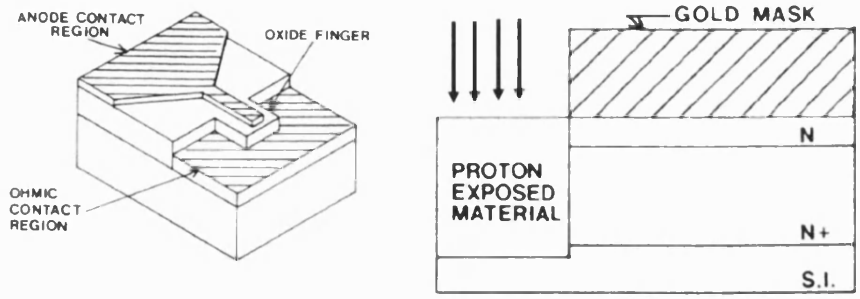

Fig. 3.6 Planar diode structure [3.21].

In 1987 W. L. Bishop [3.22] reported a new design for a whiskerless Schottky diode. This design had the advantage of using an etched surface channel to minimise the shunt capacitance (Fig. 3.7). This device achieved both low junction capacitance due to the 2.5μm diameter anode and low shunt capacitance. The capacitance values were respectively C_{jo} = 5 fF and C_{shunt} = 13 fF. and series resistance R_S = 5 Ω. Using this diode, a SSB mixer noise temperature of 950 K and SSB mixer conversion loss of 6.4 dB was reported at 110GHz [3.22].

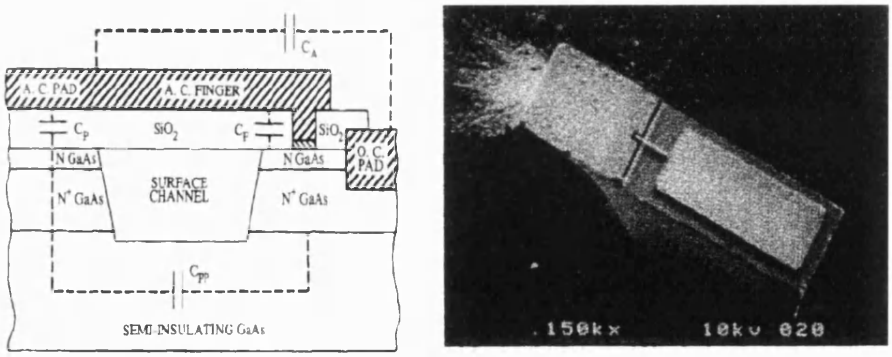

Fig. 3.7 Cross section and SEM of surface channel Schottky diode [3.21].

The basic structure shown in Fig. 3.7 introduced for the first time the air-bridge diode design, eliminating the need for costly and inherently lower resolution proton bombardment. The diode characteristics were as good as the best conventional whisker-contacted diodes and could operate successfully at 77 K, demonstrating the mechanical stability of the air-bridge diode. Furthermore, the planar diode offered predictability and consistency of electrical characteristics which improved accuracy of the mixer design.

In 1993 Siegel [3.23] reported experiments on a planar air-bridge diode using an anti-parallel configuration. The measurements on the subharmonically pumped waveguide mixer were carried out at 215 GHz. The device proved to perform as well as their whisker-contacted counterparts up to 200 GHz.

The same year a quasi-vertical Schottky diode design was proposed by Hartnagel [3.24]. The main idea of the quasi-vertical Schottky diode was to transfer the advantages of the whisker geometry to a planar structure (Fig. 3.8).

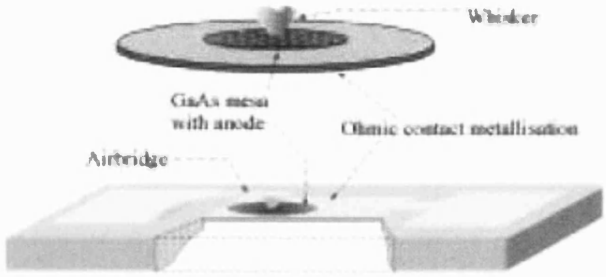

Fig. 3.8 Structure of the quasi-vertical planar Schottky diode [3.24].

This structure reduces the lateral dimension of the of the device therefore reducing the series resistance. Fig. 3.9 gives a comparison of the series resistance of a substrateless diode and a planar surface channel diode for identical diode parameters.

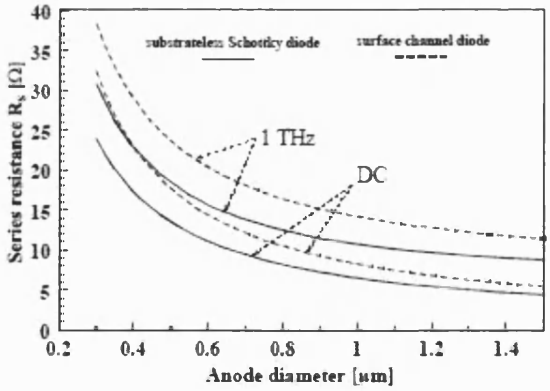

Fig. 3.9 Series resistance of different diode geometries [3.23].

Fig. 3.6 shows a reduction of the series resistance of about 20-30 %.

In 2005, the same research group presented a new Schottky diode structure, the Whisker Integrated Diode (WID) [2.25] (Fig. 3.10).

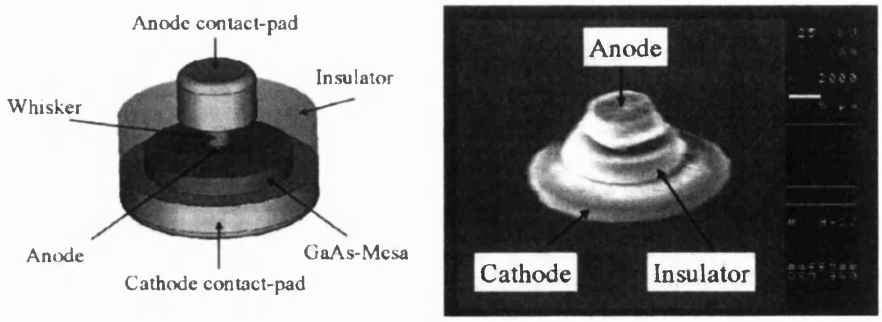

Fig. 3.10 3D sketch and SEM-picture of a fabricated WID-structure [3.24].

The structure consists of 3 major parts, anode, cathode and insulator. The anode includes the anode contact pad and the anode contacting-whisker contact, made by electroplating deposition of Pt. The cathode supports the anode and on the opposite side contains the ohmic contact-pad. The insulator made of SU8 ensures the mechanical stability of the structure.

The advantage of WID geometry compared to the planar structure comes from the vertical current flow between the cathode and the ohmic contact. This uniform field distribution will reduce additional noise due to locally-crowded high current densities which are present in the planar structure. The small geometry allows proper impedance matching as well as a reduction in contacting whisker length, minimising the parasitic inductance.

In recent years interest has shifted to integrated submillimetre circuits such as JPLs GaAs monolithic membrane-diode (MOMED) [2.26]. The concept of MOMED and submillimetre integrated circuits in general is to merge the planar Schottky diode and RF membrane diode circuitry to produce mixer or multiplier circuits. These devices have proven to be easier to fabricate and assemble.

3.3 Evolution of Mixer circuits

Over the course of the last half-century, diode technology has achieved maturity. This evolution has also driven modifications and simplifications of the mixer circuit. The following section reviews fifty years of development of mixer circuits.

One of the most common mixer configurations in the millimetre and more specifically in the submillimetre region of the spectrum is the corner cube mixer.

As the frequency increases, the dimensions of waveguide structures are extremely difficult to control and fabricate. An open radiating structure consisting of a long

wire can provide the necessary interface from free space to the mixing element. The familiar long wire antennas are by definition several wavelengths long, providing a simple way of achieving some directivity along with simplicity of design. One radiating lobe can be achieved by placing the wire close to the ground plane or reflecting plane. The RF signal and local oscillator are coupled to the antenna and to the diode. The honey-comb Schottky diode is placed at the base of the 4 wavelengths long wire antenna. The wire is placed at 0.93λ from the corner cube apex to provide the desired radiating pattern. A typical radiation pattern is sketched in Fig. 3.11.

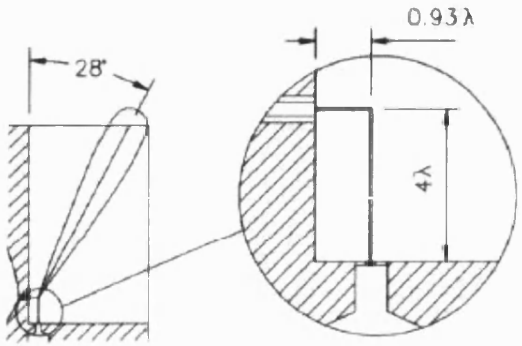

Fig. 3.11 Typical corner cube configuration and radiation pattern [3.27].

At the end of the long wire a diode chip or a beam-lead diode is placed and all high frequencies should be de-coupled at this point. The high frequency is effectively de-coupled at the capacitor formed by the strangled and of the coaxial section. The IF+DC connections are made through an appropriate diplexing structure.

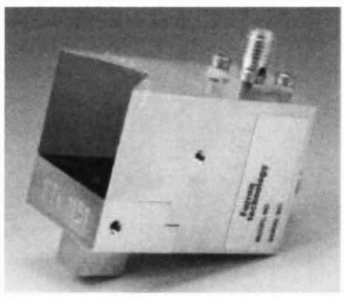

Fig. 3.12 Corner cube Mixer Model CMB-3 from Farran Technology [3.30].

The corner cube is fabricated in two parts; the top contains the corner cube open structure and the bottom has the IF/DC SMA connector. The corner cube reflector is a critical part to be constructed and this is commonly electroformed.

As early as 1977, using the corner cube configuration, McColl reported measurements at 7.2 THz using a submicron Schottky diode barrier mounted in this open, non-tunable mount [3.27]. For many years these structures have demonstrated the best conversion loss at the highest frequencies. Unfortunately, the optical coupling efficiency of the corner cube is only 50 %, so that half of the signal power and half of the LO is unable to reach the diode.

Waveguide structures have the advantage that they couple up 90 % of the incident power. An exploded view of a typical crossed-waveguide configuration from the mid-1960s is presented in Fig.3.13 [3.28]. The crossed waveguide diode mounts were fabricated by electroforming techniques. The signal waveguide was integrated with a pyramidal horn antenna. The diode junction was formed in the signal waveguide between a wafer of n-doped gallium arsenide and an electrolytically-pointed phosphor bronze whisker.

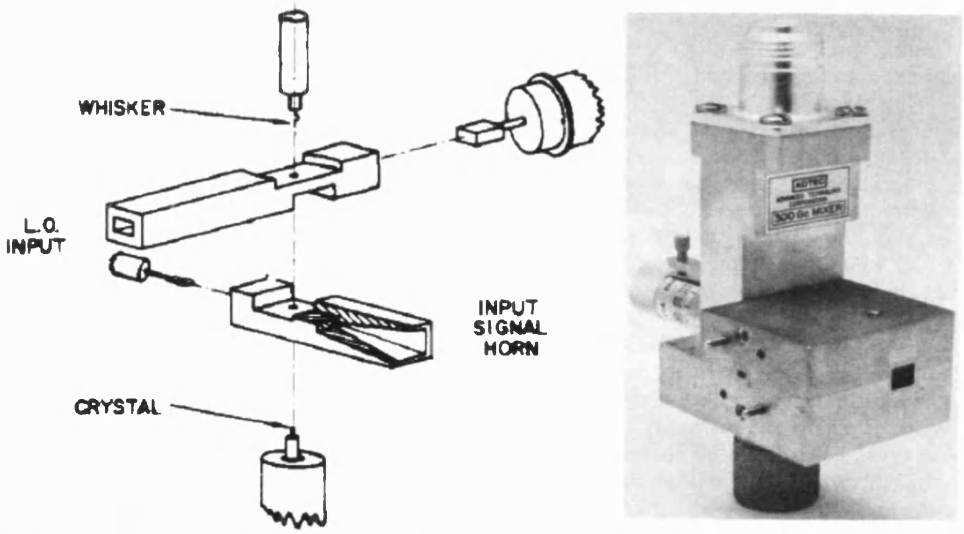

Fig. 3.13 Exploded view of cross waveguide device and picture of a 300GHz Fundamental mixer with integral directional coupler horn [3.28].

Fig. 3.14 summarises a number of different harmonic mixers fabricated at frequencies ranging from 90 to 600 GHz [3.29]. The conversion loss measurements showed a degradation of performance of 3dB when second harmonic mixing was used instead of fundamental mixing. Third harmonic mixing brought an extra 4dB loss compared to second harmonic mixing.

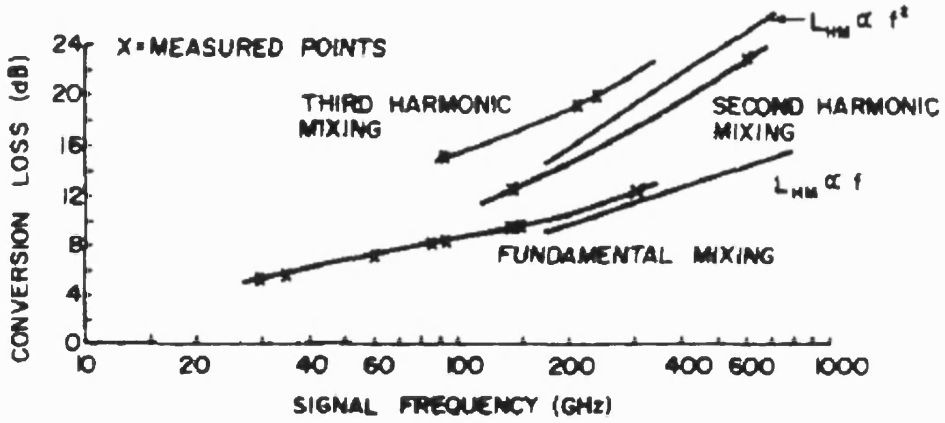

Fig. 3.14 Conversion loss of fundamental and harmonic mixers as a function of frequency [3.29].

In 1975 Kerr[3.31] introduced a reduced-height waveguide structure in the vicinity of the whisker diode. This quarter height waveguide proved to be necessary to obtain a good match between the diode impedance and the mixer block embedding impedance. Two different structures were fabricated, one working at room temperature (Fig. 3.15), and a second one suitable for cryogenic operation (Fig. 3.16 (a)). For cryogenic operation the diode was mounted on a quartz mounting structure (Fig. 3.16 (b)).

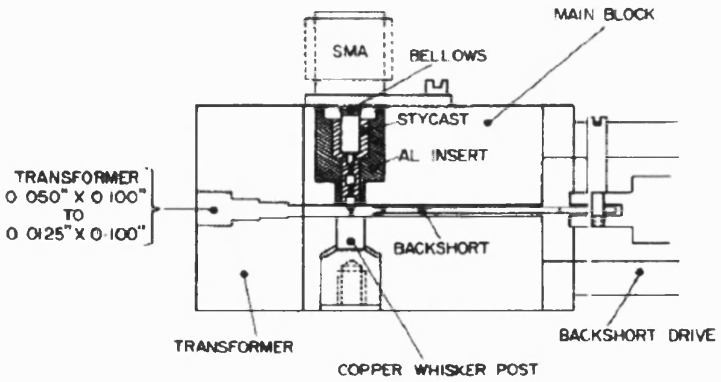

Fig. 3.15 Cross section of the room temperature mixer[3.31].

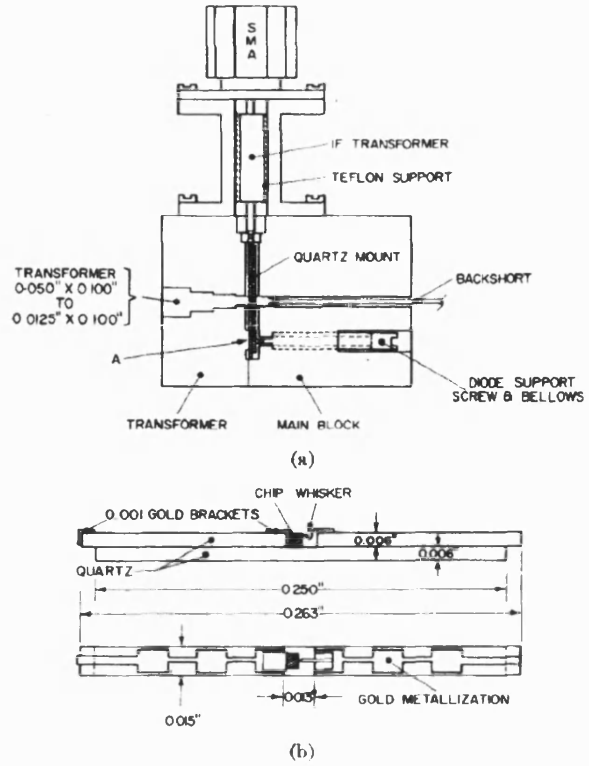

Fig. 3.16 Cryogenic mixer. (a) Cross section of the mixer. (b) Quartz diode mount [3.31].

The SSB conversion loss and SSB noise temperature for the mixer operating at room temperature at 115 GHz were reported to be respectively 5.5 dB and 500 K, with a 1.4 GHz IF. The SSB conversion loss and SSB noise temperature for the mixer operating at 77 K or 18 K were reported to be respectively 5.8 dB and 300 K. The mixers were used on the National Radio Astronomy Observatory 's 36-ft radio telescope at Kitt Peak, Arizona.

In 1978 Schneider [3.32] presented one of the first subharmonically pumped (SHP) mixers working between 47-110 GHz and using notch-front diodes compatible with strip transmission line. The SHP mixer provides the following advantages:

1) The thin-film stripline medium suppresses waveguide modes at harmonics of the LO pump frequency.

2) The mixer can be tuned for SSB or double side Band (DSB).

3) The pump frequency is half of the RF signal.

4) The circuit does not require a DC return path.

5) Separation of the signal and the pump is inherent to the SHP mixer design.

Fig. 3.17 presents the stripline RF circuit for the 50 GHz mixer. The circuit consists of a WR15 waveguide section for the signal, a waveguide-to-stripline transition, a low pass Chebyshev stripline filter to block RF leakage to the LO and IF port, a pair of Schottky diodes, transition from the WR28 waveguide pump to the stripline and finally a hammerhead low pass filter to block the RF signal and collect the IF.

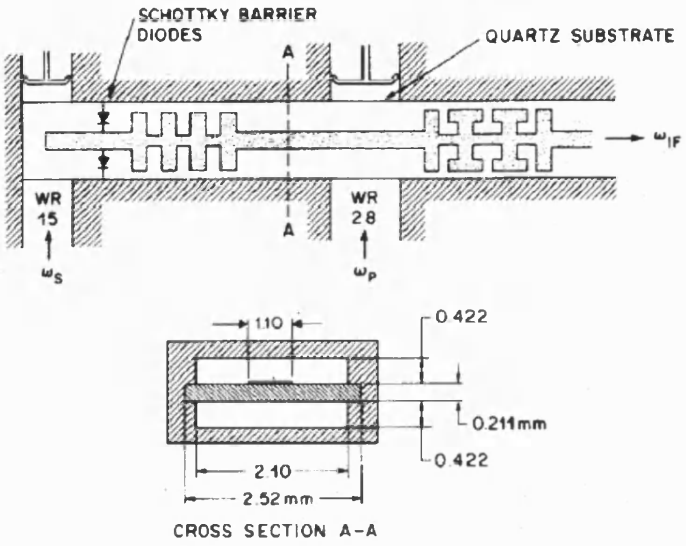

Fig. 3.17 Top view and cross-sectional view of the 50GHz stripline circuit with the signal and pump waveguide inputs ports [3.32].

The SHP mixer could be operated as a SSB or DSB mixer by adjusting the waveguide backshort and an H-plane waveguide short (Fig.3.18).

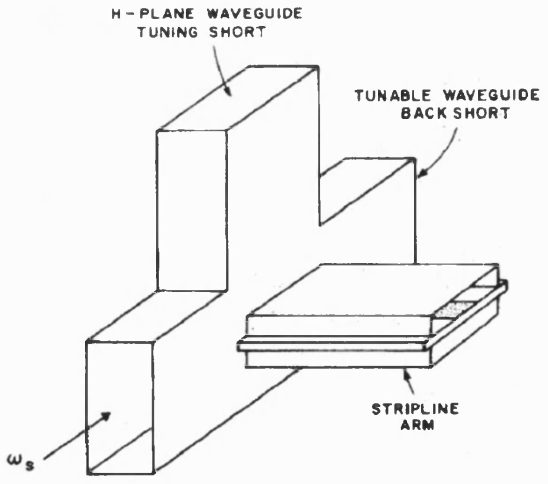

Fig. 3.18 Transition from signal waveguide to stripline circuit with a tunable waveguide backshort and a H-plane tunable short for matching the signal and rejecting the image frequency [3.32].

Fig. 3.19 presents the measured conversion loss and SSB noise figure of the receiver. A conversion loss of 5.5 dB and a SSB receiver noise figure of 10.9 dB were reported at 95 GHz showing good pump rejection.

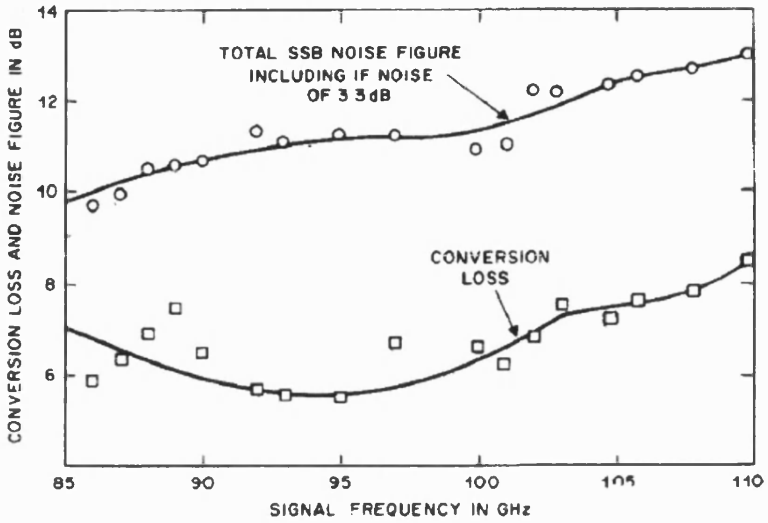

Fig. 3.19 Total SSB noise figure, including a 3.3 dB IF noise contribution, and conversion loss of the down converter from 86 to 110 GHz. The data point were obtained by adjusting the tunable shorts for optimum noise figure at each frequency [3.32].

A major landmark was the introduction of split-block mixer and planar Schottky diodes in the early 1990s. The introduction of high quality planar Schottky diodes, as mention in the previous section, had enabled new approaches in millimetre and submillimetre-wave devices. In 1991 Mattauch [3.33] presented measurements showing that discrete planar integrated diodes could perform as well as whisker contacted diodes. Fig 3.20 presents a performance comparison between a whisker and a surface channel diode (planar air-bridge Schottky diode) [3.33].

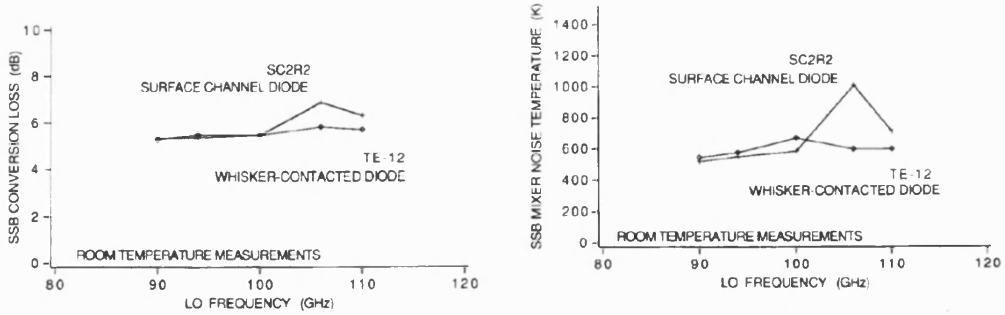

(a) (b)

Fig. 3.20 Comparison of surface channel versus whisker contacted diode. (a) SSB mixer conversion loss versus frequency, (b) SSB mixer input noise temperature versus frequency [3.33].

In 1993 Siegel [3.34] reported an antiparallel-diode pair mixer in a split-block waveguide mixer. The mixer block used a traditional configuration where the microstrip crosses the RF waveguide and LO waveguide and the RF and LO waveguide are perpendicular to each other. A quartz microstrip contained the planar diodes and provided the different RF filters to provide adequate isolation between the IF, LO and RF signals. Apart from underneath the RF and LO antennas, the back-side of the quartz was metallised to facilitate soldering in the cavity. A DC return for the IF signal was provided by a stub present at the LO side of the microstrip. The diodes were suspended in the middle of the signal waveguide. Fig 3.21 (a) presents the 215 GHz mixer block and (b) the quartz filter.

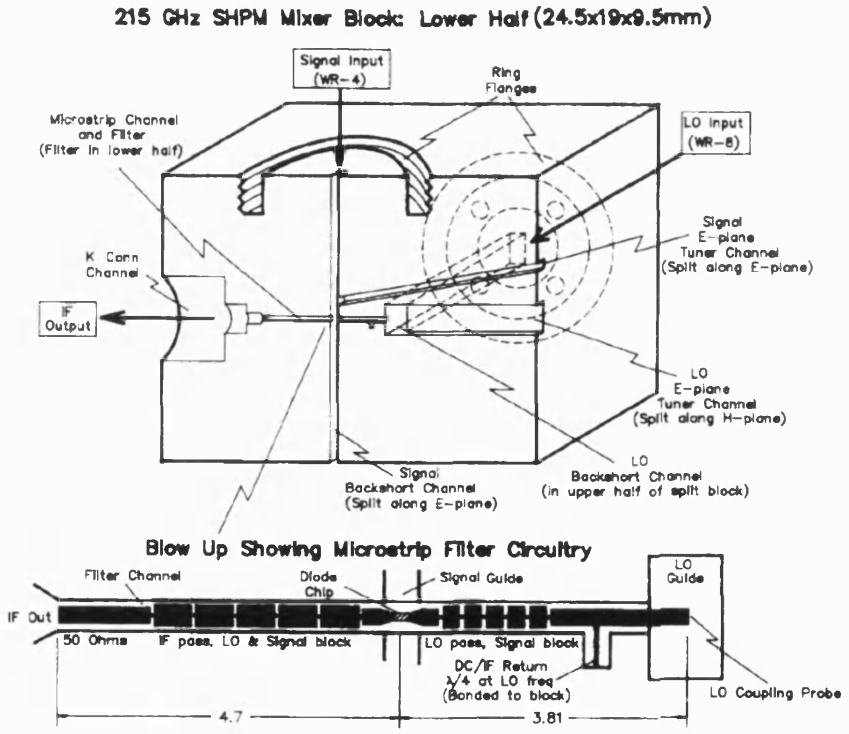

Fig. 3.21 (a) Schematic of the 215GHz SHP crossed waveguide mixer block, (b) microstrip filter circuit [3.34]

For many years the conversion loss results presented by Schneider [3.32] in 1978 were unmatched. Using the same configuration, Siegel reported slightly better results using planar Schottky diodes. Fig 3.22 presents the measurements for different planar diode dimensions. The different diode parameters are reported in Table 3.1.

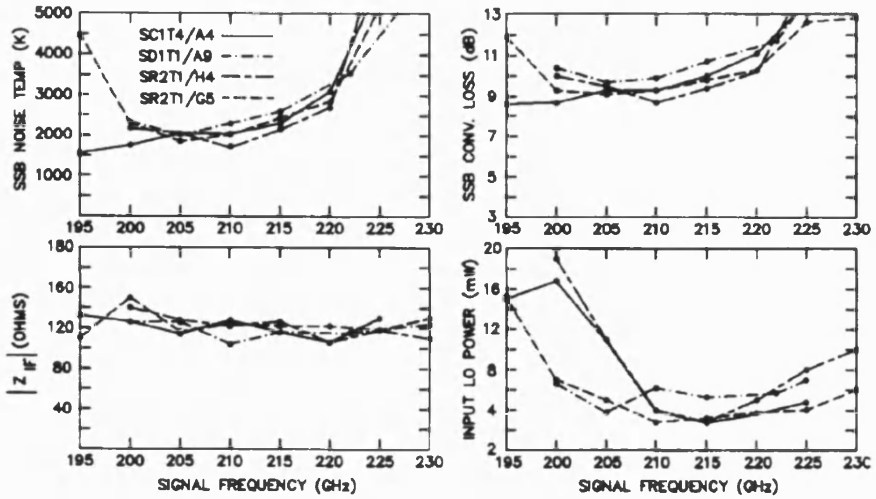

Fig. 3.22 Measured room temperature mixer noise, conversion loss, magnitude of the IF output impedance, and required LO power between 195 and 230 GHz for five diodes whose characteristics are give in table 3.1 Results are give for a IF frequency of 1.4 GHz.[3.34]

The measurements shown in Fig. 3.22 were reported and optimised for lowest noise temperature at each frequency using two backshorts and two E-plane tuners. The noise and conversion loss were measured between the input signal feed horn and the IF output K-connector. In all cases the SSB values were obtained by doubling the DSB results.

Designation diode	mixer	filter	Description	C_{j0} fF	ϕ_b V	η	R_s Ω	I_{sat} 10^{-16}	Anode Diam.	Finger lgth	Bond Pad w × l (μm)
SC1T4/A4	200B4	1A	Small area all GaAs	3.0	1.09	1.28	11.9	2.5	1.4 μm	20 μm	30 × 50
			80w × 200l × 50t (μm)	3.0	1.07	1.25	12.6	1.4			
SD1T1/A9	200B3	2A	Large area all GaAs	3.0	1.09	1.28	10.7	2.5	1.4 μm	50 μm	120 × 100
			120w × 260l × 80t (μm)	3.0	1.08	1.25	12.0	1.2			
SR2T1/H4	200B4	2A	Thinned GaAs/Quartz	3.0	1.08	1.26	6.8	2.2	1.2 μm	50 μm	130 × 50
			130w × 240l × 100t (μm)	3.0	1.06	1.22	7.7	1.3			
SR2T1/G5	200B4	2A	Large area thinned	3.0	1.09	1.25	8.1	1.5	1.2 μm	50 μm	130 × 50
			GaAs no substrate	3.0	1.07	1.22	7.3	0.9			

Notes: All diodes were fabricated at the University of Virginia, Semiconductor Device Laboratory (see [14] for details). Diode parameters (except C_{j0}) are derived from the measured dc I–V curves after mounting. Parameters for both diodes are given. Values of C_{j0} and anode diameter are the nominal for the processed diode wafer. Filters 2A and 1A differ in having diode bonding pads of 100 and 30 μm wide and gaps of 100 and 40 μm, respectively. Mixers 200B3 and 200B4 are nominally identical.

Table 3.1 Diodes used for the measurements shown in Fig. 3.22 [3.34].

This SHP mixer configuration, which proved to be more robust than the whisker diode approach, was the direction that space-born instruments would take for several years. Two SHP mixers working at 240 GHz and 640 GHz using the same configuration were reported and flight-qualified to be used in NASA's Mission to Planet Earth [3.35]. The 200 GHz mixer was reported to have an input noise temperature 30 % lower than the best whisker-contacted diode subharmonic mixers.

Although planar diodes and split-block mixers have facilitated the fabrication of submillimetre mixers, the circuits require backshorts and E-plane tuners to achieve best performance. Furthermore, a diode chip that is fabricated separately from the substrate needs to be bonded with precision. Due to the size of the diode chip (300 x 90 x 75 μm) this task requires high skills. This process involves soldering the chip in place which can damage the fragile electrostatically-sensitive devices and bring some additional series resistance.

A method to overcome the flip-chip-bonding is to create the passive RF circuit substrate out of the GaAs material. This monolithic approach avoids the need for soldering and provides accurate positioning of the diodes with the rest of the circuit. The process has now become completely planar, i.e. diodes, filters and microstrip transmission lines can all be formed on the semiconductor chip using one photolithographic mask. This planar process also has the advantage of producing multiple circuits simultaneously giving higher yields and more reproducible devices. The introduction of this monolithic approach result in an increase of the parasitic capacitance in the circuit due to the high dielectric constant of the GaAs. However, by use of selective wet etching and dry reactive ion etching (RIE), the amount of GaAs present in the integrated mixer circuit and hence RF losses can be minimised.

A first monolithic membrane-diode structure was reported in 1999 by Siegel [3.26]. The 2.5 THz Schottky diode mixer was fabricated on a GaAs substrate, thinned down to a thickness of 3 μm. The fabrication of the membrane device required a normal epi-layer structure for the diode and a specific sandwich of AlGaAs for etch stop, followed by a 3 μm semi-insulating layer which will acted as the membrane material and a second etch stop layer. The membrane was formed using a front-side RIE and backside wet etching. Fig. 3.23 shows the membrane device.

The circuit and device implementation presented above was the starting point for the research described here. The same concepts could be applied to fabricate a subharmonic pumped mixer using integrated planar Schottky diodes. Furthermore using today's modelling capabilities a fixed-tuned membrane mixer could be designed.

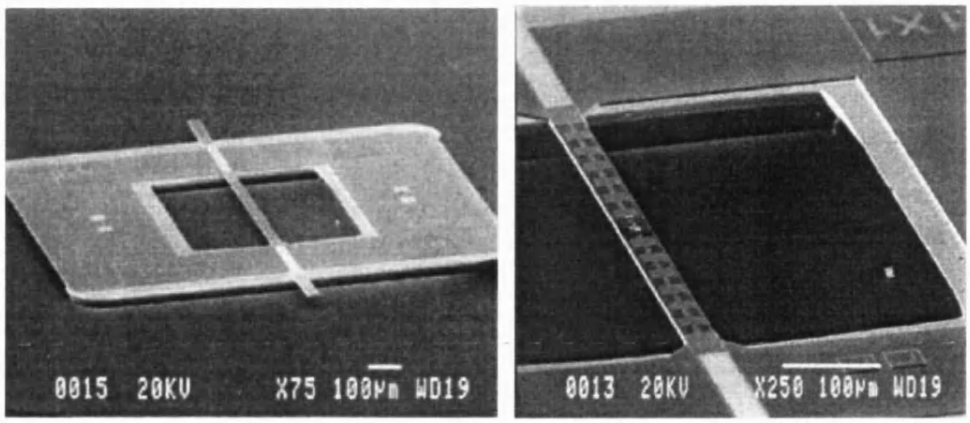

Fig. 3.23 SEM micrographs of completed membrane and frame with 2.5 THz Schottky diode and RF low-pass filter structure. Frame dimensions are 1 mm x 1.4 mm x 50µm thick. Membrane is 36 µm x 600 µm x 3 µm thick [3.26].

Chapter 3 – References

[3.1] A. Schuppen, U. Erben, A. Gruhle, U. Konig,"Enhanced SiGe Heterojuntion Bipolar transistors", *IEDM Tech. Dig.*, pp. 743-746, 1995

[3.2] Wenlei Shan, Takashi Noguchi, Shengcai Shi, and Yutaro Sekimoto, "Design and Development of SIS Mixers for ALMA Band 8", *IEEE Transactions on Applied Superconductivity*, Vol. 15, No. 2, June 2005.

[3.3] Yoshinori Uzawa, Akira Kawakami, Shigehito Miki, and Zhen Wang," Performance of All-NbN Quasi-optical SIS Mixers for the Terahertz Band", *IEEE Transactions on Applied Superconductivity*, Vol. 11, No. 1, June 2001.

[3.4] A. H. Dayem and R. J. Martin, "Quantum interactions of microwave radiation with tunnelling between superconductors," *Phys. Rev. Lett.*, vol.8, pp. 246-248, Mar. 1962.

[3.5] G. J. Dolan, T. G. Philips, and D. P. Woody," Low Noise 115GHz mixing in superconductor oxide barrier tunnel junctions," *Phys. Rev. Lett.*, vol.34, pp. 347-349, Mar. 1979.

[3.6] Moon-Hee Chung, Channghoon Lee, Kwang-Dong Kim, Hyo-Ryoung Kim, "Development of an SIS mixer over 120-180GHz Band", *Astronomy, Atmospheric and Environmental Science*, p1.72, 2004.

[3.7] James W. Lamb, "Millimeter receiver technology for a large array", *Proceedings of the workshop on large millimeter arrays*, 11-Dec 1995.

[3.8] C.E. Honingh, K. Jacobs, S. Haas, D. Hottgenroth and J. Stutzki, "Niobium SIS mixers at 490GHz, 690GHz and 810 GHz", *IEEE transactions on applied superconductivity*, Vol. 5, N°2, June 1995.

[3.9] B.D. Jackson, N.N. Oisad, G. de Lange, A. M. Baryshev, W. M. Laauwen, J.- R. Gao and T. M. Klapwijk, "NbTiN/SiO_2/Al tunning circuits for low-noise 1 THz SIS mixers", *IEEE transactions on applied superconductivity*, Vol. 11, N°1, March 2001.

[3.10] L. Jiang, J. Li, W. Zhang, Q.J. Yao *et al*, "Characterization of NbN HEB Mixers Cooled By a Close-Cycled 4 Kelvin Refrigerator", *IEEE transactions on applied superconductivity*, Vol. 15, N°2, March 2005.

[3.11] A. Skalare, W. R. McGrath, B. Bumble and H. G. LeDuc, " A heterodyne receiver at 533GHz using a diffusion-Cooled superconducting Hot Electron Bolometer Mixer", *IEEE transactions on applied superconductivity*, Vol. 5, N°2, June 1995.

[3.12] Aaron M. Datesman, Jian Z. Zhang, and Arthur W. Lichtenberger, " A new Fabrication Technique for Ultra-small Diffusion-Cooled Hot-Electron Bolometers", *IEEE transactions on applied superconductivity*, Vol. 9, N°2, June 1999.

[3.13] H.C. Torrey, *et al*, "Crystal Rectifiers", *MIT Rad Lab Series*, Vol.15, McGraw Hill, NY, 1948

[3.15] D.T. Young and J. C. Irvin, "Millimeter frequency conversion using Au-n-type GaAs Schottky barrier epitaxial diodes with a novel contacting technique," *Proc. IEEE*, vol. 53, pp. 2130-2131, Dec. 1965.

[3.16] Vizard, D. R., Keen, N. J., Kelly W. M. and Wrixon, G. T., "Low noise Millimiter-Wave Schottky Barrier Diodes with Extremely low local Oscillator Power requirements", *Microwave Symposium Digest, MTT-S International*, Vol. 79, Issue 1, pp81-83, Apr. 1979.

[3.17] Q. P. Pham, W. M. Kelly and J. O'Brien, "Noise Reduction in sputtered W/GaAs Schottky junctions", *Int. J. of IR and MM Waves*, vol.12, no.9, 1991.

[3.18] L. K. Seidel and T. W. Crowe, "Novel GaAs Schottky Barrier Diodes Structures", *Proc. IEEE*, pp. 149-153, Apr. 1988.

[3.19] M. McColl, W. A. Garber, M. F. Millea, "Electron Beam fabrication of submicrometer diameter mixer diodes for millimeter and submillimeter wavelength", *Proceeding of the IEEE*, Vol. 60, Issue 11, pp. 1446-1447, Nov. 1972.

[3.20] T. W. Crowe, R. J. Mattauch, H. P. Roser, *et al* "GaAs Schottky diodes for THz mixing Applications", *Proc. IEEE*, Vol. 80, Issue 11, pp.1827-1841, Nov., 1992.

[3.21] K. McKinney, R. J. Mattauch, W. L. Bishop, "Design, Fabrication, and Performance of a Whiskerless Schottky diode for Millimeter and Submillimeter wave applications", *Proc. IEEE*, pp. 111-115, 1985.

[3.22] W. L. Bishop, K. McKinney, R. J. Mattauch, T. Crowe, G. Green, "A Novel Whiskerless Schottky Diode For Millimeter And Submillimeter Wave Application ", *IEEE MTT-S Digest*, 1987.

[3.23] A. V. Räisänen, D. Chouldhury, R. J. Dengler, J. E. Oswald, and P. H. Siegel, "A Novel Split-Waveguide Mount Design for Millimeter and Submillimeter-wave Frequency Multipliers and Harmonic Mixers", *IEEE Microwave and Guided Wave letters*, Vol. 3, No. 10, October 1993.

[3.24] Chih-I Lin, A. Simon, M. Rodriguez-Gironés, H. L. Hartnagel, P. Zimmermann, R. Henneberger, " Planar Schottky Diodes for Submillimeter Waves Applications", *Terahertz Electronics Proceedings*, p. 135-138, Sept. 1998.

[3.25] O. Cojocari, C. Syldo, H. –L. Hartnagel, " WID: A New Schottky-Structure Design for THz-Applications", *Infrared and Millimeter Waves and 13th International Conference on Terahertz Electronics*, Vol. 2, pp. 447-448, Sept. 2005.

[3.26] P. H. Siegel, R. P. Smith, M. C. Gaidis, S. C. Martin, "2.5-THz GaAs Monolithic Membrane-diode Mixer", *IEEE Transactions on Microwave Theory and Techniques*, Vol. 47, NO. 5, May 1999.

[3.27] M. McColl, D. T. Hodges, W. A. Garder, "Submillimeter-Wave Detection with Submicron Size Schottky-Barrier Diodes", *IEEE Transactions on Microwave Theory and Techniques*, Vol. 25, Issue 6, Jun. 1977.

[3.28] R. J. Bauer, M. Cohn, J.M. Cotton, R.F. Packard Jr., " Millimeter wave semiconductor diode detectors, mixers and frequency multipliers", *Prodeedings of the IEEE,* Vol. 54, Issue 4, pp. 595-605, Apr. 1966.

[3.29] M. Cohn, F. L. Wentworth, and J. C. Wiltse, "High-sensitivity 100-to 300-Gc radiometers,", *Proc. IEEE,* vol. 51, pp. 1227-1232, Sept. 1963.

[3.30] http://www.farran.com

[3.31] A. R. Kerr, "Low noise Room-Temperature and Cryogenic Mixers for 80-120GHz", *IEEE Transactions on Microwave Theory and Techniques*, Vol. 23, Issue 10, Oct. 1975.

[3.32] E. R. Carlson, M. V. Schneider, T. F. Master, " Subharmonically Pumped Millimeter-wave mixers", *IEEE Transactions on Microwave Theory and Techniques*, Vol. 26, Issue 10, Oct. 1978.

[3.33] D. G. Garfield, R. J. Mattauch, S. Weinreb, " RF performance of a novel planar millimeter-wave diode incorporating an etched surface channel", *IEEE Transactions on Microwave Theory and Techniques*, Vol. 39, Issue 1, Jan. 1991.

[3.34] P. H. Siegel, R. J. Dengler, I. Mehdi, J. E. Oswald, W. L. Bishop, T. W. Crowe, and R. J Mattauch, " Measurement on a 215-GHz Subharmonically pumped waveguide mixer using planar Back-to-Back Air-Bridge Schottky diodes", *IEEE Transactions on Microwave Theory and Techniques*, Vol. 41, No. 11, Nov. 1993.

[3.35] I. Mehdi, T. H. Lee, D. A. Humphrey, S. C. Martin, R. J. Dengler, J. E. Oswald, A. Pease, R. P. Smith and P. H. Siegel, " 600GHz Planar-Schottky –Diode Subharmonically Waveguide Mixers", *Microwave Symposium Digest, 1996 IEEE MTT-S*, Volume 1, pp. 377-380, June 1996.

Chapter 4

Diode and Mixer Modelling

The first section of this chapter presents the modelling of the Schottky diode by two different methods. The diode impedance is evaluated to choose the best fabrication parameters for building a mixer at 200 GHz with low noise and low conversion loss. The second section presents the modelling of the first generation of integrated Schottky diodes. The final part presents the modelling of a 183 GHz integrated GaAs mixer developed in collaboration with RAL, LERMA Observatory of Paris and LISIF University of Paris 6.

4.1 Planar Schottky diode Modelling

This section describes two different methods to evaluate the impedance of the Schottky diode seen between the anode and the ohmic contact. The first method defines and evaluates the impedance of the diode through lumped elements. The impedance is then used in a modified version of the original mixer program written by P. H. Siegel and A. R. Kerr in 1978 [4.1]. The program computes the conversion loss and noise temperature of a mixer, given the diode characteristics and embedding circuit impedances. The second method employs a combination of HFSS and ADS to extract the diode impedance and evaluate the parasitic capacitance as a function of fabrication parameters.

4.1.1 Definition and calculation of diode impedance

The whisker-contacted and planar mixer diode structures are shown respectively in Fig. 4.1 and Fig 4.2. The whisker diode configuration was a typical configuration used around 1980 as described in chapter 3. For this reason the mixer program written by P.H Siegel and A. R. Kerr used this configuration in order to estimate diode impedance and mixer performance. The program was modified to use the planar diode configuration used in this research. Fig. 4.2 shows the gold contact pad and finger (which contacts the anode), the ohmic contact, insulating layer of silicon dioxide, the lightly doped active n layer, the higher doped n^+ layer and a semi-insulating substrate. Also shown is an etched air-bridge that isolates the device during fabrication and reduces the parasitic capacitance.

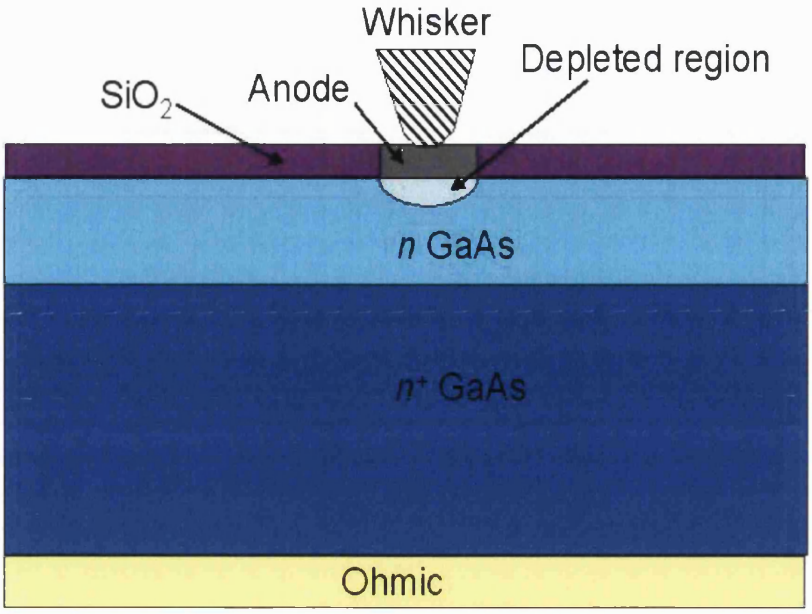

Fig. 4.1 Whisker diode cross section

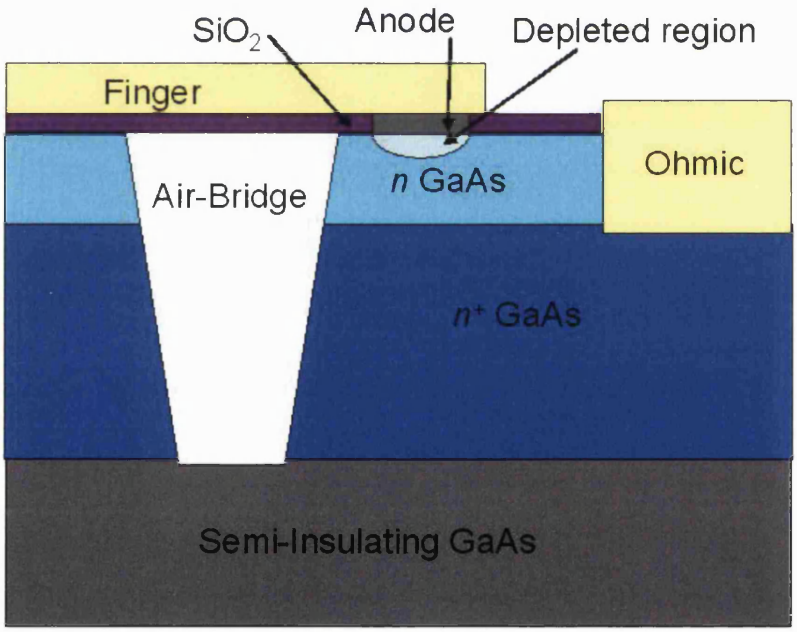

Fig. 4.2 Planar Schottky diode cross section

A circuit model for the Schottky diode is shown in Fig. 4.3. It illustrates the behaviour of the depletion region under the anode. The depletion region is equivalent to a nonlinear resistance R_j in parallel with a nonlinear capacitance C_j. As presented in Chapter 2, the Schottky diode is largely immune to minority carrier effects and for this reason the capacitance and current change almost instantaneously with junction voltage. In Fig. 4.3 R_1, L_u and C_u are respectively the resistance, inductance and capacitance of the undepleted epilayer.

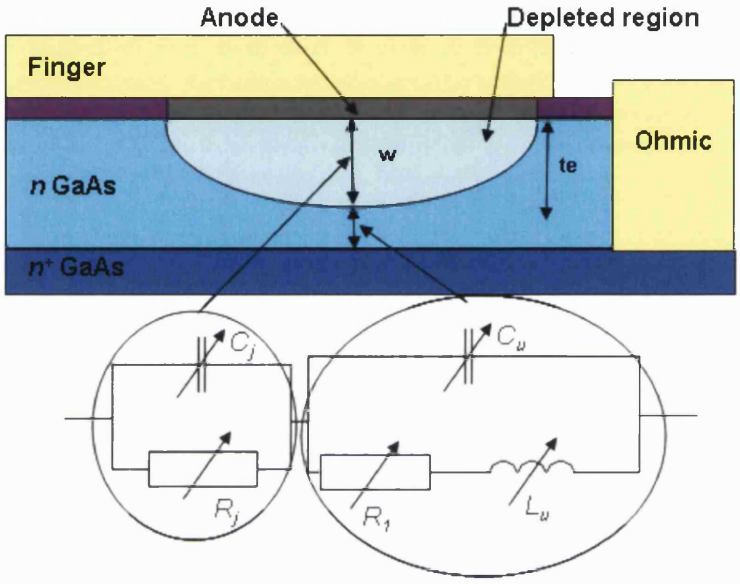

Fig. 4.3 Extended model of Schottky diode

The impedance of the undepleted epilayer R_1 Fig. 4.3, is given by [4.2]

$$R_1 = \frac{t_e - w}{A_0 q \mu_{e0} N_D} = \frac{(t_e - w)\rho_e}{A_0} \tag{4.1}$$

where t_e is the thickness of the epilayer, w is the width of the depletion region, A_0 is the area of the anode, μ_{e0} is the mobility of the electrons in the epilayer, N_D is the doping concentration in the epilayer and ρ_e is the resistivity in the epilayer.

Carriers in the undepleted region also display inertia effects due to nonzero effective mass which is modelled as inductance. Upon arrival at the potential barrier, electrons travelling through the epilayer either pass over or are reflected similar to a scattering event. The transit time of electrons through this layer results in a

scattering frequency $w_{s,eff}$. The inductance through the undepleted epilayer is given by [4.21] as

$$L_u = \frac{R_1}{\omega_{s,eff}} \tag{4.2}$$

where

$$\omega_{s,eff} = \frac{q}{m^* \mu_{e0}} + \frac{v_d}{t_e} \tag{4.3}$$

and v_d is the mean drift velocity of the electrons. A displacement current also accounts for a capacitance that shunts the series undepleted epilayer resistance and inductance and is given by

$$C_u = \frac{\varepsilon_s A_0}{(t_e - w)}. \tag{4.4}$$

At frequencies below 1 THz most models omit the displacement capacitance. For lower frequencies the reactance from C_u is much larger than the resistance from R_1 and therefore most of the current flows through the resistor. The equivalent circuit model presented in fig 4.4 is commonly use for frequencies below 1 THz.

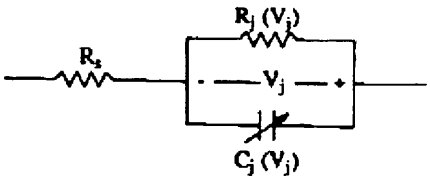

Fig. 4.4 Schottky diode equivalent circuit [4.20]

In Fig. 4.4 the series resistance R_s can be broken down into four main components as shown in Fig. 4.5 This follows the early analyses of spreading resistance in a semiconductor by L. E. Dickens [4.3] and more recently by J. A. Calviello [4.3] and K. Mckinney et al [4.5].

The first component, R_1, arises from current flow in the undepleted epitaxial layer equation (4.1). R_2, is called the spreading resistance and is of dominant importance in diodes used for high frequency mixing applications.

The spreading resistance R_2 is caused by high frequency signals being restricted to current flow in only the surface area of the semiconductor. The depth at which a high frequency signal penetrates a material is called the *skin depth* and is inversely proportional to frequency [4.3]

$$\delta = \sqrt{\frac{2}{\omega\mu\sigma}} \tag{4.5}$$

where ω is the angular frequency, μ is the mobility of electrons in the material and σ is the conductivity of the material.

R_2 can be decomposed into two components [4.3] R_2' and R_2''. R_2' arises from the current flowing vertically (4.6) and R_2'' from the current flowing toward the ohmic contact.

$$R'_2 = \frac{\rho_{n+}}{2\pi R_0}\tan^{-1}\left(\frac{\delta}{R_0}\right) \tag{4.6}$$

$$R''_2 = \frac{SF\rho_{n+}}{4\pi\delta} \tag{4.7}$$

$$R_2 = R'_2 + R''_2 = \frac{\rho_{n+}}{2\pi R_0}\tan^{-1}\left(\frac{\delta}{R_0}\right) + \frac{SF\rho_{n+}}{4\pi\delta} \tag{4.8}$$

where ρ_{n+} is the resistivity of the n^+ layer, R_0 is the anode radius and SF is a scaling factor to account for the current not taking a full radial pattern. The scaling factor, SF, is given by [4.6]

$$SF = \frac{360°}{2\phi + 180} \tag{4.9}$$

where ϕ is indicated in Fig. 4.6.

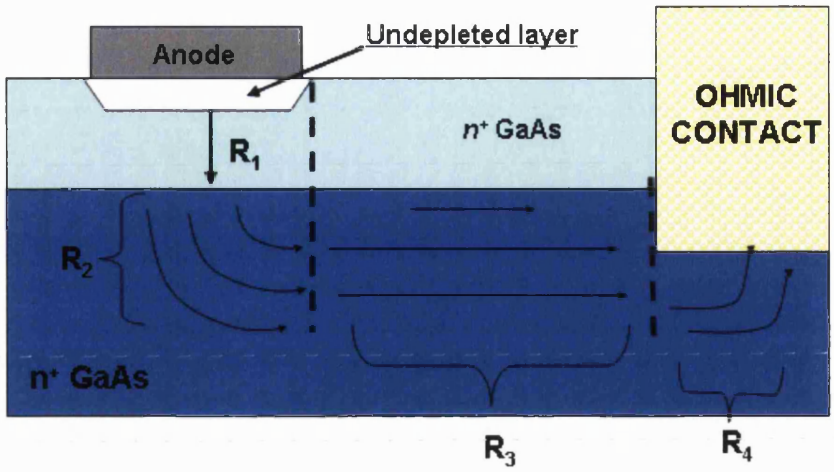

Fig. 4.5 The breakdown of series resistance through the n+ layer. R_2 is attributed to spreading resistance, R_3 is resistance to current flowing on the device surface and R_4 is resistance to current entering the ohmic contact.

R_3 accounts for the resistance encountered by current flow across the device surface and, with the addition of *SF*, is given by Setzer as [4.7]

$$R_3 = \frac{\rho_{n+} SF}{2\pi\delta} \ln\left(\frac{r_x}{R_0}\right) \tag{4.10}$$

where r_x is the distance between the centre of the anode and the edge of the cathode. The final component is the resistance to current flowing into the ohmic, given by Setzer as [4.7]

$$R_4 = \frac{1}{SF\pi r_e}\left(\frac{\rho_n + r_c}{\delta}\right)^{1/2} \tag{4.11}$$

where r_e is the distance from the centre of the anode to the edge of the chip, ρ_n is the resistivity of the *n* layer and r_c is the specific contact resistance of the ohmic contact.

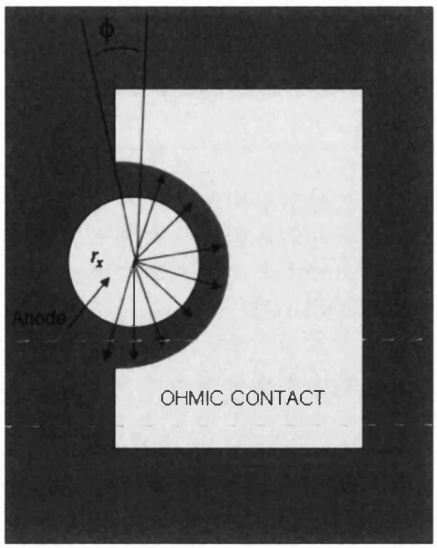

Fig. 4.6 Scaling factor used in calculating the spreading resistance.

The shunt capacitance of the planar device is also different from the whisker diode. The planar configuration as indicated in Fig. 4.7 has more capacitance parameters than the whisker diode and several efforts in the design have been made to reduce this extra shunt capacitance. This shunt capacitance is very detrimental since it is connected within the series resistance. One design that has successfully reduced this shunt capacitance is the "air bridge diode" developed by the University of Virginia in 1987 [4.8] and used in our design. This design effectively cuts off the current path from the capacitance to the anode. The remaining shunt capacitance is primarily due to the relatively small fringing field component C_{pp}, in series with C_p. C_{pp} can be minimized by reducing pad area, increasing pad separation, providing a material with a lower dielectric constant under and between the pads or by reducing the thickness of the dielectric. Most of these extra capacitances were modelled during the structure simulation discussed in the next section.

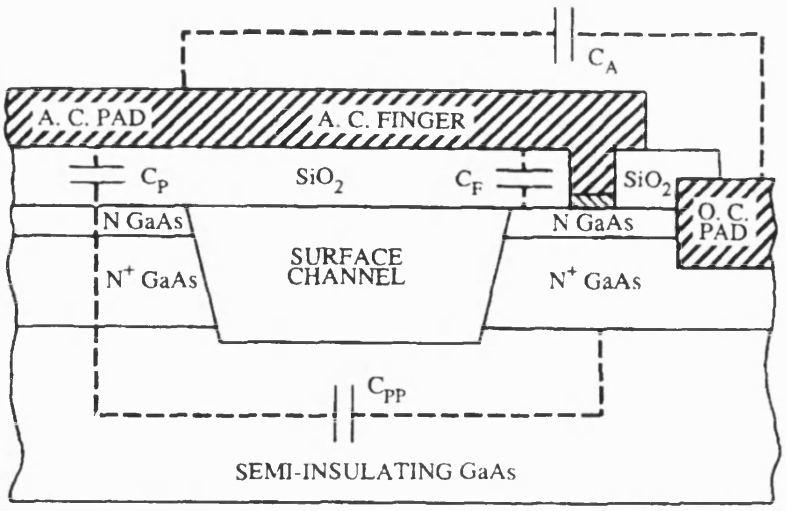

Fig. 4.7 Extra shunt capacitances: C_P is a parallel plate capacitance from the anode contact pad, C_F is a parallel plate capacitance due to the contact finger [4.8].

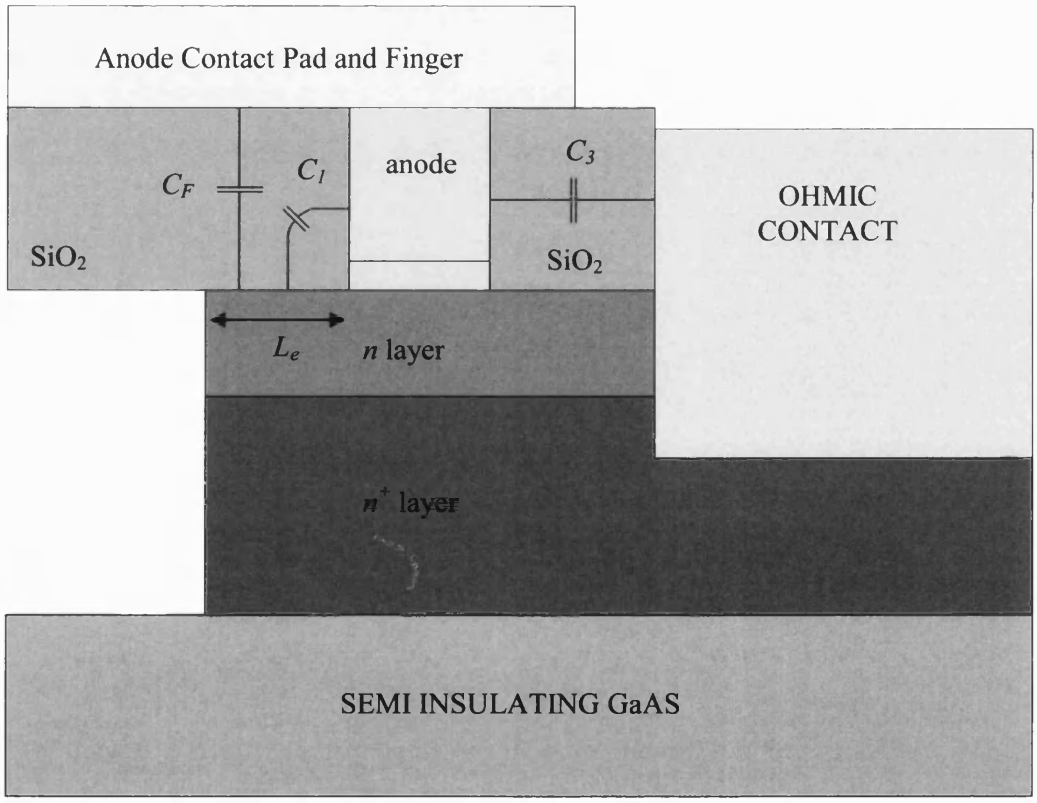

Fig. 4.8 Parasitic capacitances within the planar diode. C_1 is the capacitance due to the anode cone and the material beneath it, C_F the capacitance given between the GaAs and anode contact finger and C_3 is the capacitance between anode and ohmic contact.

C_1 has been evaluated by Kerr [4.9] and is given by

$$C_1 = \frac{\pi\varepsilon\left(a_0^2 - b_0^2\right)^{1/2}}{\tan^{-1}\left[\dfrac{\left(a_0^2 - b_0^2\right)^{1/2}\tan\left(\dfrac{\phi_a}{2}\right)}{\left(a_0 + b_0\right)}\right]} \tag{4.12}$$

where

$$\begin{aligned} a_0 &= r_0 \ln\left(\frac{r_2 - r_0}{r_1 - r_0}\right) \\ b_0 &= r_2 - r_1 \end{aligned} \tag{4.13}$$

and all radii are shown in Fig. 4.9.

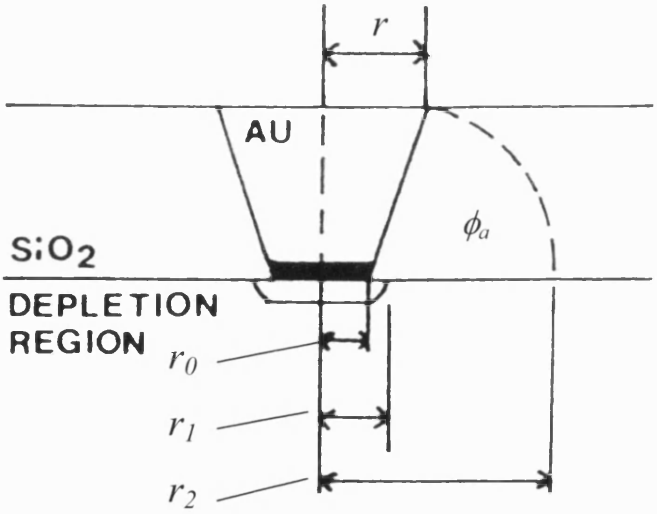

Fig. 4.9 The radii and angle needed for calculating C_1, [4.6]

C_F is the capacitance between the *n* GaAs and contact finger and is given by [4.6]

$$C_F = 2.5\varepsilon L_e \tag{4.14}$$

where L_e is the portion of the finger that overhangs the active GaAs as shown in Fig. 4.8. The capacitance between the anode and the ohmic contact, C_3, is given by [4.10]

$$C_3 = \frac{2\pi\varepsilon t_{ox}}{\ln\left(r_x / r\right)} \tag{4.15}$$

where t_{ox} is the thickness of the oxide layer. The total shunt capacitance is the sum of C_1, C_F and C_3.

4.1.2 Mixer performance as a function of diode parameters

The diode cut-off frequency is often defined as

$$f_c = \frac{1}{2\pi R_s C_j} \tag{4.16}$$

This is simply the frequency where the series resistance is equal to the junction reactance at zero bias ($R_s = \frac{1}{\omega_c C_j}$) [4.11]. Its main benefits are that it is easily measured and the diodes with the greatest f_c virtually always yield the best performance at THz frequencies.

Using the set of equations for the series resistance and capacitance described in the previous section a trend can be found to determine the diode parameters. Fig. 4.10, 4.11 and 4.12 present the diode cut-of frequency function of the epitaxial doping concentration N_D, anode radius R_0 and epitaxial thickness t_e.

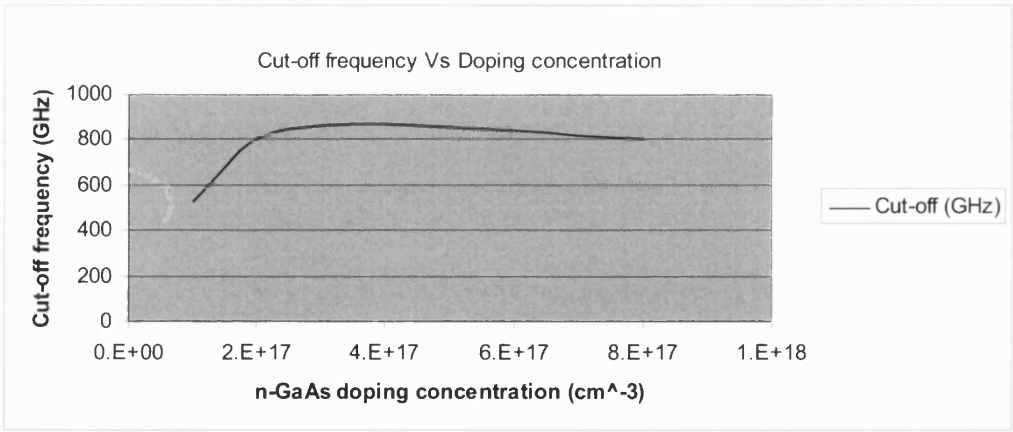

Fig. 4.10 Cut-off frequency function of *n*-GaAs doping concentration N_D.

Fig 4.10 demonstrates that increasing the doping concentration of the *n*-GaAs increases the cut-off frequency. However too much doping will increase the junction capacitance and degrade the diode ideality factor.

Fig 4.11 demonstrates that increasing the anode diameter decreases the cut-off frequency by reducing the junction capacitance. For this reason high frequency mixer diodes requires small anode size. However small diameter anodes increase the series resistance, therefore requiring high doping concentration for the *n-GaAs* layer.

Fig 4.12 demonstrates that increasing the epitaxial thickness t_e decreases the cut-off frequency. Increasing the thickness t_e increases the junction capacitance therefore decreases the cut-off frequency.

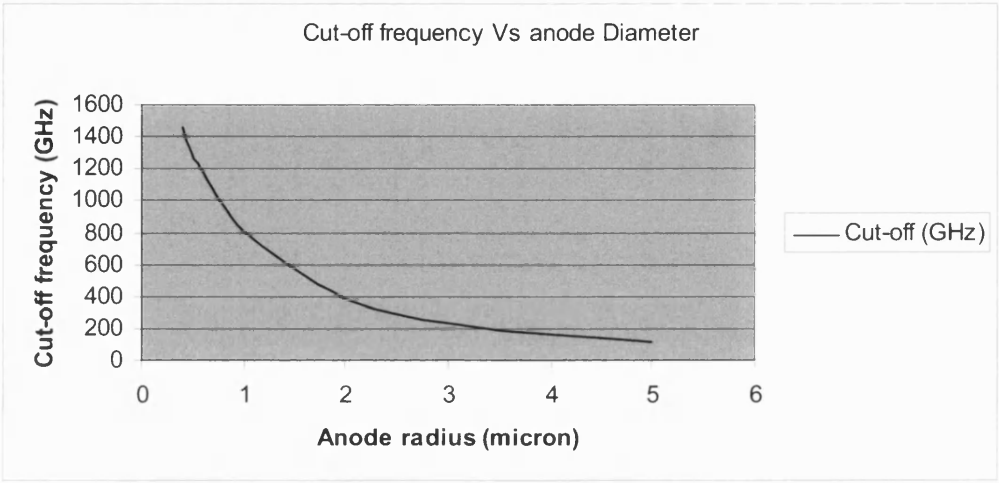

Fig. 4.11 Cut-off frequency as a function of anode radius R_0.

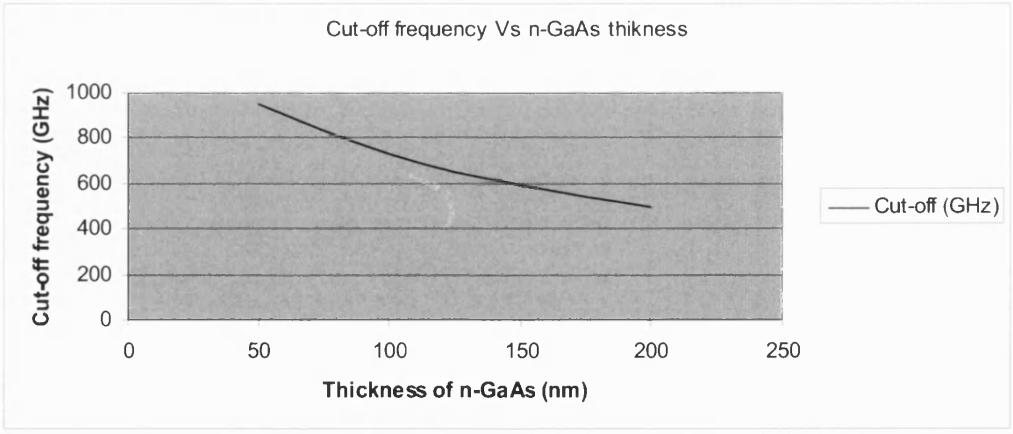

Fig. 4.12 Cut-off frequency as a function of epitaxial thickness t_e.

In the view of these plots, for high frequency applications the Schottky diode should have a doping concentration around 4.10^{17} cm-3, an anode diameter of 1 µm and epi-layer thickness of 50 nm.

To determine the performance of a diode with such parameters in a mixer circuit, a modified version of the mixer program written by P.H Siegel and A. R. Kerr was used [4.1]. The program computes the conversion loss and noise temperature of a mixer, given the diode characteristics and embedding circuit impedances. The program first performs a nonlinear circuit analysis to determine the diode conductance and capacitance waveforms produced by a local oscillator. A small-signal linear analysis is then used to find the input and output impedances and the conversion loss between the mixer ports. Finally, the thermal and shot noise contributions from the diode are determined.

The most difficult step in analysing a mixer is finding the diode conductance and capacitance waveforms produced by the LO. The technique used by Siegel and Kerr in this program is based on solving the nonlinear problem by considering a series of reflections between the diode and the embedding network. The algorithm operates in the time domain when considering the diode and in the frequency domain when dealing with the embedding network. The small signal properties of the mixer are derived from knowledge of the diode conductance and capacitance waveforms and the impedance of the embedding network.

The mixer analysis program allows arbitrary embedding impedances at the harmonics of the local oscillator and the side-band frequencies. In order to run the program the user must supply the embedding impedance seen by the diode at each harmonic of the LO and at the harmonic sidebands, the characteristics of the diode, including the CV dependence, and the operating conditions of the mixer, i.e., the bias voltage applied to the diode, LO and intermediate frequencies.

The output of the program includes the large signal current, voltage, conductance, and capacitance waveforms at the diode, the Fourier coefficients of the diode conductance and capacitance, the conversion loss between each pair of sideband frequencies, the IF output impedance, the input impedance at each sideband, and the equivalent single-sideband, and the equivalent single input noise temperature.

The original program was designed to use whisker contact diodes. This configuration is quite different to the planar Schottky diode. Fig. 4.1 illustrates the configuration, resistance and capacitance parameters used in the original program. Fig. 4.2 shows the new configuration and new set of resistances and capacitances parameters, which have been examined in the previous section.

Using the modified program, the conversion loss of a diode is computed. The diode dimensions and design are presented in Fig. 4.13. The structure has an epi-layer doping concentration of 4.10^{17} cm^{-3} and a thickness of 50 nm. From the dimensions of the design in Fig. 4.13, the parasitic capacitances and series resistances were calculated in a Fortran script added to the mixer program and then used to compute the conversion loss and noise temperature of this diode structure. Fig. 4.14 presents the conversion loss as a function of anode diameter for this particular structure.

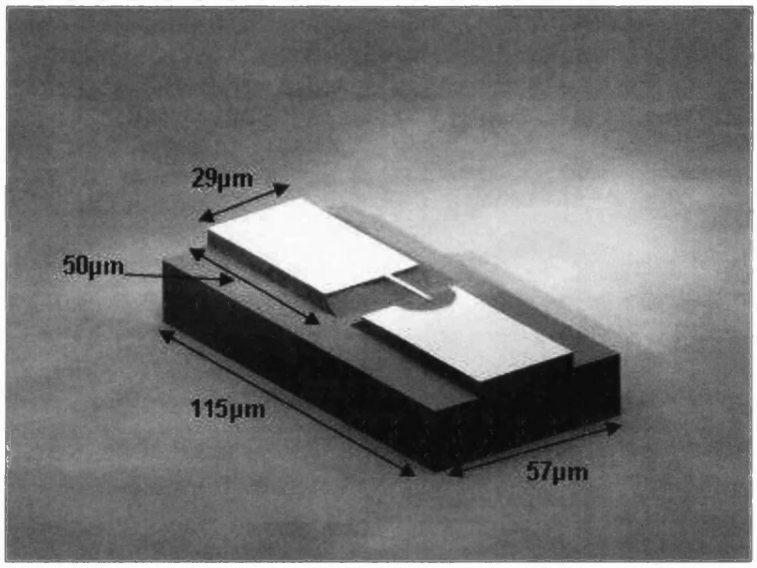

Fig. 4.13 CAD image of air-bridge Schottky diode.

Fig. 4.14 shows that the double side band conversion loss reached a minimum at 3.5 dB for a diode with a radius of 0.7 µm. For this radius the anode impedance matched the structure embedding impedance resulting in a minimum conversion loss.

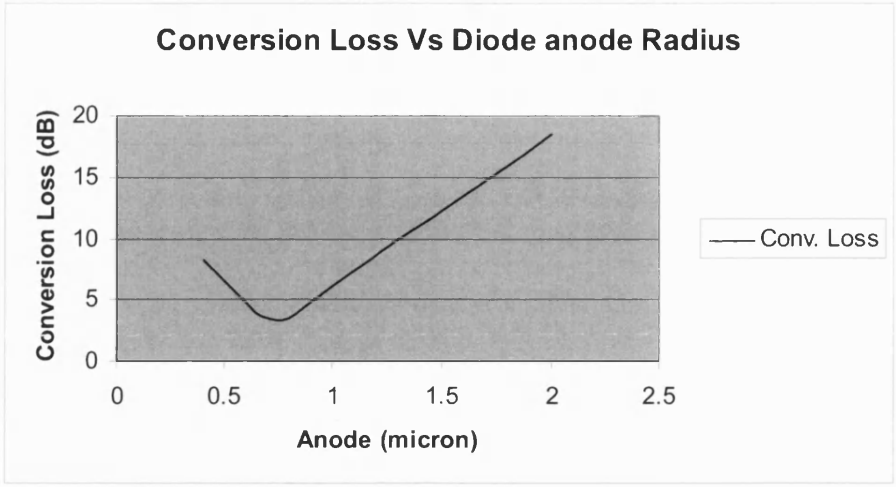

Fig. 4.14 Double Side Band Conversion Loss function of anode radius.

Using the P.H Siegel and A. R. Kerr Fortran mixer program it was not practical to change the diode structure without having to manually input a lot of diode parameters making it difficult to change the diode design. Furthermore calculating the parasitic capacitance of structures with really low capacitance was found challenging and inaccurate with the equivalent circuit model. A more integrated approach was employed using HFSS and ADS to compute the diode impedance and conversion loss.

4.1.3 3D Electromagnetic simulation of air-bridged diode

The equivalent circuit model presented in the previous section gives a good idea of the major components of the series resistance as well as the parasitic capacitance. However the parasitic components close to the diode as well as the finger have predominant impact since the EM fields are the strongest around the anode.

Using HFSS 3D EM simulation the goal was to predict, compute and compare the measurements to the parasitic capacitance of the diode fabricated during this research. Several authors have presented a similar approach [4.12]. The method presented here, to extract the diode capacitance, was presented by A. Maestrini and B. Thomas [4.13].

The method differs from previous work as it models the finger and the finger transition to the pads more accurately.

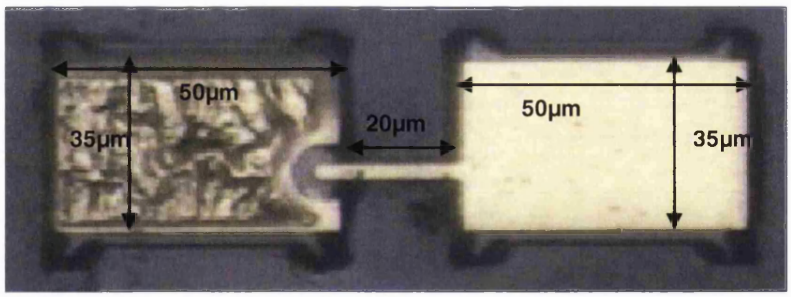

Fig. 4.15 Picture of Schottky diode fabricated during this research.

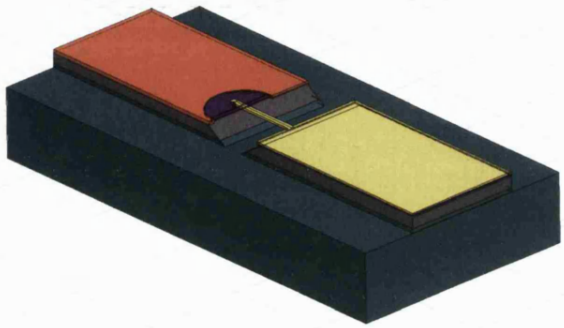

Fig. 4.16 HFSS 3D Model of Schottky diode

The 3D model used in HFSS to simulate the diode is presented in fig. 4.16. The design was created to accurately reproduce the geometry of the diode fabricated during this research (Fig. 4.15).

In this 3D model 3 ports are defined, the anode port, the ohmic-pad port (cathode) and the anode-pad port. The pad ports are defined as suspended micro-strip in a wave-guide (Fig. 4.17). The channel dimensions are set to permit only one mode (quasi-TEM) to propagate at 200 GHz. Both ports are deembedded, the cathode is deembedded to where the finger starts and the cathode to where the silicon dioxide starts (Fig. 4.17).

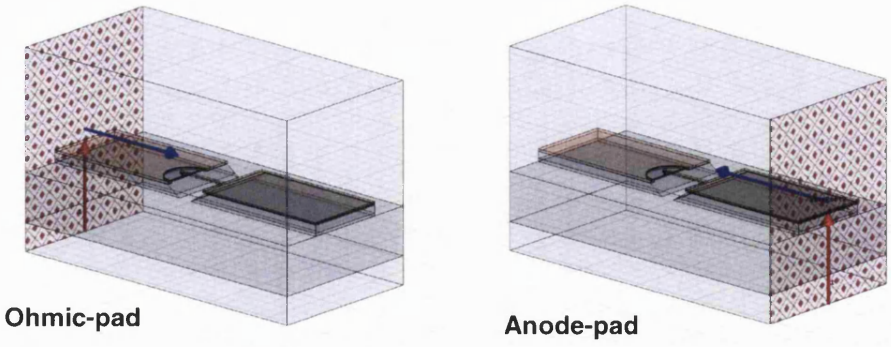

Fig. 4.17 Definition of anode-pad and Ohmic-pad ports

The definition of the anode port is critical to correctly evaluate the parasitic capacitance of the diode. J. Hesler [4.12] proposed a method were a coaxial probe is use as the anode port. The coaxial probe has an outer conductor connected to the cathode and a inner conductor connected to the anode. The gap between the two conductors is set to equal the n-GaAs layer thickness J. Hesler [4.12] and A. Maestrini [4.13]. A. Maestrini concluded from varying the gap between the inner conductor and outer conductor of the coaxial probe that too wide a gap could result in under-estimating the capacitance. Fig. 4.18 presents the anode port defined as a coaxial probe.

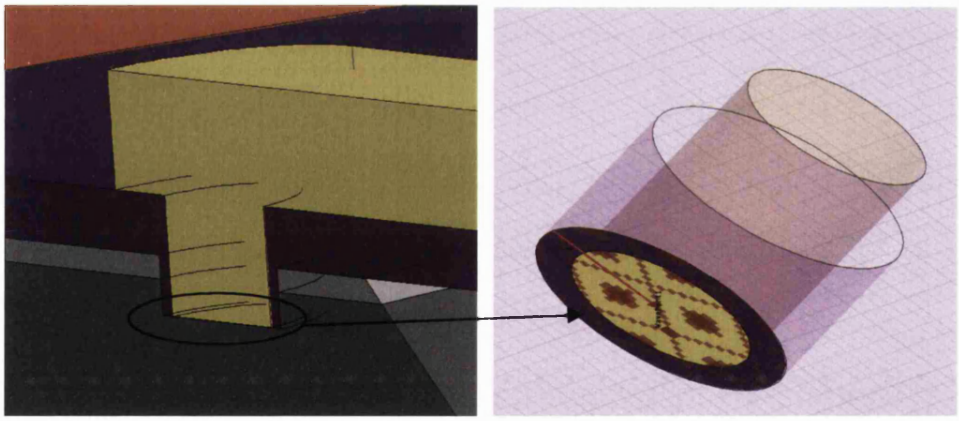

Fig. 4.18 Definition of anode port

The HFSS 3D diode model is simulated between 90 GHz and 200 GHz which represents the operating band of the diode. The S-parameters are then extracted and fed into the left side of the ADS circuit Fig. 4.19.

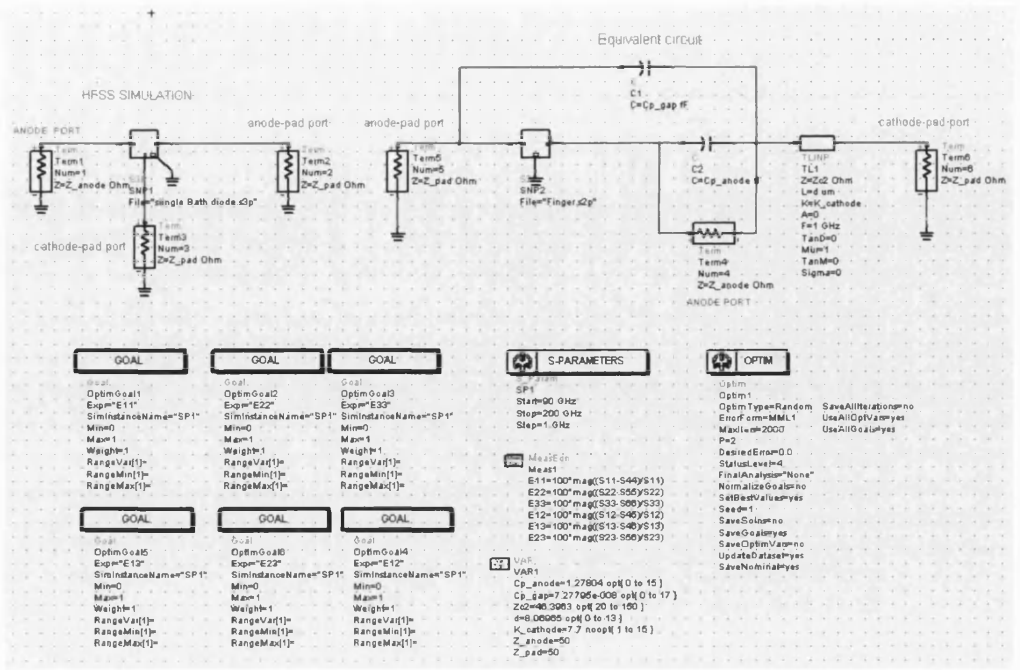

Fig. 4.19 Simulation of the full 3D structure of the diode (left).
Equivalent diode model (right).

The ADS circuit compares and optimizes the equivalent circuit (right side) to match the S-parameters of the full 3D simulation (left side) by adapting the capacitance C_p and C_J. Where C_p represents the gap capacitance and C_J the diode capacitance, those parameters being the predominant source of capacitance in the structure.

The series resistance and junction capacitance are calculated with classical formulas present in the ADS software suite during the mixer analysis.

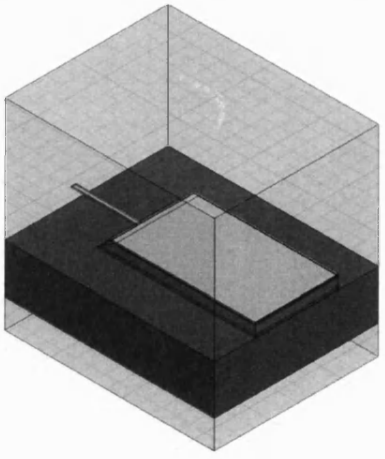

Fig. 4.20 3D model of finger and transition

The ADS equivalent circuit (right side) includes from left to right the anode-pad port, the S-parameters from the finger transition (Fig. 4.20), the anode capacitance to be tuned C_1, in parallel with the anode port. The gap capacitance C_p, is in parallel to all the previous the circuit followed by a section of transmission line representing the length from the anode to the ohmic contact, and finally the ohmic-pad port.

The left and right S_{11}, S_{22}, S_{33}, S_{12}, S_{13} and S_{23} are compared and the capacitances C_1 and C_p are optimized to match the port S_{44} to S_{11}, S_{22} to S_{55}, S_{33} to S_{66}, S_{12} to S_{45}, S_{13} to S_{46} and S_{23} to S_{56}.

From I. Mehdi [4.14], the total parasitic capacitance is:

$$C_{parasitic} = C_1 + C_p \tag{4.17}$$

B. Thomas [4.15] has shown that the position of the substrate in the channel in which it is located affects the value of $C_{parasitic}$. During our simulations, the same results were found with our diode design and an air-gap of 70 μm was taken to reproduce the air-gap in the RAL mixer (Table 4.1).

Air Gap (μm)	C_p (fF)	C_1 (fF)	$C_{parasitic}$ (fF)
70 um	2.23	1.3	3.53
50um	2.61	1.8	4.41
40um	3.36	1.7	5.06
2um	3.1	1.4	4.5

Table 4.1 Parasitic capacitance as a function of air gap.
This simulation was done with a 1.5 μm anode diameter.

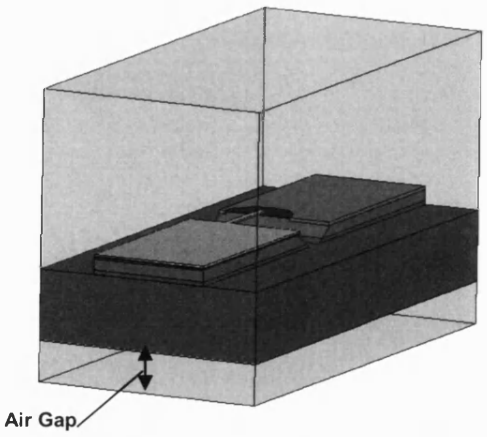

Fig. 4.21 Air gap parameter used in the diode parasitic capacitance simulation.

We calculated the total capacitance of the diode depending on the anode diameter for two different lengths of air bridge: 15 μm or 20 μm. These simulations are compared to fabricated devices in Fig. 4.22.

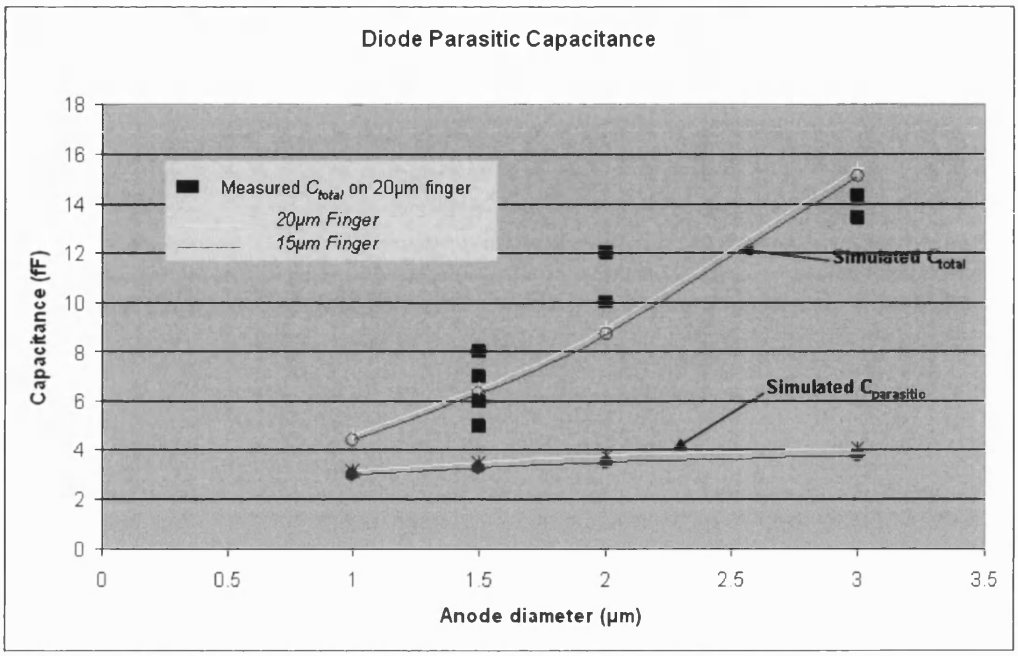

Fig. 4.22 Parasitic capacitance for 15 μm or 20 μm finger as a function of anode size.

Fig. 4.22 shows that good agreement exists between simulation and measured capacitance. The simulated $C_{parasitic}$ represents the simulation of the capacitance as a function of anode size. The simulated C_{total} represents the $C_{parasitic}$+ C_{j0}. Chapter 6 will present, in more detail, measurements of different capacitance, series resistance and ideality as functions of anode size.

3D simulation allows good simulation of the diode parasitic capacitance. The same method was used to optimise the diode structure for the membrane and integrated diode cases.

4.2 Simulation of Integrated Membrane Mixer

Following the good mixer performance results using the flip-chip diode (process developed during this research), an integrated mixer design was decided. Integrating the Schottky diode, as mention in Chapters 1 and 3, has two main advantages: better control in the placement of the diode, resulting in a more accurate control of the

embedding impedance seen by the diode, and elimination of the difficult assembly of the diode on the quartz substrate. The first integrated mixer circuit was designed to use an existing mixer block. The mixer is of the split-block type using suspended-substrate stripline and reduced-height waveguide. The mixer block was designed to work with a quartz circuit and a flip-chip diode as the non-linear mixing device. Fig. 4.23 shows the mixer block. Fig. 4.24 presents the old quartz configuration and Fig. 4.25 the new one with the anti-parallel diode integrated with the GaAs RF circuit.

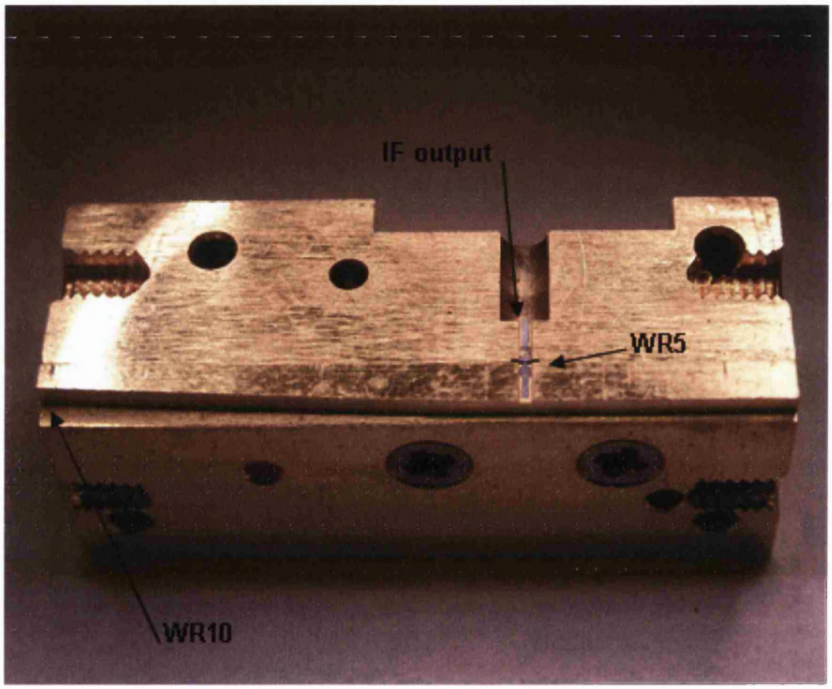

Fig. 4.23 Submillimetre-wave mixer design with flip-chip diode on top of quartz RF circuit.

The mixer block is made from 4 pieces of brass machined with a milling machine. To maximize and tune the mixer performance over different frequency, both RF signal and Local Oscillator waveguides have E-plane tuners (contacting backshorts). The LO and RF waveguide are reduced to quarter height to reduce the waveguide impedance and suppress the parasitic modes. The IF output is passed through an SMA connector whose centre pin is ribbon bonded to the end of the microstrip filter.

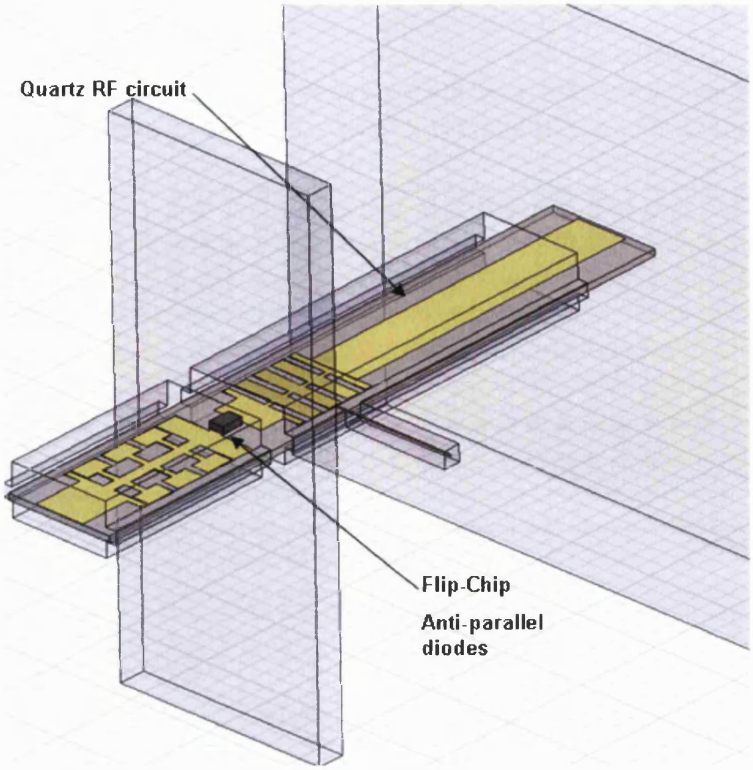

Fig. 4.24 Submillimetre-wave mixer design with flip-chip diode on top of quartz RF circuit.

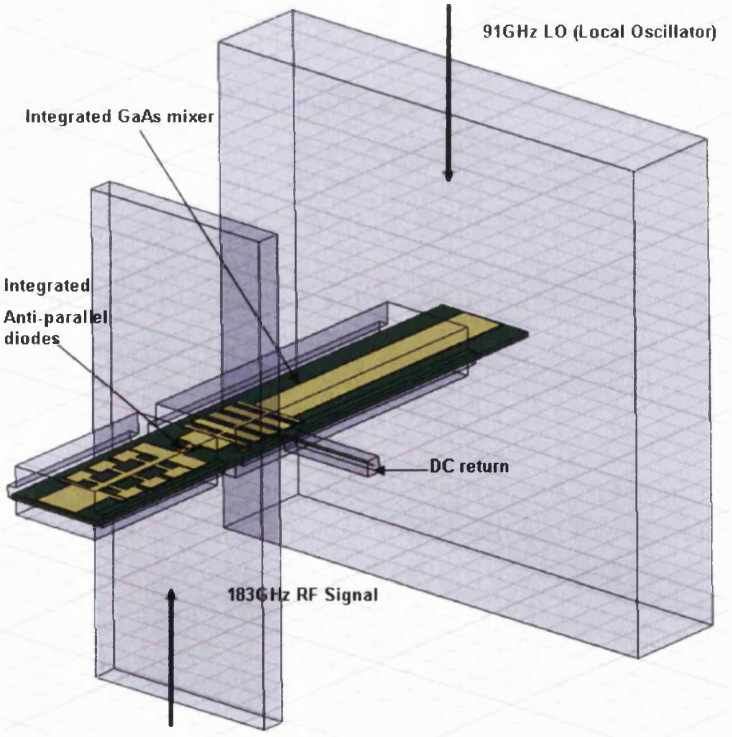

Fig. 4.25 Integrated planar diode submillimetre-wave mixer design.

The quartz RF circuit from the original design was replaced by the integrated GaAs substrate. For this reason the low-pass filter, IF filter and LO antenna had to be redesigned to adapt to the new EM proprieties of the new material.

4.2.1 Optimisation of LO low-pass filter

The LO low-pass filter is designed to allow the LO power to be delivered to the diode while rejecting the RF signals. The design is a classic stepped-impedance low-pass filter on microstrip alternating sections of very high and very low characteristic impedance lines [4.16]. To provide a flat response of LO power as a function of frequency and because the RF frequency was clearly away from the LO frequency a maximally flat response was chosen to design the low-pass filter. The design was optimized using HFSS. The filter design is shown in Fig.4.26 and dimensions are given in Fig. 4.27.

To provide a return to ground for the anti-parallel diode a DC grounding needed to be incorporated. The stub showed in Fig 4.26 is designed to be $\lambda/4$ long at the LO. The stub needed to present a short circuit to the ground at DC but to present an open circuit at the LO. Fig.4.28 presents the S_{21} and S_{23} showing the good return to ground at DC and maximum coupling to the filter at the 90 GHz LO frequency.

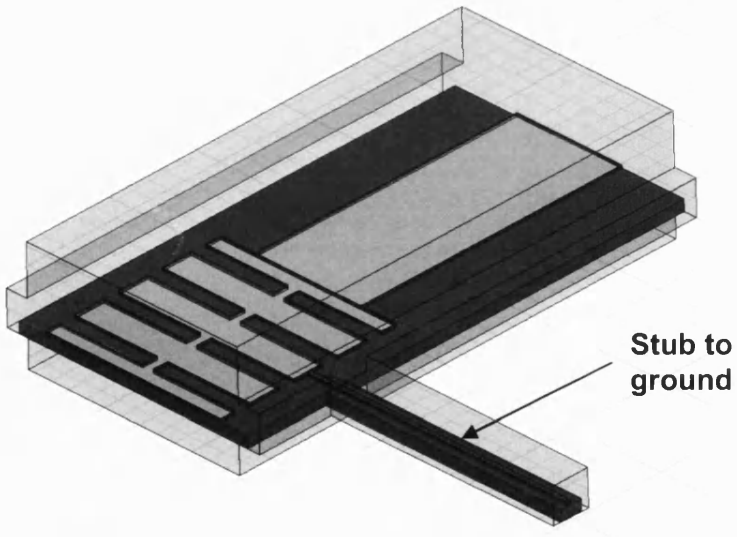

Fig. 4.26 93 GHz Butterworth Low-Pass filter on 50μm GaAs.

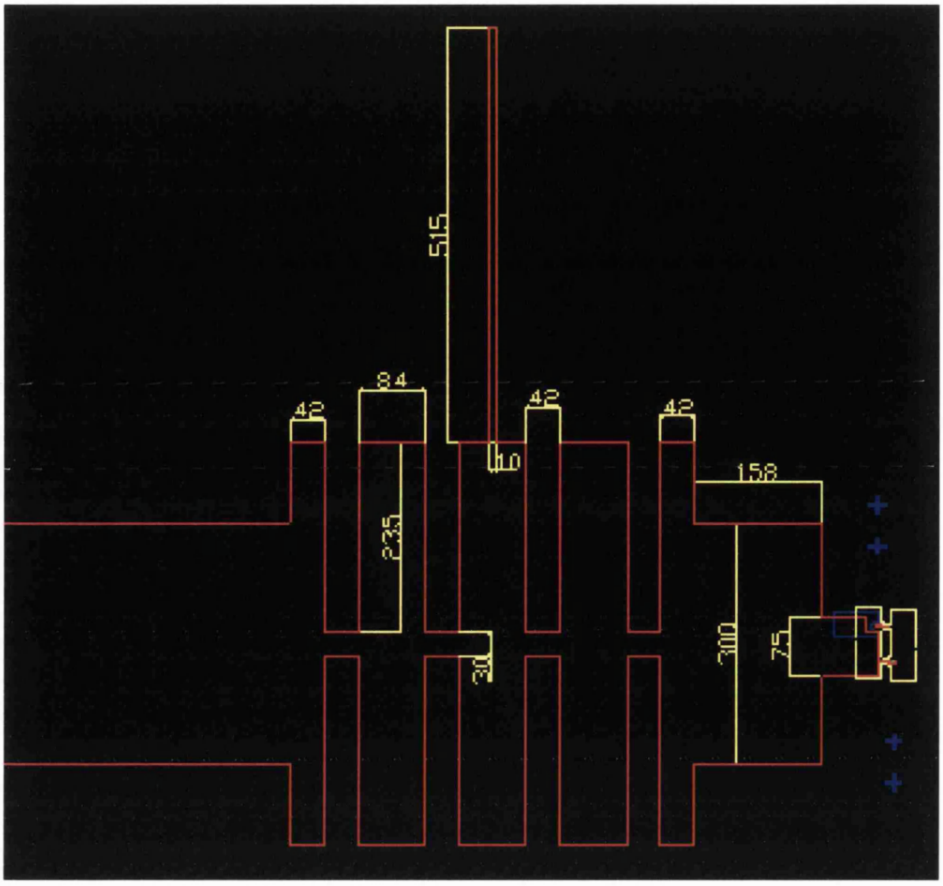

Fig. 4.27 Dimensions in μm of the optimised 93 GHz Butterworth Low-Pass filter.

The frequency response for the filter is shown in Fig. 4.27 and fig. 4.28 giving over 50 dB of rejection across the entire band 170-190 GHz and an insertion loss less than 0.5 dB between 80-93 GHz.

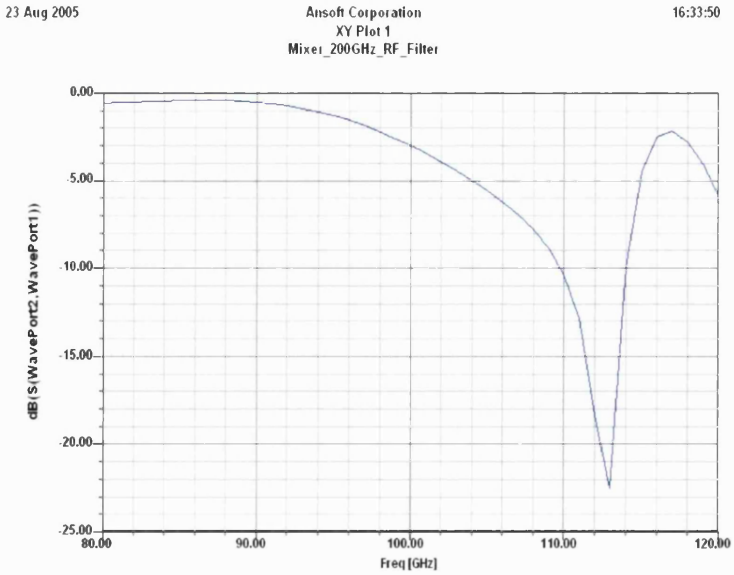

Fig. 4.28 S_{21} response for the Low-Pass filter between 80 GHz and 90 GHz.

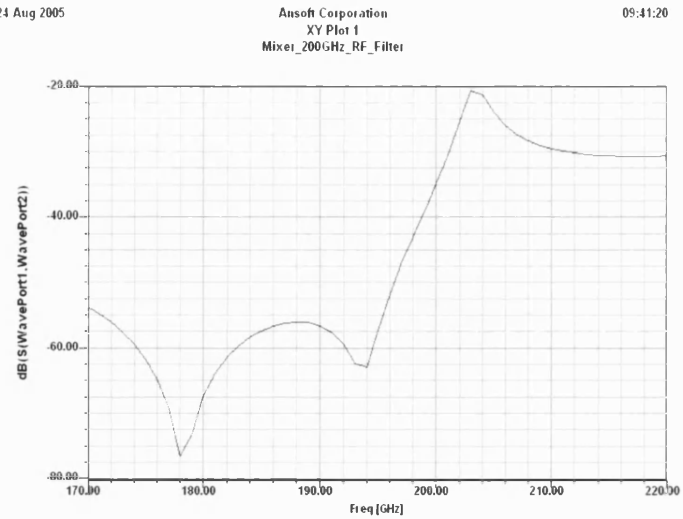

Fig. 4.29 S_{21} response for the Low-Pass filter between 170 GHz and 220 GHz.

4.2.2 Optimisation of LO E-plane probe

Following the optimisation of the low-pass filter, the LO waveguide E-plane probe was optimised using ADS and HFSS to maximise the transition between the waveguide and the microstrip. The LO power is coupled into the microstrip and to the RF low-pass filter and is coupled into the diode. The RF waveguide and IF low-pass filter prevent any leakage of the LO power. The position of the E-plane probe in the LO waveguide-channel was optimised and is presented in Fig. 4.29.

4.2.3 Optimisation of IF low-pass filter

Fig. 4.31 presents the modelled response for an 8-element stripline hammerhead IF filter (shown in Fig. 4.30). A first estimate of the proper dimension was obtained by scaling the filter presented in [4.17]. Then HFSS was used to fine tune the filter dimensions to meet the desired frequency response.

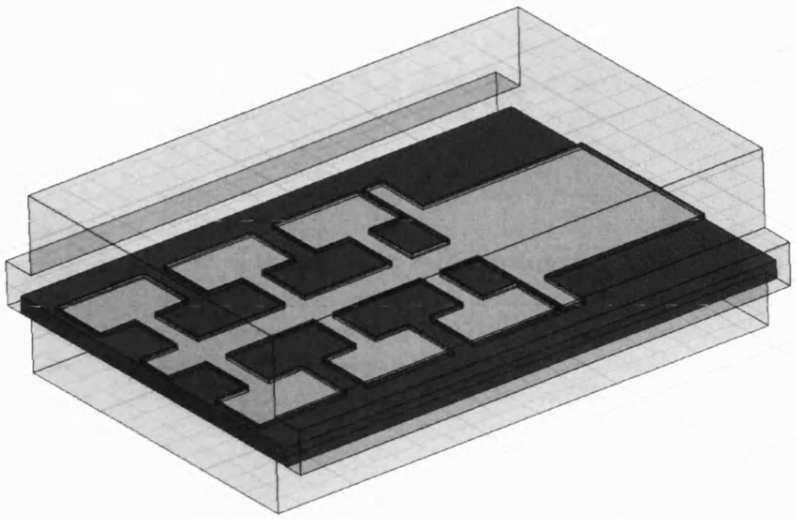

Fig. 4.30 Hammerhead Low-pass filter.

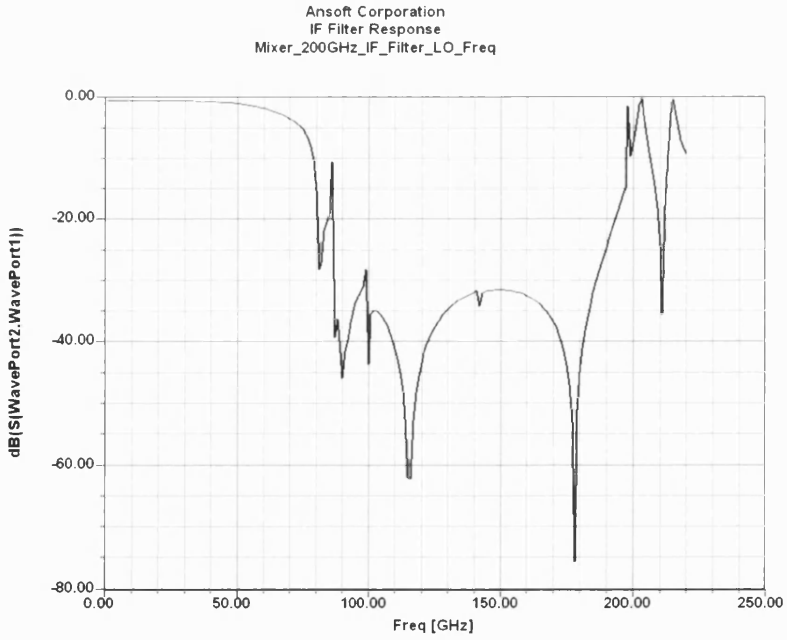

Fig. 4.31 S_{21} response for the low-pass hammerhead filter between 0.5 GHz and 220 GHz.

The frequency response for the hammerhead filter is shown in Fig. 4.31 indicating over 30 dB of rejection across the entire 90-190 GHz band and an insertion loss of less than 0.5 dB between 1 GHz to 5 GHz.

4.2.4 Mixer diodes

The Schottky diodes used in this circuit were fabricated at the University of Bath using the process developed during the fabrication of flip-chip devices, presented in Chapter 5. The diode consists of an anti-parallel Schottky barrier diode pair integrated on GaAs with the RF circuit. The diode design was modified from the flip-chip design presented in Chapter 5. No differential bias was needed for this circuit, so for this reason the anode and cathode pad on each side were shorted together. Fig. 4.32 presents a 3D representation of this design. The diode is located in the RF waveguide. The anode diameters were between 1 μm and 4μm. The measured I-V and C-V characteristics for the 1 μm device yielded a diode series resistance of approximately 18 ohms, ideality factor around 1.24 and a zero bias junction capacitance of 6 fF.

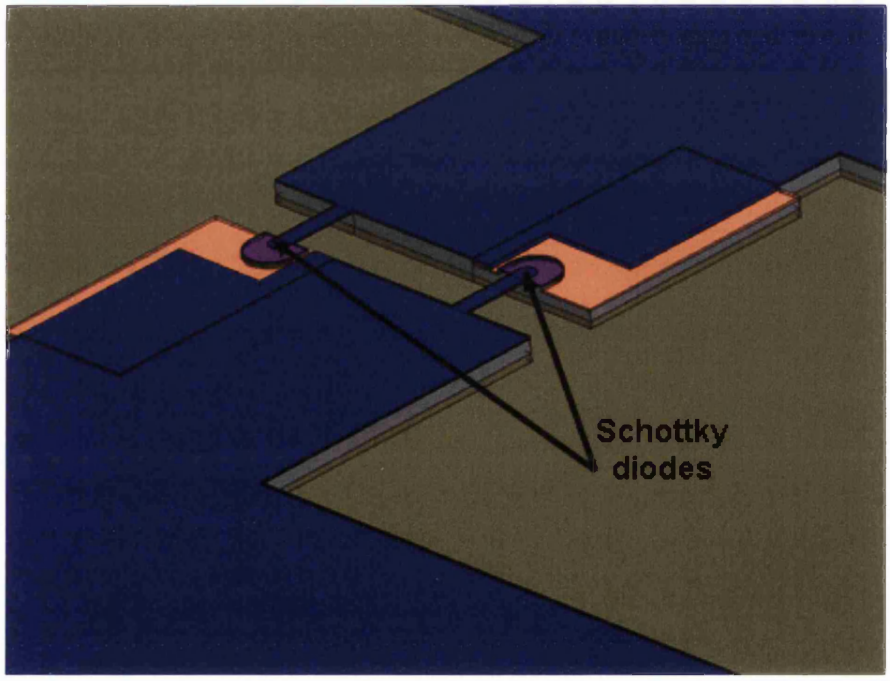

Fig. 4.32 3D representation of integrated Schottky diodes in mixer circuit.

4.2.5 Description of HFSS and ADS circuit model configuration

In order to optimise and assess the performance of the sub-harmonically pumped (SHP) integrated mixer presented in Fig.4.25, a circuit model of the SHP mixer was designed using ADS. The conversion loss and noise temperature of the circuit can be computed using the ADS non-linear analysis.

To accurately model the circuit using ADS, the mixer circuit was divided into parts which were simulated using HFSS at the LO and RF frequency. Fig. 4.33 presents how the circuit was divided for modelling with HFSS.

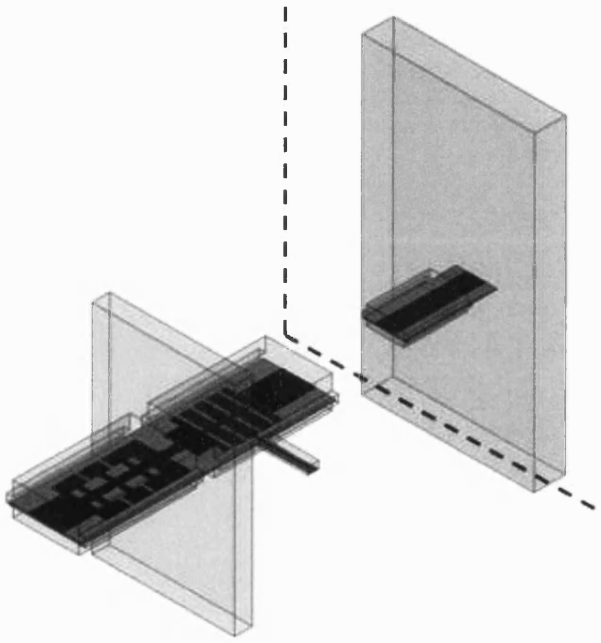

Fig. 4.33 Mixer circuit divided for HFSS simulation.

The HFSS antenna (Fig. 4.34) was modelled as a 3-Port. The S-parameters were calculated for the LO frequency range 80 GHz-120 GHz with the following port definitions:

- Port 1 LO source port
- Port 2 Backshort port
- Port 3 Antenna output

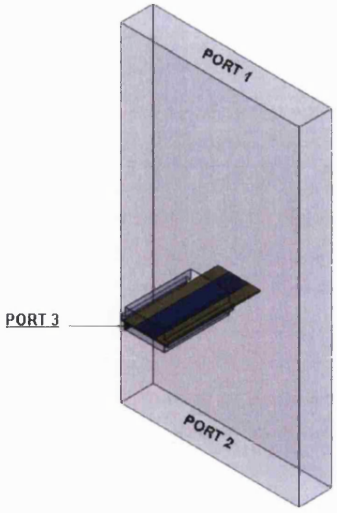

Fig. 4.34 Definition of the LO antenna ports at the LO frequency

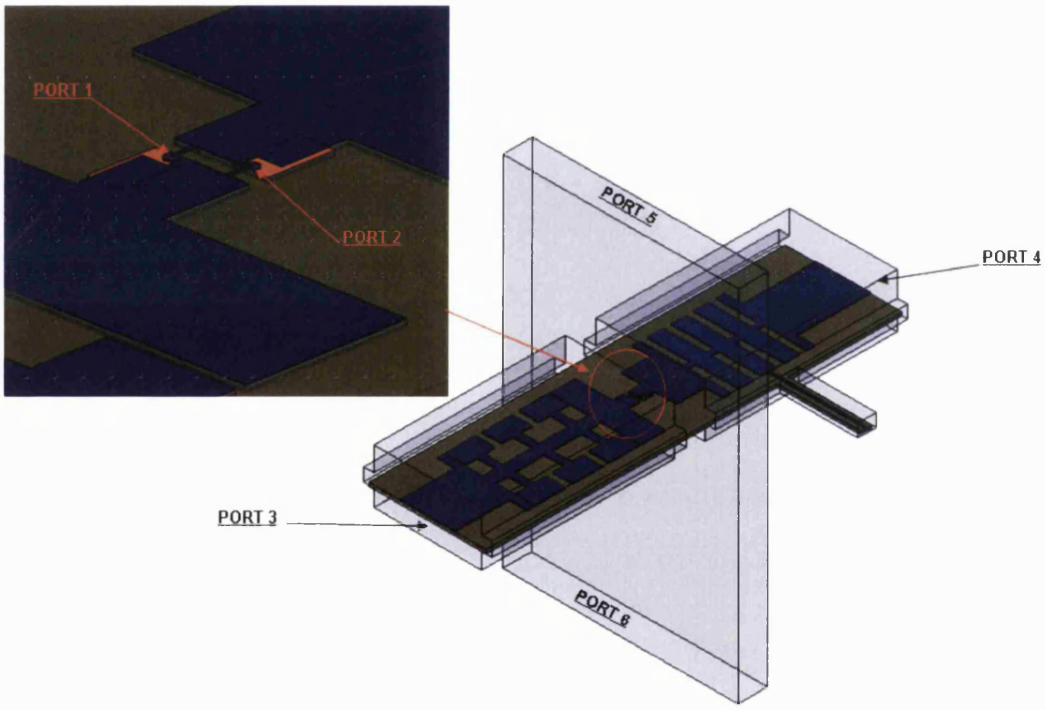

Fig. 4.35 Definition of the RF-antenna ports at the RF frequency

The diode parasitics and RF antenna model are presented in fig. 4.34 and 4.35. The S-parameters were calculated for the RF frequency range 180 GHz-220 GHz with the following port definitions:

- Port 1 antiparallel diode 1 port
- Port 2 antiparallel diode 1 port
- Port 3 IF filter output

- Port 4 LO antenna input
- Port 5 RF antenna source
- Port 6 RF antenna backshort

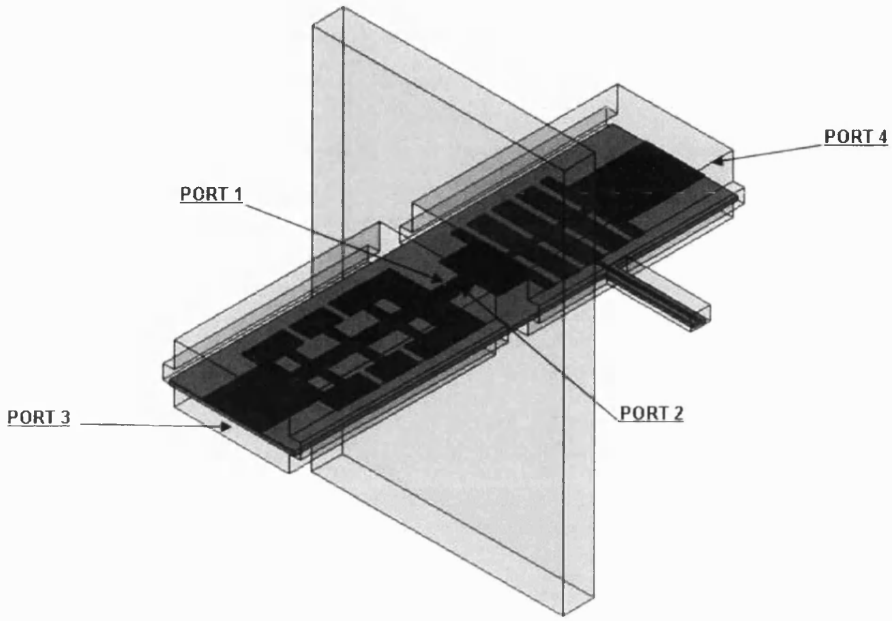

Fig. 4.36 Definition of the port on RF-antenna at the RF frequency

The diode ports 1 and 2 were defined using the coaxial approach presented in the previous section.

At the LO frequency band 80 GHz-120 GHz (Fig. 4.35) the port definitions were:

- Port 1 antiparallel diode 1 port
- Port 2 antiparallel diode 1 port
- Port 3 IF filter output
- Port 4 LO antenna input

All the waveguide impedance ports were defined as Z_{pv} to match the waveguide characteristic impedance definition in ADS. For the same reason the stripline ports and diode ports were defined using the $Z_{pi.}$ characteristic impedance representation. The Z_{pv} definition of characteristic impedance is the most appropriate for waveguide, whereas Z_{pi} impedance is more appropriate for stripline [4.18].

All the HFSS simulation results were exported into ADS as SnP files.

Fig. 4.36 presents the ADS circuit used to compute the conversion loss of the integrated mixer.

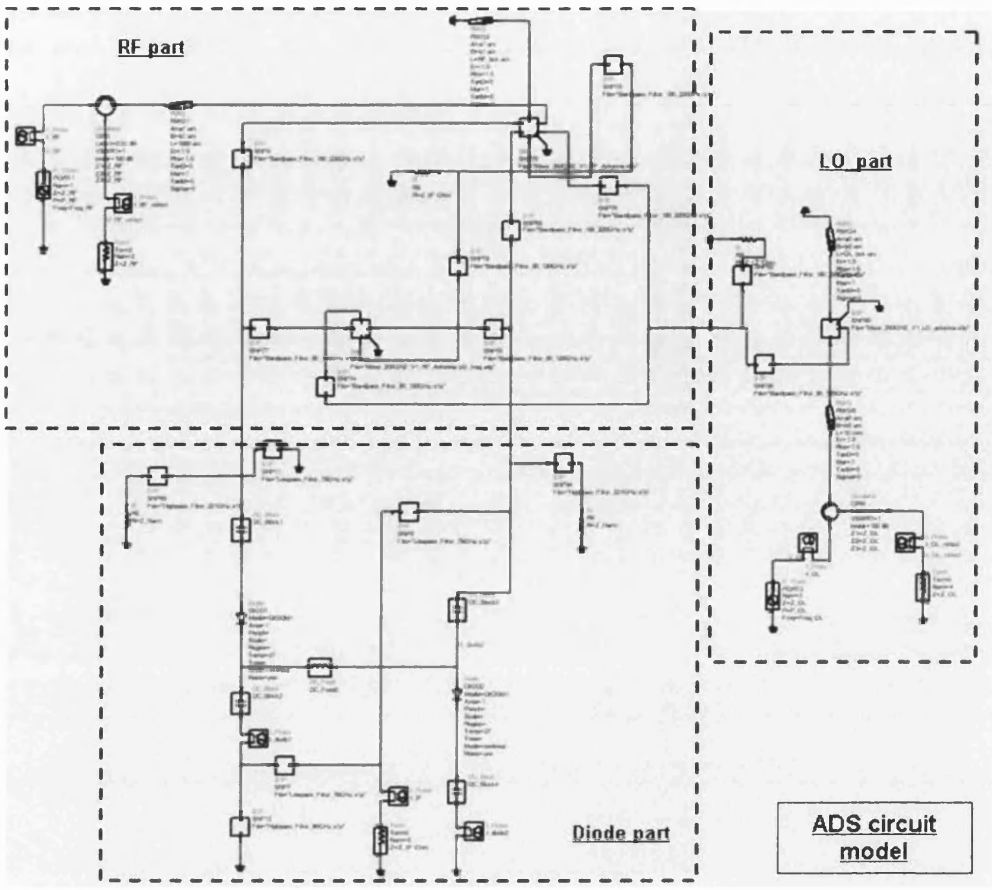

Fig. 4.37 ADS circuit model for the SHP integrated mixer.

The LO section of the ADS circuit (Fig. 4.37) includes the LO source, a length of waveguide transmission line and the 3 port S-parameters (S3P) corresponding to the response of the antenna between 80-120 GHz. Each port in the S3P box needs to be carefully attached to its corresponding port in HFSS. The LO circuit source is connected to Port 1, Port 2 is connected to a tuneable circuit backshort and Port 3, which represents the stripline port in the HFSS simulation, is connected to an ideal 80-120GHz band-pass filter. Any residual RF signal, having passed through the LO low-pass filter, is directed by the ideal 180-220 GHz band-pass filter to a 10Ω load. The power being coupled from the source to the antenna is redirected to the RF section.

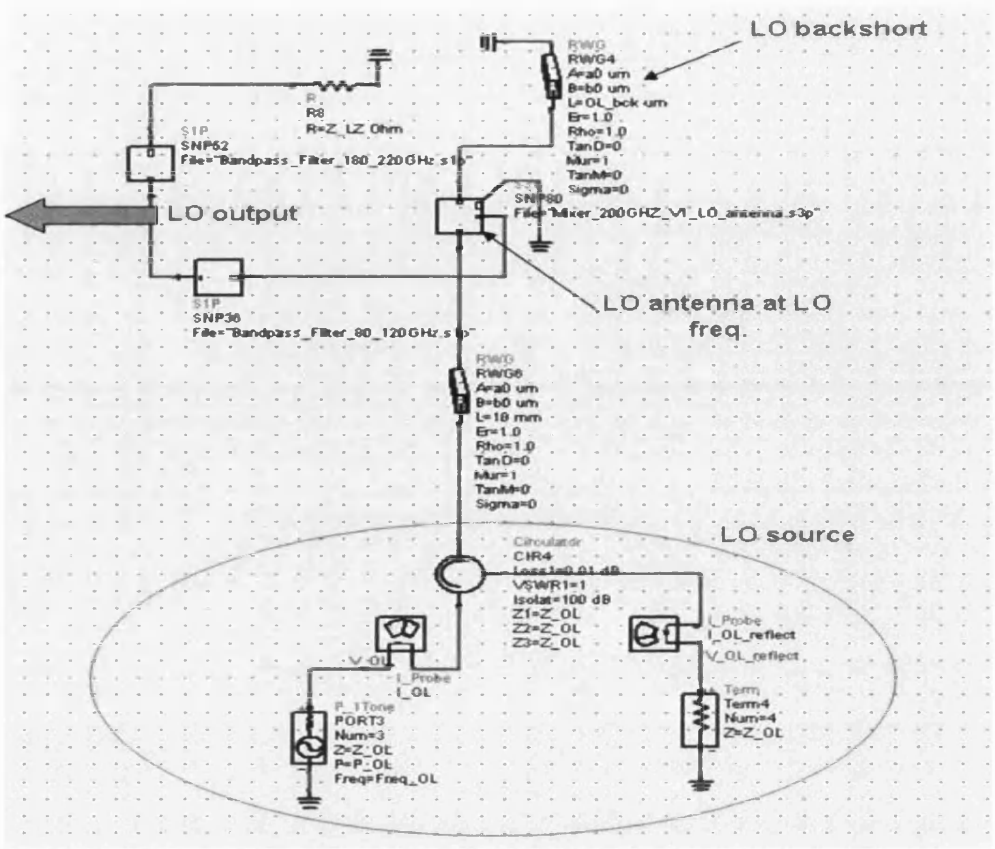

Fig. 4.38 ADS circuit model for the LO section of the circuit, including LO antenna, backshort and ideal filters.

The RF section of the ADS circuit model includes the RF source, RF waveguide backshort, a series of ideal frequency filters and SnP blocks representing the RF antenna at the LO and RF frequencies.

In the RF section of the ADS circuit (Fig. 4.38), the LO signal is coming from the LO section describe above. The LO is directed via an ideal band-pass filter to the RF antenna SnP block. The RF antenna S4P block model at the LO frequency includes the input port of the LO source, the output of the IF low-pass filter and the two anode ports. The IF output is connected to a 50 Ω resistor corresponding to the impedance of the SMA connector. The two anode ports are connected to the diode circuit section. The RF antenna S6P block model at the RF frequency includes 6 ports. The RF source and RF backshort are connected respectively to Port 5 and Port 6. Port 4 and Port 3 model respectively the RF residual power being transmitted to the LO antenna after passing through the LO low-pass filter and the residual power transmitted to the IF output after passing through the IF low-pass filter. Port1 and Port 2 model the

power coupled through the diodes. The anode Port 1 and Port 2 are connected to the ADS diode circuit section.

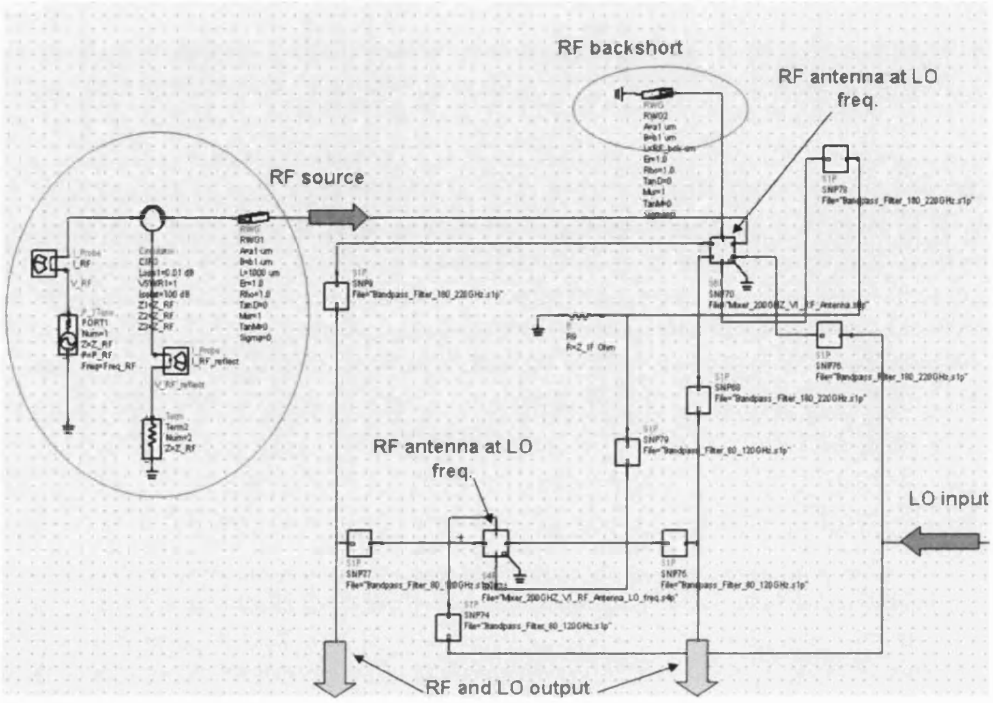

Fig. 4.39 ADS circuit model including diode, IF output and ideal frequency switches.

The diode section includes two ADS Schottky diode models. The saturation current, series resistance, ideality factor, zero bias junction capacitance and junction potential were all set in the diode model to match the Schottky diode fabricated during this work. Table 4.2 summarises the diode values.

The diode section contains a set of ideal filters acting as perfect frequency switches which redirect the IF signal to an output load. (Z_IF). The higher order harmonic frequencies generated by the diodes are filtered out by a 10Ω resistor (Z_Harm). Fig. 4.39 presents a closer view of the diode section.

Diode Characteristics	Typical Diode
Rs (Ω)	18-15
Cjo (fF)	3.5
ideality η	1.24
Vbi (V)	0.81
Isat (A)	3.10-14

Table 4.1 Electrical characteristics used in ADS Schottky diode model

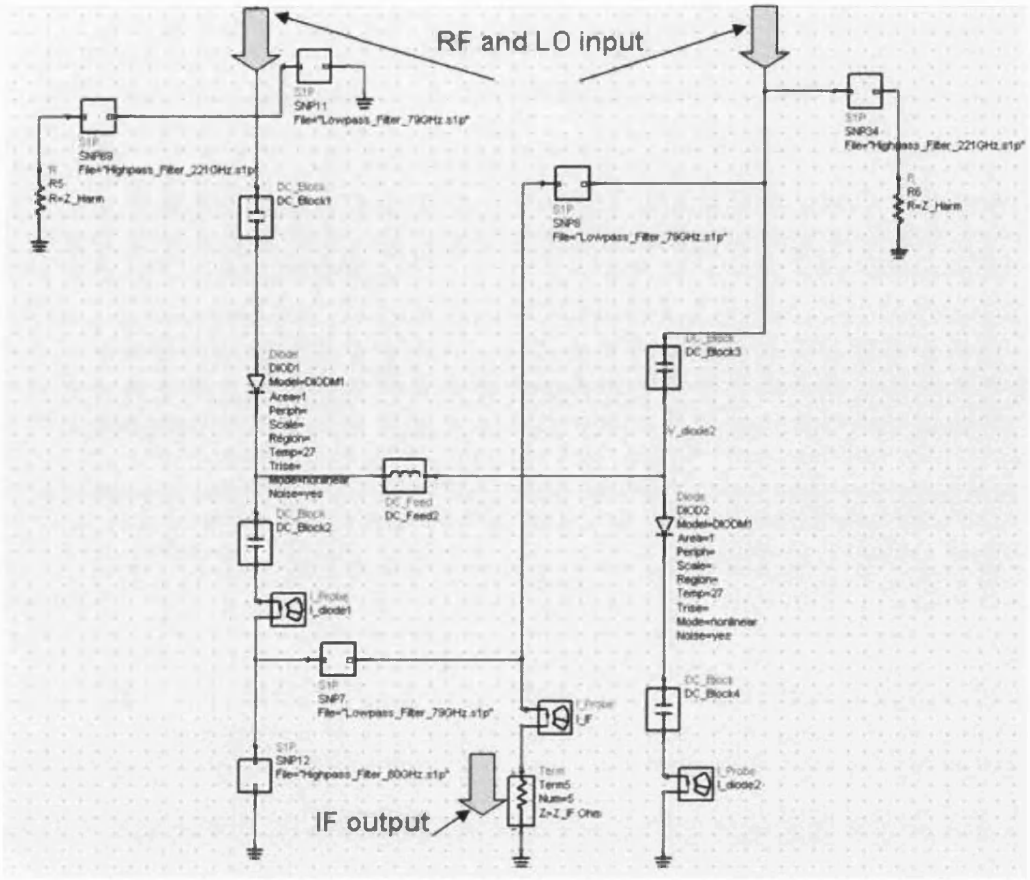

Fig. 4.40 ADS circuit model including diode, IF output and ideal frequency switches.

4.2.6 Simulated performances of integrated mixer

Using the ADS harmonic balance circuit configuration presented above, the integrated mixer circuit fabricated during this research was modelled. The goal of this simulation was to determine the conversion loss expected for the integrated mixer and not to optimise the RF circuit. The fabrication of the integrated mixer was completed before finalising the ADS circuit modelling tool. For this reason the optimisation was only carried out on the antenna and LO and IF filter using HFSS.

Fig. 4.40 presents the integrated mixer SSB conversion loss as a function of frequency.

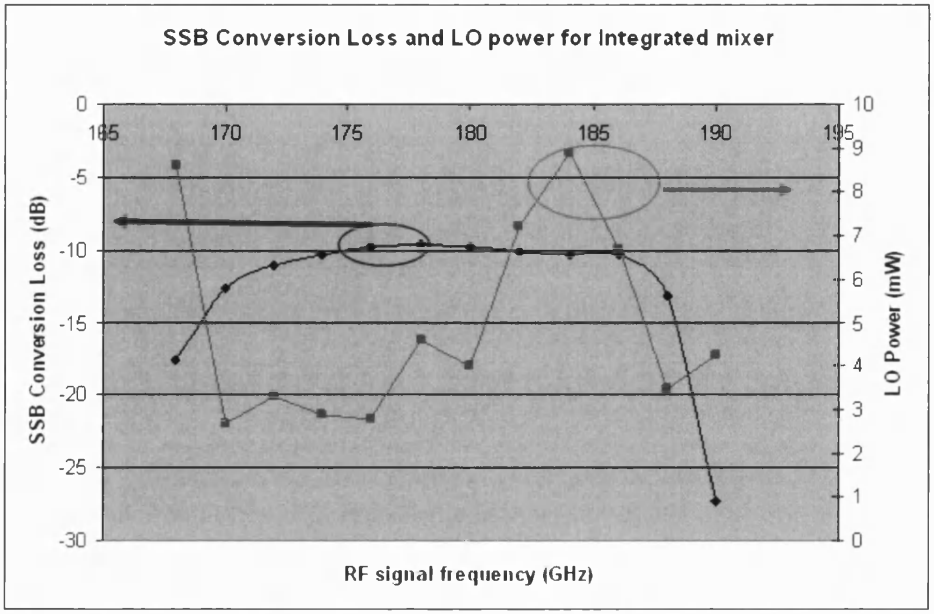

Fig. 4.41 Conversion loss and LO power as a function of RF signal frequency for integrated mixer.

The conversion loss for the mixer was computed for each frequency for the optimum LO backshort position. The RF backshort was kept fixed to find the instantaneous bandwidth of the mixer. The IF frequency was kept at 1.5 GHz and the RF signal was set at 10 μW (-20 dBm). The LO power was tuned for best performance for each frequency. Fig 4.40 shows a 9.6 dB minimum conversion loss achieved at 178 GHz with an LO power of 4.6 mW.

4.2.7 Comparison of integrated mixer with membrane integrated mixer

A fabrication option was added to the integrated mixer mask. This option was a set of masks to allow the thinning down of the region of GaAs directly underneath the Schottky diodes. This provided the ability to create a membrane below the diodes. To fabricate this membrane, a few additional steps were required. First a backside alignment was needed to align the region to be thinned down and an AlGaAs stop-layer had to implemented in the GaAs Schottky diode wafer to stop the backside etching and create the membrane. Below the diode, 25 μm of GaAs was etched away, leaving a membrane of 5 μm thickness. Fig.4.42 presents the 3D representation of this integrated mixer membrane.

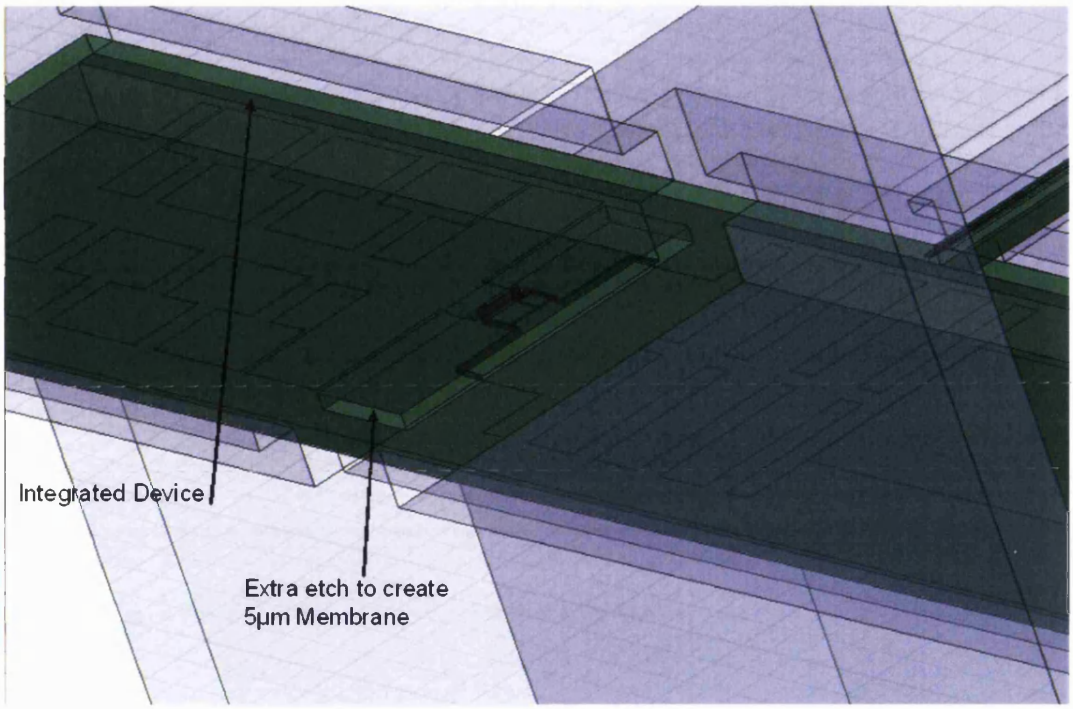

Fig. 4.42 3D representation of the membrane integrated mixer.

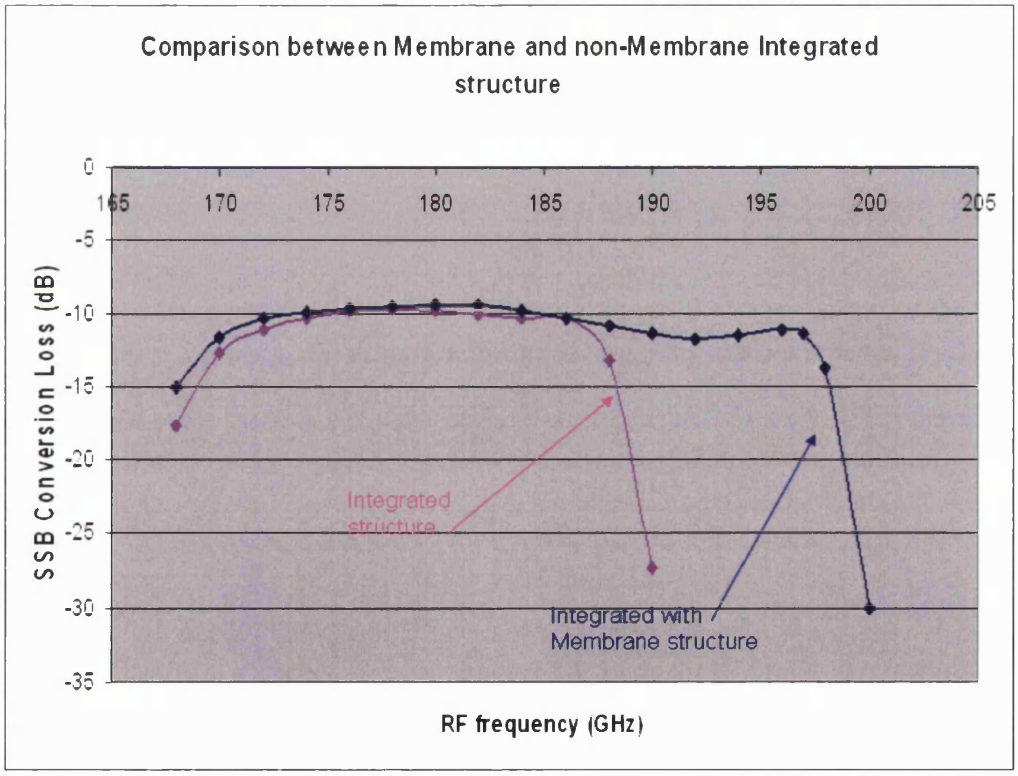

Fig. 4.43 Calculated conversion loss as a function of RF signal frequency for integrated mixer versus integrated membrane mixer.

This membrane integrated mixer was simulated and the conversion loss as a function of RF signal frequency is compared with that of the integrated mixer in Fig.4.43.
The results show a broader frequency response for the membrane device compared with the integrated mixer. The non linear simulations gave a SSB conversion loss below 13 dB between 168 GHz to 198 GHz. This broader band of operation for the membrane is due to the decrease in parasitic capacitance around the diode region. This decrease improves the diode impedance match with its embedding impedance.

4.2.8 Membrane integrated mixer with mesa structure.

The mask set used to fabricate the integrated mixer is described in Chapter 6. During the fabrication the IF and RF filter are built on top of a layer of SiO_2, n^+-*GaAs* and *n-GaAs*. The conversion loss for this structure was simulated for the integrated and membrane structure and compared with a structure where the RF and IF filter are formed directly on top of the semi-insulating GaAs. Fig 4.44 illustrates the mesa structure and Fig. 4.45 shows the conversion loss comparison between the different designs.

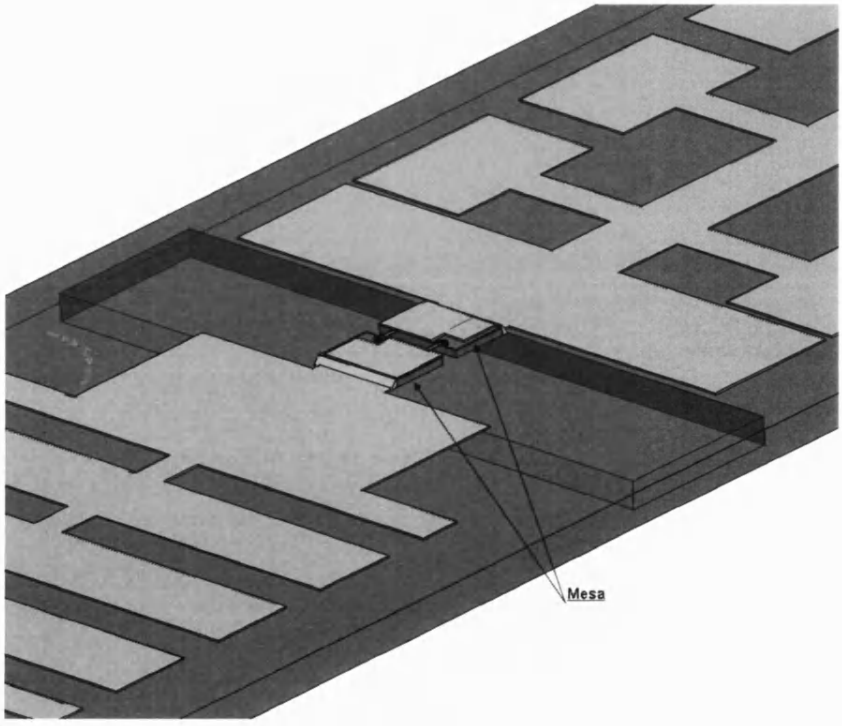

Fig. 4.44 Membrane integrated mixer with Schottky diode on a mesa.

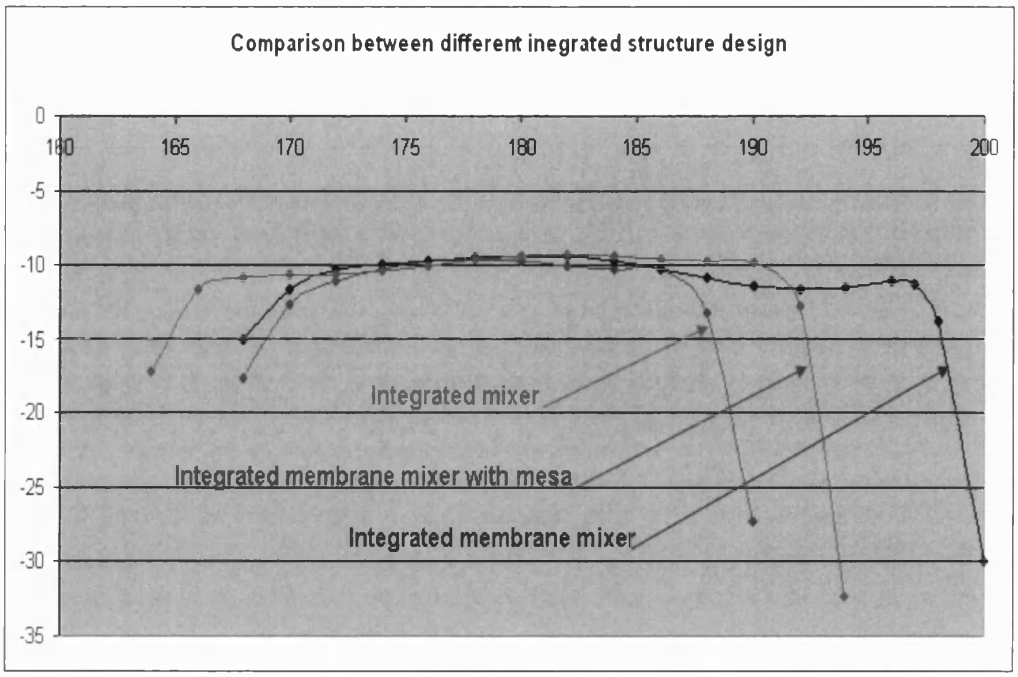

Fig. 4.45 SSB Conversion loss as a function of RF signal frequency for integrated mixer, integrated membrane mixer and integrated mixer with the diode on mesa structure.

Fig. 4.44 is a plot of the conversion loss for the two different configurations shown in Fig 4.42 plus the structure in Fig.4.43 which represents the integrated membrane mixer with mesa. Comparing the integrated membrane mixer (IM) and the integrated membrane mixer with mesa (IMmesa), the simulation shows a similar instantaneous bandwidth for the two structures. The IMmesa mixer is shifted 7GHz to the left compared to the IM mixer. This shift can be explained by the substitution of the extra capacitance brought between the n^{+}-*GaAs* layer and the filter metal layer Fig.4.45.

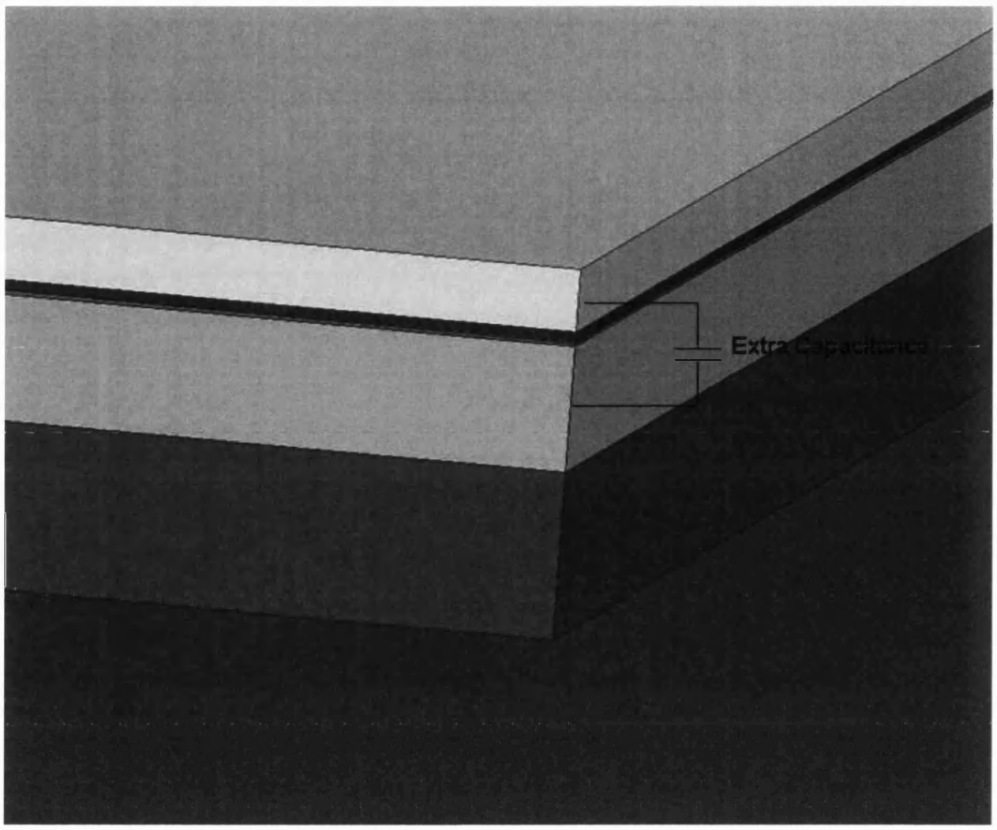

Fig. 4.46 Extra capacitance due to low doped material between n^{+}-*GaAs* and metal filter.

4.3 Simulation of Fixed-Tuned Integrated Membrane Mixer

Following the successful integration of the Schottky diode with the IF and RF filters using the tunable mixer block circuit, a fixed-tuned circuit was modelled and optimised for fabrication using the processes develop during this research.

The aim of this work was to design a broadband fixed-tuned sub-harmonically pumped mixer at 183 GHz featuring an antiparallel pair of planar Schottky diodes monolithically integrated on a 50 µm-thick substrate. The mixer layout was optimised using a combination of HFSS and the ADS non-linear circuit simulation software. The optimisation of this circuit was mainly done with the major collaboration of Hui Wang, Bertrand Thomas and Alain Maestrini from respectively LERMA, Observatoire de Paris, Rutherford Appleton Laboratory and LISIF – Université Paris 6.

Fig. 4.47 and Fig. 4.48 present respectively the 3D representation of the 183GHz fixed-tuned mixer and the mixer block and Fig.4.49 a picture of the actual mixer.

This mixer configuration offers the advantages of only requiring two parts compared to the previous design which required 4 parts, making it cheaper to fabricate.

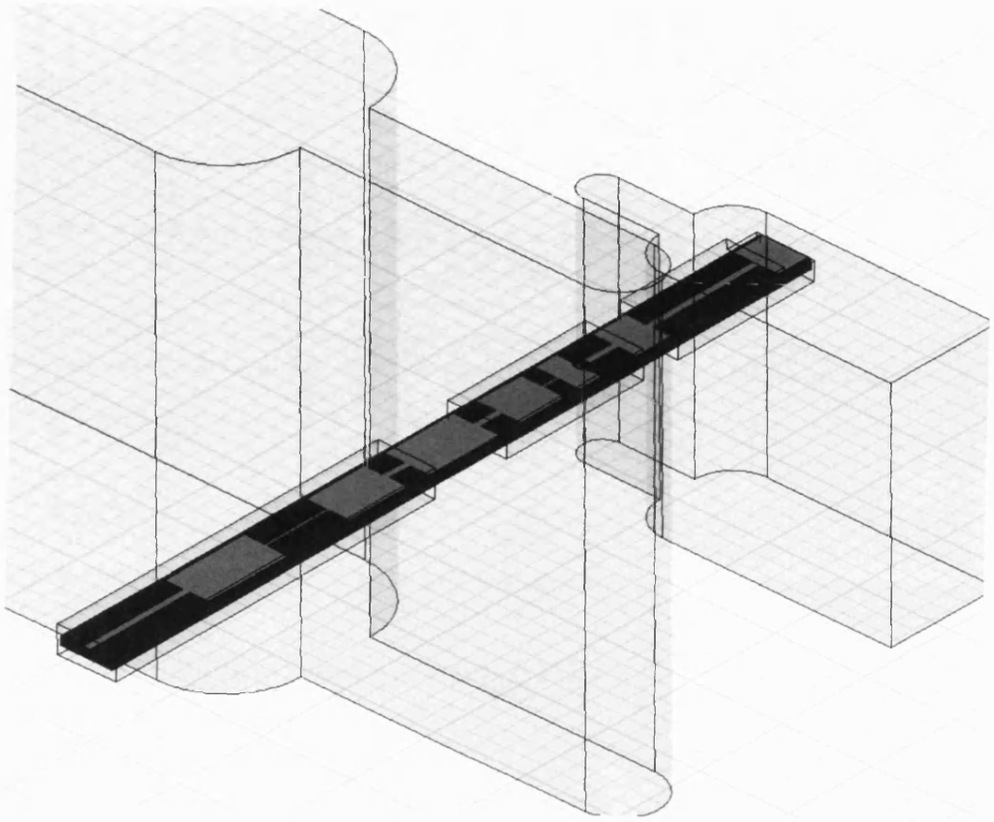

Fig. 4.47 3D HFSS representation of the 183 GHz fixed-tuned mixer.

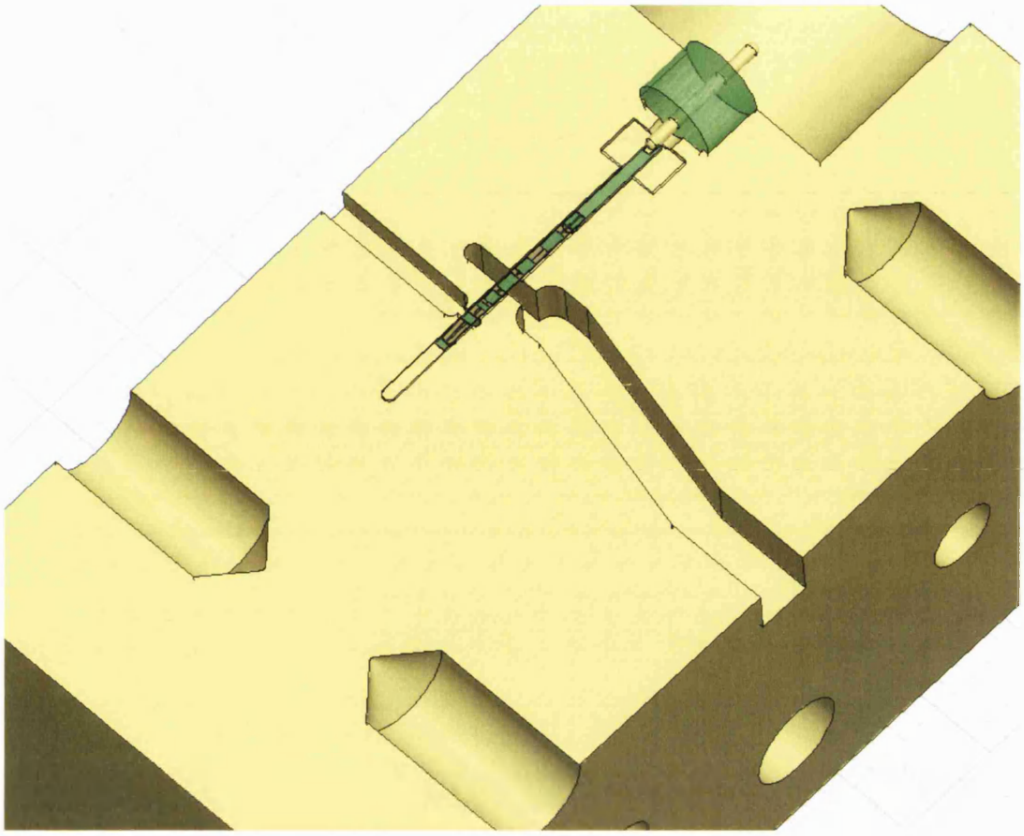

Fig. 4.48 3D representation of the 183 GHz fixed-tune integrated mixer in mixer block.

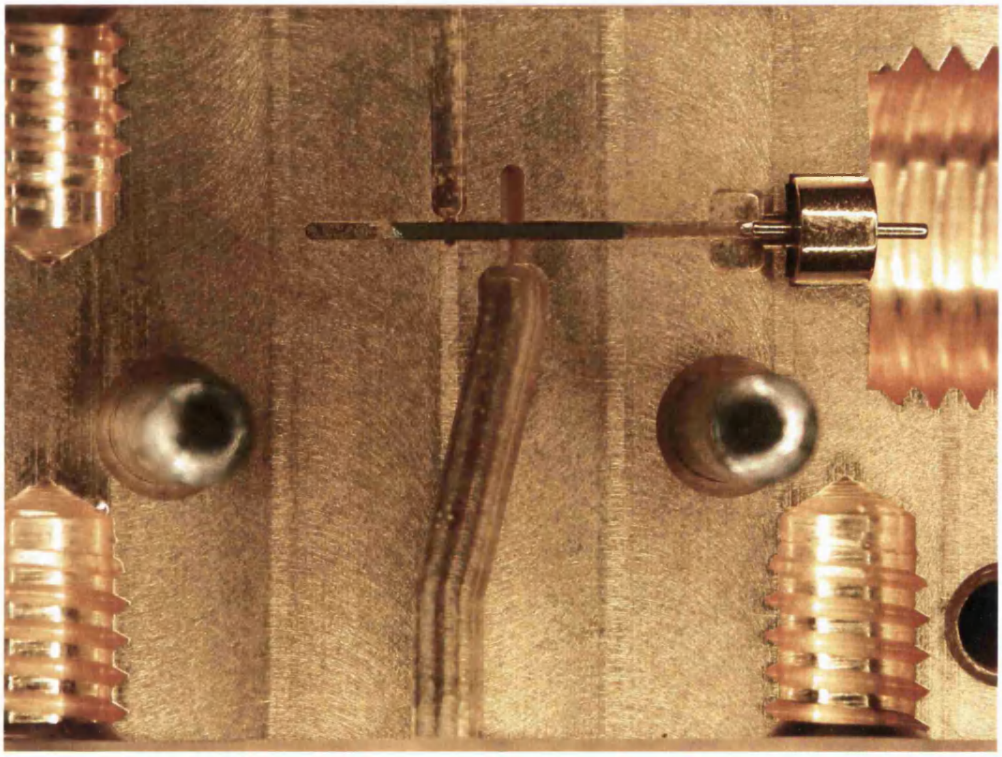

Fig. 4.49 Picture of the 183 GHz fixed-tune integrated mixer in mixer block.

The mixer block layout consists of two halves of a metal block, split along the E-plane of both the RF and LO waveguides, resulting in a simple mixer assembly and low cost mechanical structure. The integrated GaAs mixer circuit is inverted and suspended in an enclosed channel crossing the RF and LO waveguides. One end of the circuit is directly connected to the mechanical block providing a precise IF/DC grounding point. The other end of the circuit is connected to another stripline quartz circuit to output the IF signal. Wide E-probe waveguide-to-suspended stripline transitions are used to couple both the RF and LO signals into the channel. Reducing the height of both RF and LO waveguides in the vicinity of the E-probe transitions was found necessary to achieve broadband operation as mentioned in [4.19]. Two low-pass stripline filters are used to prevent the RF signal from coupling to the LO waveguide and the LO signal from leaking towards the IF connection.

The optimisation was carried out by first taking the typical diode characteristics with the process develop during this research (Table 4.1) coupled to an ideal matching element load. The non-linear simulation results gave an optimum LO power of 1.5mW for the pair of diodes, with embedding impedances Z_{RF}=(82+j45) Ω at f_{RF}=183 GHz and Z_{LO}=(197.5+j182) Ω at f_{LO}=89.5 GHz. The IF load impedance was set to 100 Ω. The RF and LO matching circuits were then optimised in a sequence of linear simulations (Agilent ADS) to produce an embedding impedance as close as possible to the value found previously. Each individual section of the mixer circuit was solved using 3D EM finite element (HFSS) and imported as S-parameter files in the circuit simulator before optimising the circuit. Finally, a non-linear analysis of the entire mixer circuit, including the S-parameter data of the mixer EM structures, was used to compute the mixer noise temperature and conversion loss. Results from these simulations are presented in Fig. 4.50.

The performances were computed over the frequency range 160-200 GHz. Fig.4.50 shows the conversion loss for different values of LO input power. The expected SSB conversion losses are higher than –7 dB between 160 and 196 GHz using 2 mW of LO power, with a best value of –6.1 dB at 183 GHz. Considering additional losses of about 2 dB due to the total conductor and dielectric loss of the horn and waveguide, as well as possible mismatches between the IF output of the mixer and the first IF low noise amplifier, the DSB mixer conversion loss is expected to be approximately 5.1 dB at 183 GHz.

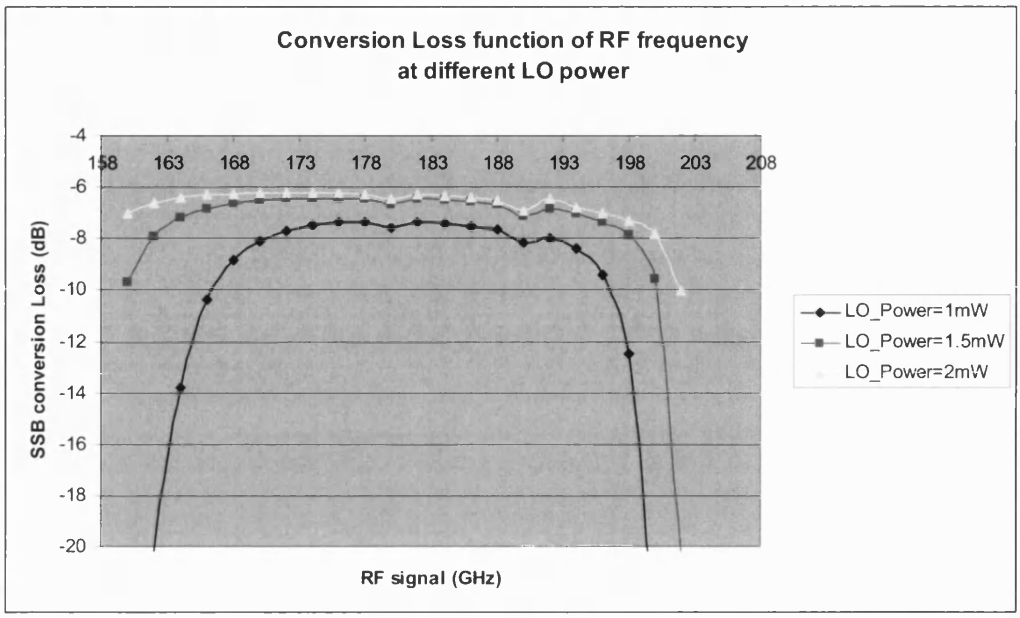

Fig. 4.50 Simulated SSB conversion loss of the integrated fixed-tuned 183 GHz mixer.

References – Chapter 4

[4.1] P. H. Siegel, A. R. Kerr, "Computer Analysis of microwave and millimeter-wave mixers", *IEEE Transactions on Microwave Theory and Techniques*, Vol. MTT-28, pp. 275-276, March 1980.

[4.2] M. T. Faber, J. Chramiec, M. E. Adamski, "Microwave and millimeter diode frequency multipliers," *Artech House, Inc, MA*, 1995.

[4.3] Lawrence E. Dickens, " Spreading resistance as a function of frequency", *IEEE Transactions on Microwave Theory and Techniques*, vol. MTT-15, pp. 101-109, February 1967.

[4.4] Joseph A. Calviello, "Advanced devices and components for the millimeter and submillimetre systems", *IEEE Transaction on Electron Devices*, Vol. ED-26, pp. 1273-1281, September 1979.

[4.5] Kathy Mckinney, Robert J. Mattauch, William L. Bishop, "Design, fabrication and performance of a whiskerless Schottky diode for millimeter and submillimetre wave applications", *IEEE Southeastcon. Proc.*, 1985, pp. 111-115.

[4.6] C. H. Blanton, M.S. Thesis, University of Virginia, 1984.

[4.7] C. S. Setzer, Dissertation, University of Virginia , 1981.

[4.8] W. L. Bishop, "A novel whiskerless Schottky diode for millimeter and submillimeter wave applications," *IEEE MTT-S Digest*, vol. Q-16, pp. 607-610, 1987.

[4.9] A. R. Kerr, *et al.*, *NASA Technical Memo.*, no. 79616, 1978.

[4.10] W. H. Hayt, "Engineering Electromagnetics," McGraw-Hill, New York, 1981.

[4.11] T. W. Crowe, *et al.*, " GaAs Schottky Diodes for THz Mixing Applications", *Proc. IEEE*, Vol. 80, pp. 1827-1841, November 1992.

[4.12] J. Hesler, Ph.D. thesis, University of Virginia, January 1996.

[4.13] A. Meastrini, B. Thomas, "Report on evaluation of the capabilities of united monolithic semiconductors to produce Schottky diode based mixers in the band 100-380 GHz", *proceedings of the round-table discussion on Schottky technology,* ESTEC, Noordwijk, The Netherlands, March 16, 2004.

[4.14] I. Mehdi and P.H. Siegel, "Effect of parasitic capacitance on the performance of planar subharmonically pumped Schottky diode mixers", *5th Int. Symp. On Space THz tech*, University of Michigan, Ann Arbor, pp.379-393, 1994.

[4.15] B. Thomas," Etude et réalisation d une tête de réception hétérodynes en ondes submillimétrique pour l'étude des atmosphères et surfaces de planètes", These de Doctorat, Université Paris 6, 2004.

[4.16] D. M. Pozar, "Microwave engineering," John Wiley and Sons Inc., New York, 1998.

[4.17] P.H. Siegel, J.E. Oswald, R.J. Dengler, D.M. Sheen and S.M. Ali," Measured and computed performance of a microstrip filter composed of semi-insulating GaAs on fused quartz substrate", *IEEE Microwave and Guided Wave Letters*, Vol. 1, No. 4, pp78-80, April 1991.

[4.18] Bruno Bianco, Luigi Panini, Mauro Parodi, and Sandro Ridella, "Some Considerations about the Frequency Dependence of the Characteristic Impedance of Uniform Microstrips," *IEEE Transactions on Microwave Theory and Techniques*, vol. MTT-26, pp. 182-185, March 1978.

[4.19] S.C. Shi and J. Inatani, "A waveguide-to-Microstrip Transition with a DC/IF Return path and an Offset Probe", *IEEE Transactions on Microwave Theory and Techniques*, MTT-45, pp. 442-446, March 1997.

[4.20] Stephen A. Maas, " Microwave mixers ", Artech House Inc., 1986

[4.21] M. T. Faber, J. Chramiec, M. E. Adamski, "Microwave and millimeter diode frequency multipliers," *Artech House, Inc, MA*, 1995

Chapter 5

Flip-Chip Schottky Diode Fabrication

This chapter covers the development of the fabrication process for flip-chip Schottky diodes. This development was the key in moving towards the fabrication of a membrane-diode mixer. In this chapter we will review the development of submicron Schottky diodes, the study of different metals for producing high yield, low series resistance, low ideality factors and reliable flip-chip diodes. Finally this chapter reviews the full fabrication process of a complete flip-chip Schottky diode.

5.1 Submicron Schottky diode

Submillimetre-wave mixers require diodes with anode diameters of less than half a micron. Small diameter anodes will decrease the device anode capacitance and improve performances. Sub-micron resolution is difficult to achieve with the use of contact photolithography. For this reason the e-beam lithography process was developed to write submicron features.

5.1.1 E-Beam Lithography

In the e-beam lithography process, high energy electrons are used to expose the e-beam resist coated on the wafer chip. The resist used in this process is polymethylmethacrylate (PMMA). PMMA is a positive resist. A resolution as low as 10 nm can be achieved depending on the process, material, aspect ratio, electron energy and current density. When an electron enters the PMMA, energy is transferred to molecules in the resist, resulting in bond breaking. This bond breaking in the resist increases the solubility of PMMA in the developer. The developer used in this case is a 1/3 solution of methyl-iso-butyl-ketone (MIBK)/isopropanol. Unlike photolithography no mask is used in e-beam. The design is first defined in a CAD software, before being used to write the pattern. The masks were designed under the Raith system. All the developments and studies of metal deposition were performed using e-beam lithography. Fig. 5.1 presents an example of one of the e-beam masks used during beam writing of some test anode structure.

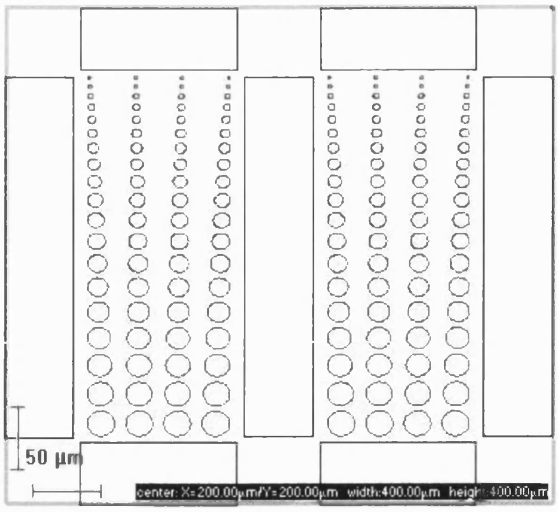

Fig. 5.1 Array of anodes surrounded by ohmic contacts.

5.1.2 Dry etch of submicron via-holes in silicon dioxide

Test or device anodes with diameters below one micron were defined using the PMMA e-beam resist. The anode defined in PMMA serves as a mask to etch the silicon dioxide and open a via-hole to the n-GaAs layer. Metal is then deposited through the via to create the Schottky diode. Via-holes in silicon dioxide can be opened using hydrofluoric acid wet etching for anodes larger than 1 µm in diameter. For smaller anodes, due to the isotropic nature of the hydrofluoric acid etching, only anisotropic dry etching could allow anode sizes below 1 µm. A process was developed to allow dry etching of the anode with the use of poly-methyl-methacrylate (PMMA) as a mask. It was also important to accurately control the etching rate of silicon dioxide to minimise the damage which could occur on the surface of the GaAs. Damage of the surface of GaAs results in a degraded ideality, high series resistance and in a poor Schottky diode.

The aim of this study was to find the set of parameters which would give the highest selectivity of etching between SiO_2/PMMA, and also a relatively high and stable etch rate. The selectivity is quoted as a ratio of the etch rate of the material which is the primary layer to be removed and the etch rate of another material present during the process. A selectivity of silicon dioxide to PMMA of 3 or 3:1 means that the SiO_2 etches three times faster than the PMMA.

Twelve experiments were carried out using: 1.2 μm of sputtered SiO_2 deposited on GaAs and single layer of PMMA resist, patterned with features ranging from 30 to 0.5 μm.

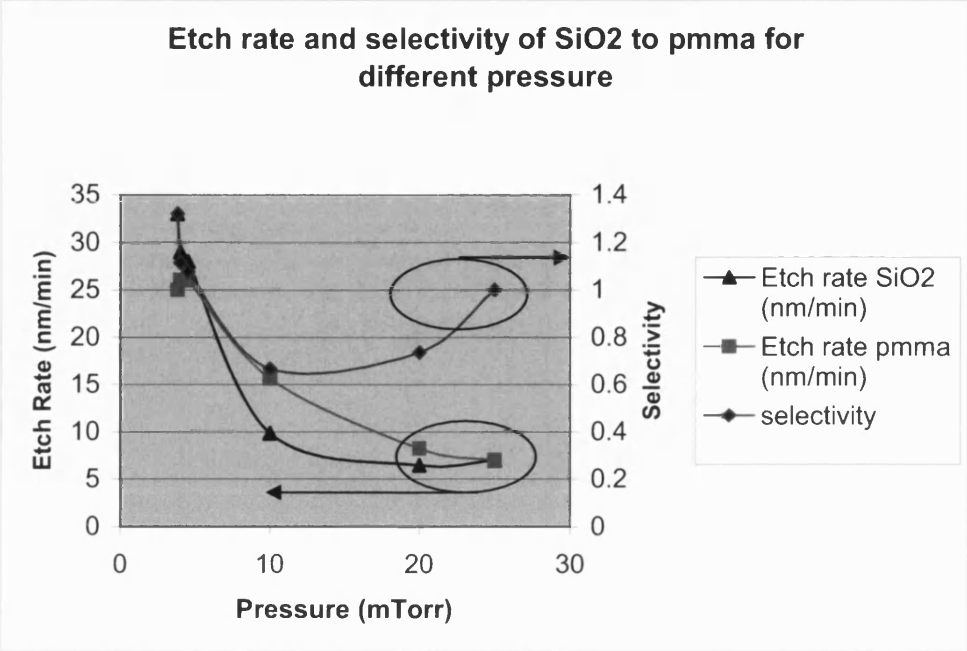

Fig. 5.2 Etch rate and Selectivity of SiO2 to PMMA function of process pressure.

Fig. 5.2 shows the etching rate of SiO_2 and PMMA as a function of the pressure in 25 sccm CHF_3 plasma at 150 Watts of RF power. These experiments show that both etching rate and selectivity are highly dependent on the pressure. The etching rates of SiO_2 and PMMA increase at low pressure and the selectivity of SiO_2 versus PMMA also increases at lower pressure. From these experiments, in order to increase the selectivity we need to work at lower pressure. The pressure can not be reduced below 3mTorr due to the introduction of CHF_3. In order to keep a stable low pressure the CHF_3 has to be at 20 sccm. The last measurement at 25 mTorr suggests that we can increase the selectivity for higher pressure. The selectivity of PMMA with silicon dioxide at relatively high pressures has been studied [5.1]. The use of CHF_3 as the working gas during the RIE, has the advantage that it forms a fluoropolymer with the PMMA. This polymer, formed on top of the PMMA, has been shown to be harder than PMMA and to increase the selectivity [5.1].

Experiments with pressures above 25 mTorr have not been carried out due to the risk of polluting the ICP chamber during long plasma etches.

Fig. 5.3 shows the effects of the RF power on the etching rate and selectivity. The SiO_2 etch was performed in 20 sccm CHF_3 plasma at a pressure of 3.5 mTorr and RF power between 50 to 150 W. The etch rate of SiO_2 and PMMA increase with the RF power. With these parameters, the main mechanism to etch SiO_2 relies mainly on mechanical etching rather than chemical etching. For this reason, higher RF power increases ion energy and consequently increases the etching rate. Figure 5.3 shows that the selectivity is approximately constant with changing the RF power, again because the chemical etching is low versus physical sputtering.

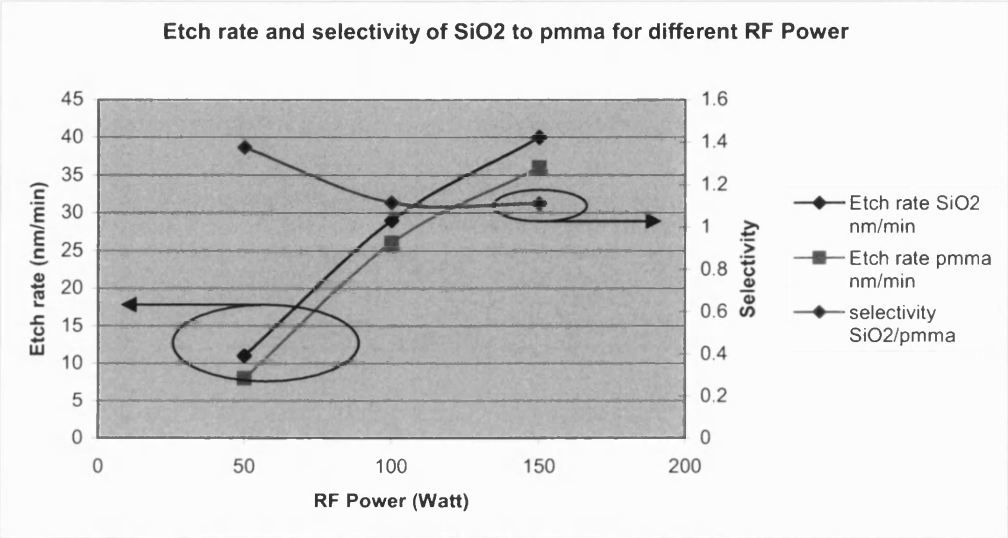

Fig. 5.3 Etch rate and Selectivity of SiO2 to PMMA function of process RF power.

In conclusion for silicon dioxide etching of the via for the planar diode, a low pressure of 3mTorr was found to have the best selectivity. A good trade-off between etch-rate/selectivity can be found for a process with: 20 sccm of CHF_3; RF power of 100 Watts and pressure of 3 mTorr. This process will keep a reasonable etch rate control and a relatively high selectivity.

Many groups have reported degradation of the series resistance and ideality after dry etching [5.2] due to damage of the GaAs surface. Different treatments are possible to anneal this damage, such as GaAs wet etching or thermal annealing [5.2].

5.2 Study of different junction metals

Refractory metal Schottky barrier diodes are commonly used for many applications in semiconductor electronics because of inherent high stability of the barrier metal.

Three different deposition methods have been studied during this research: platinum electro-deposition, tungsten sputtering and titanium/platinum/gold e-beam deposition. The aim of this study was to develop a process which could produce Schottky diodes with the following requirements:

- Low series resistance (R_s) and Low ideality factor (η)
- High yield to allow future monolithic integration on membrane device
- Good characteristic uniformity across the entire chip
- High thermal stability
- Reproducible process from batch to batch

These three metal barriers were chosen due to the inherent advantages of their deposition methods.

An automated I/V and C/V measurement was developed under LabVIEW to measure the different batches of diodes. The interface and LabVIEW program are described in Chapter 7.

5.2.1 Tungsten sputtering deposition

Tungsten (W) is classified as a refractory metal and has been reported to produce diodes with high thermal stability compared with other metals [5.3]. The thermal stability of the diode barrier is crucial for many reasons. The barrier needs to be stable during the different steps of the process required to make the device. Also for space or military applications the diodes must be stable to thermal cycling to successively pass the reliability norms.

Due to the high melting point of tungsten (3000 °C), sputtering is the preferred method to deposit W. The tungsten was sputtered using a Ultra-High-Vacuum chamber [5.4]. High energy argon ions are accelerated in a large potential gradient to bombard a tungsten cathode. Tungsten atoms near the surface are vaporised through momentum transfer and deposited on the GaAs substrate as a thin film. The tungsten atoms sputtered on the substrate surface are highly energetic and can damage the semiconductor surface. This can be rectified by annealing the sample at 400 °C for 2-4 minutes to unify the metal on the surface [5.5]. Table 5.1 gives an example of the I/V characteristic before and after annealing.

A_d	Before Annealing 20 μm	After Annealing 20 μm
I (mA)	*V (mV)*	*V(mV)*
1	*700*	*550*
0.1	*540*	*466*
0.01	*274*	*390*
0.001	*190*	*320*
η (ideality)	*1.41*	*1.2*
R_s	*85.3*	*14.6*

Table 5.1 I/V characteristics of a 20 μm anode before and after annealing.

Various powers and pressures were studied. The best deposition parameters were chosen as a function of the diode DC parameters after annealing.

The anodes were deposited at an RF power of 8 Watts with periods of 10 minutes on/off for a total sputtering time of 60 minutes (to the allow sputtering head to cool down). The deposition rate was 2.75 nm/min and a total of 80 nm of tungsten was deposited. Table 5.2 presents the best 20 μm,18 μm and 16 μm Tungsten diodes achieved with those parameters.

A_d	20 μm	20 μm	20 μm	18 μm	18 μm	16 μm	16 μm
I (mA)	*V (mV)*	*V(mV)*	*V (mV)*	*V(mV)*	*V (mV)*	*V(mV)*	*V (mV)*
1	*538*	*530*	*550*	*512*	*520*	*536*	*545*
0.1	*450*	*440*	*466*	*417*	*423*	*454*	*462*
0.01	*374*	*364*	*390*	*331*	*339*	*381*	*385*
0.001	*302*	*290*	*319*	*250*	*260*	*312*	*315*
η	*1.22*	*1.26*	*1.2*	*1.37*	*1.34*	*1.17*	*1.19*
R_s	*18*	*18*	*14.6*	*15.7*	*20.2*	*14.6*	*21.3*

Table 5.2 I/V characteristics of Tungsten anodes.

Conclusion of Tungsten diodes:

The sputtering process to fabricate tungsten Schottky diodes was reliable from batch to batch. The homogeneity of the diode DC parameters from diode to diode was also good. From table 5.2 we see that the diode series resistance and ideality with this process will lead to high DC parameters for smaller anodes. This high diode characteristics will not be good enough for high-frequency applications.

5.2.2 Platinum Electro-Deposition

Electroplated platinum (Pt) contacts have been the standard technology for the past decade for the fabrication of low noise Schottky diodes. Pt forms stable compounds both with As and Ga semiconductors [5.6]. The platinum establishes the Schottky barrier and prevents Au diffusion into the semiconductor.

The in-situ electrochemical deposition method reported by several groups gives an oxide free Pt/GaAs Schottky barrier by etching the GaAs native oxide layer (Ga_2O_3/As_2O_3). This method produces a nearly ideal thermionic emission characteristics and ideality factor of n=1.05 [5.7]. This method has proven to give the best diode characteristics.

Sets of experiments were carried out to first determine the deposition rate of Pt and secondly to evaluate the quality of Schottky diode fabricated using this process. The solution used to electroplate Pt was a solution from Metalor at a concentration in platinum of 4 g/L. The temperature, current density and ON/OFF duty cycle are the main parameters for the electro-deposition. In order to control the current density in the small areas to be plated, a "drop method" was used in these experiments. A small droplet of plating solution is deposited in order to cover the entire area of GaAs to electro-plate. This configuration is depicted in Fig. 5.4 and has been published by S. T. G. Wootton [5.8].

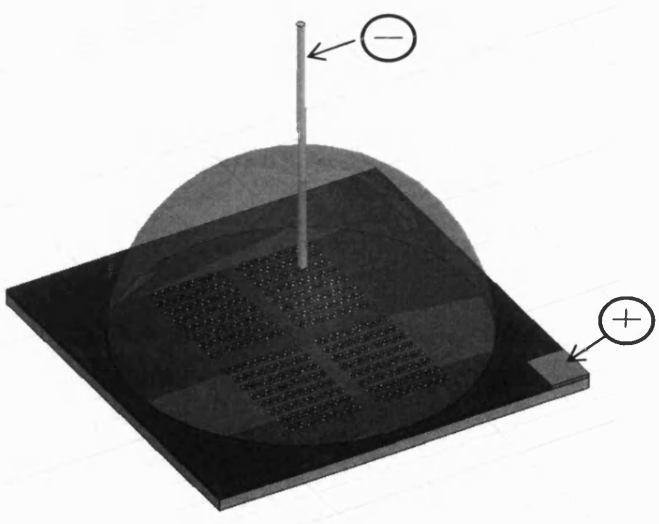

Fig. 5.4 Drop plating method

A current density of 40 nA/μm^2, a duty cycle of 10ms/500ms ON-OFF at a temperature of 40 °C was found to give the best results. Table 5.3 presents data for a batch 50 μm, 25 μm and 20 μm platinum diodes fabricated with those parameters.

A_d	50 μm	50 μm	25 μm	20 μm	20 μm	20 μm	20 μm
I (mA)	*V (mV)*	*V(mV)*	*V (mV)*	*V(mV)*	*V (mV)*	*V(mV)*	*V (mV)*
1	*736*	*735*	*770*	*788*	*789*	*788*	*787*
0.1	*664*	*663*	*698*	*710*	*714*	*713*	*711*
0.01	*600*	*593*	*618*	*640*	*645*	*642*	*641*
0.001	*532*	*524*	*552*	*572*	*577*	*574*	*573*
η	*1.16*	*1.17*	*1.12*	*1.15*	*1.15*	*1.15*	*1.15*
R_s	*4.5*	*3.4*	*6.7*	*11.2*	*7.9*	*7.9*	*9*

Table 5.3 I/V characteristics of Platinum anodes.

Conclusion of Electroplated Platinum diodes:

The electroplated platinum process has been used to fabricate diodes with very low ideality and series resistance. From Table 5.3 we can see that we could expect, in regard to the low DC parameters, fabricating small diameter anodes to use at a high frequency. Nevertheless, we found that the process was not reliable from batch to batch and that the yield on a batch was less than 30 %.

5.2.3 Titanium/Platinum/Gold Anodes

E-beam evaporated Schottky diodes are currently employed by several major groups such as the Jet Propulsion Laboratory (JPL) for sub millimetre-wave applications [5.9-5.11]. This well established process is also used, due to is high-reliability, to fabricate the gate in GaAs MESFET [5.11], [5.9]. Such contacts have also proved to exhibit excellent thermal robustness [5.11]. Table 5.4 shows the I/V characteristic of e-beam evaporated Schottky diodes before and after 15 min of RIE etching at an RF power of 200 W. The temperature during that etch reached 250 °C, but the diode characteristics were only slightly changed after this process. It was decided to decrease the RF power to 100 W to ensure the final quality of the diodes.

Throughout this work a Edwards E-Beam evaporator was used to evaporate titanium, platinum and gold.

It was found that the e-beam evaporator's chamber had to be cleaned carefully and several depositions had to be performed before good films could be obtained. As the

e-beam evaporator was used by many users, different type of metals were deposited. The deposition of Pt requires a high energy beam for evaporation and any metals or impurities present in the chamber could outgas during that deposition, resulting in the deposition of impurities.

Finally, the time between drying the sample in nitrogen after the oxide etch and loading it into the vacuum chamber of the evaporator was critical. This time was always kept to an absolute minimum (>30 s) to reduce GaAs oxide formation.

	Before RIE etching			After RIE Etching		
A_d	30 μm	20 μm	15 μm	30 μm	20 μm	15 μm
I (mA)	*V (mV)*	*V(mV)*	*V (mV)*	*V(mV)*	*V (mV)*	*V(mV)*
1	*500*	*545*	*587*	*513*	*542*	*585*
0.1	*422*	*467*	*507*	*431*	*460*	*501*
0.01	*352*	*397*	*437*	*354*	*388*	*427*
0.001	*286*	*331*	*371*	*285*	*320*	*358*
η	*1.12*	*1.12*	*1.12*	*1.17*	*1.15*	*1.17*
R_s	*13.5*	*13.5*	*15.7*	*14.6*	*15.7*	*16.8*

Table 5.4 Effect of RIE etching on diode characteristics

Tests were made to find which of the metal sequence Ti/Pt or Pt/Ti gives the best result. Table 5.5 compares the two fabrication sequences:

	Pt/Ti			Ti/Pt		
A_d	30 μm	20 μm	15 μm	30 μm	20 μm	15 μm
I (mA)	*V (mV)*	*V(mV)*	*V (mV)*	*V(mV)*	*V (mV)*	*V(mV)*
1	*745*	*810*	*851*	*519*	*540*	*561*
0.1	*649*	*699*	*722*	*446*	*467*	*488*
0.01	*562*	*602*	*600*	*379*	*400*	*411*
0.001	*484*	*519*	*500*	*313*	*334*	*344*
η	*1.32*	*1.41*	*1.7*	*1.12*	*1.12*	*1.14*
R_s	*13.5*	*13.5*	*32.5*	*7.9*	*7.9*	*6.7*

Table 5.5 Comparison of Pt/Ti and Ti/Pt anodes

It was found that the Ti/Pt anode characteristics were far better than the Pt/Ti ones. We believe the difference comes from the low pressure (7.10^{-7} mbar) achieved during deposition of Ti in Ti/Pt compared with the 7.10^{-5} mbar during Pt in Pt/Ti process. Furthermore, as a result of the temperature during evaporation of Pt being high, more out-gassing occurs polluting the metal semiconductor interface.

Sets of experiments have been carried out to determine the deposition rate of Ti for our system as it was found that the deposition rate had a large influence on the diode DC characteristics[5.12].The best results were achieved with Ti, Pt and Au deposited at the respective deposition rate of 1.1 nm/s, 0.3 nm/s, 1 nm/s. Table 5.7 presents different batches of Ti/Pt/Au anodes UBFC-1, UBFC-2, UBFC-3 and Table 5.8 the DC characteristics for diodes of 2 μm and 3 μm.

A_d	30 μm		20 μm		15 μm	
Batch	η	R_s	η	R_s	η	R_s
UBFC_1_diode1	1.15	7.9	1.09	8.4	1.14	8.4
UBFC_1_diode2	1.14	6.7	1.12	6.5	1.12	9.1
UBFC_2_diode1	1.12	4.6	1.12	5.3	1.12	6.8
UBFC_2_diode2	1.12	9	1.12	7.9	1.13	8.2
UBFC_3_diode1	1.17	4.8	1.15	5.7	1.15	7.3
UBFC_3_diode2	1.17	5.7	1.07	6.2	1.13	5.9

Table 5.6 Showing diode ideality, series resistance for diode different batches.

A_d	3 μm	2 μm
I (mA)	*V (mV)*	*V(mV)*
1	*750*	*593*
0.1	*665*	*667*
0.01	*592*	*749*
0.001	*523*	*877*
η (ideality)	*1.17*	*1.25*
R_s	*18*	*20.1*

Table 5.7 Showing diode ideality, series resistance for two finish devices.

Conclusion on e-beam evaporated anodes:

The e-beam evaporated Schottky diodes process has proved to be successful for the fabrication of high quality devices. The result is a repeatable process with a yield close to 100 % and with the added advantage of enhanced thermal stability. The repeatability could be improved by dedicating an e-beam evaporator on only anode formation. Unfortunately in a University research facility this was impossible to implement and a lot of tests had to be perform before getting reproducible results.

This process was used during the development and fabrication of the integrated membrane diode describe in chapter 7.

5.3 Final process scheme for flip-chip diodes

5.3.1 Mask Design

The photomask used for the flip-chip diodes fabrication was designed using CAD software packages. Four layers are necessary for the different fabrication steps. Fig. 5.5 presents the mask layout.

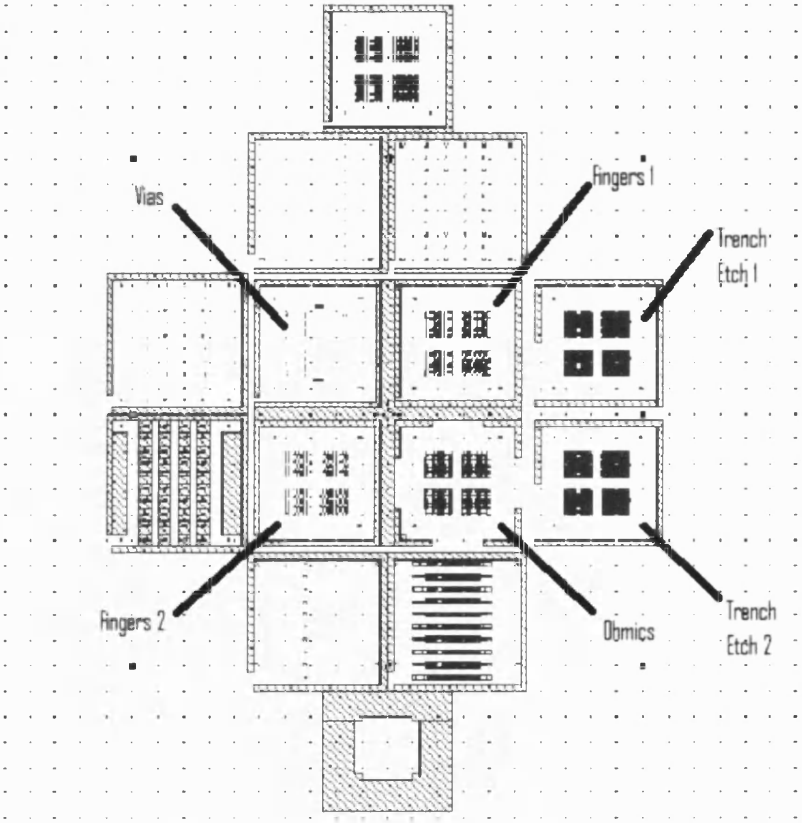

Fig. 5.5 Mask Layout for the fabrication of flip-chip diodes.

The ohmic pads and anode vias of 1 μm, 2 μm and 4 μm are present in the mask design. Two different finger lengths 15 μm and 20 μm have been chosen to allow comparison of the inductance between these different lengths. Two different trench etch masks are present and used during the wet etch of the air-bridge.

5.3.2 Final process fabrication Scheme

In this section the final fabrication process is presented. Each step will be covered in detail to describe the development and study which has been required. The wafer

layer structure used in final device processing included (from bottom up); semi-insulating GaAs substrate 550 μm, 1 μm Al (0.6) Ga (0.4) As etch stop layer, 4 μm highly doped ($4x10^{18}$ cm^{-3}) n^+ GaAs layer, 0.3 μm low doped ($4x10^{17}$ cm^{-3}) n GaAs layer and capped with a 0.25 μm SiO_2 electrically insulating layer (see Fig. 5.6).

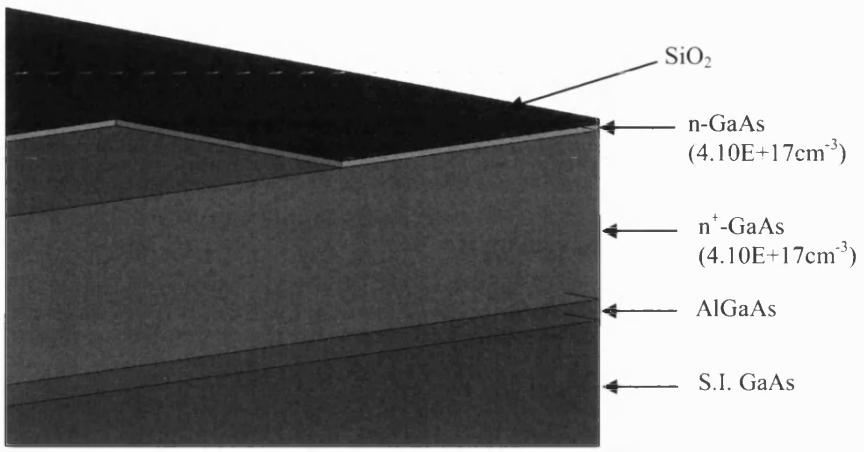

Fig. 5.6 Layers on GaAs wafer.

Step 1: The [100] GaAs wafer is cut in chips with a dimension of 10x11 mm using a diamond scribe. In step 6 a wet etch is necessary to undercut under the fingers and create the air-bridge. Therefore the diode fingers were aligned perpendicular to the [110] GaAs crystal direction to give the correct undercut profile. The orientation is referenced by using the length difference (see Fig. 5.7).

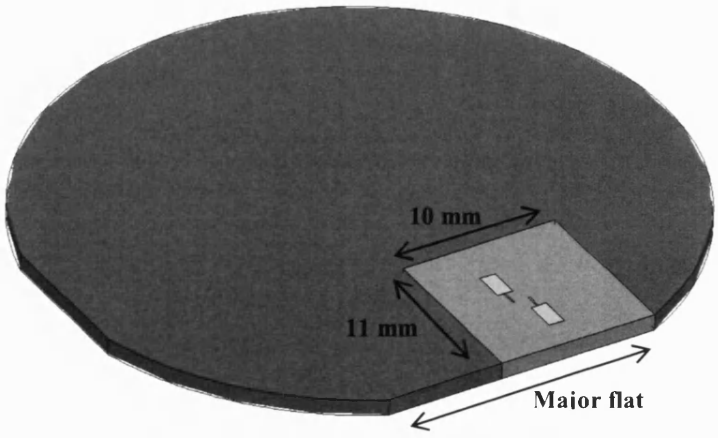

Fig. 5.7 Orientation of finger for on [100] GaAs wafer.

Step 2: The sample is then cleaned with the following procedure:

- - Sample soak in trichloroethane under ultrasonic agitation for 5min

- - Sample soak in acetone under ultrasonic agitation for 5 min
- - Sample soak in isopropyl-alcohol (IPA) under ultrasonic agitation for 5 min
- - Dehydrate bake on hot plate at 180 °C for 15 min

Step 3: The sample is patterned to defined the ohmic pads with the following procedure:

- HMDS spin at 3000 rpm for 30 sec.
- AZ1813 spin at 3000 rpm for 30 sec.
- Bake for 1 min on hot plate at 115 °C.
- Expose edge bead removal patterns for 1 min.
- Develop in AZ351 for 1 min.
- Expose ohmic contact patterns.
- Develop in AZ351 for 50-60 sec.
- Post Bake for 2 min on hot plate at 90 °C.
- Wet etch SiO_2 in 5:1 Buffered Oxide Etch, Typical etch rate 3 nm/sec.
- GaAs oxide etch in HCl/H_2O_2 (1:1) for 20 sec., rinse in H_2O for 20 sec.
- Etch through n- layer in $H_2SO_4/H_2O_2/ H_2O_2$ (1:8:100), typical etch rate 250 nm/min
- GaAs oxide etch in HCl/H_2O_2 (1:1) for 20 sec, rinse in H_2O for 20sec.
- Immediately after drying, load into Thermal evaporator.
- Deposit Ge/Au/Ti/Au 25/52/20/250 nm.
- Lift-off in acetone.
- Anneal ohmic contact metal layers at 405 °C for 6 min in H_2/N_2 forming gas.

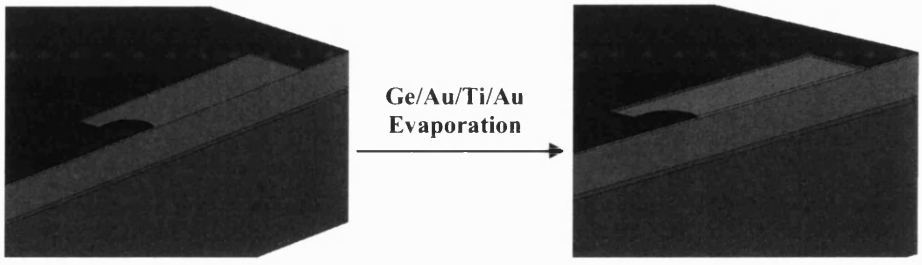

Fig. 5.8 SiO_2 and GaAs wet etch followed with Ohmic metal evaporation.

Fig 5.8 presents the process to remove the silicon dioxide in the ohmic pads region, etch the low doped n-GaAs to access the highly doped n^+-GaAs and evaporate ohmic

contact material. The GaAs oxide etch between the silicon dioxide etch and GaAs etch, was implemented to improve the homogeneity during GaAs wet etching. It was found that GaAs oxide could form on the surface while drying with N_2. Not applying a GaAs oxide etch always resulted in poor homogeneity after a GaAs wet etch. Material deposited onto a substrate was done using an Edwards 306 thermal evaporator. After lift-off, the ohmic contact was made by alloying germanium and gold using an in house rapid annealer. The annealing was performed in a H_2N_2 environment to avoid oxide formation. Fig. 5.9 illustrates the temperature profile used.

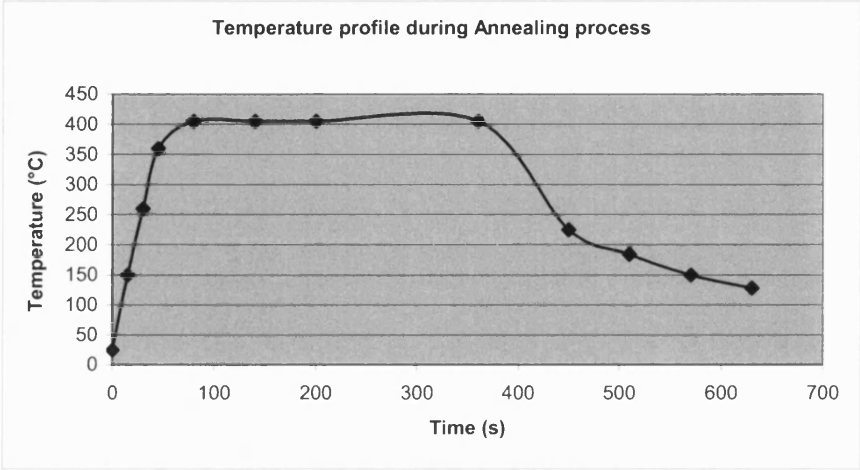

Fig. 5.9 Temperature profile during ohmic contact annealing.

Step 4: Anodes are patterned in Shipley AZ1813 resist and a HF wet etch of SiO_2 is performed to open the anode holes to the n-GaAs surface. Fig. 5.10 presents these process steps. Titanium, platinum and gold are deposited with the Edwards e-beam evaporator with the respective deposition rate of 1.1 nm/s, 0.3 nm/s, 1 nm/s. Fig. 5.10 indicates this step. The cleaning procedure described in step 2 is repeated before spinning the resist.

- HMDS spin at 3000 rpm for 30 sec.
- AZ1813 spin at 3000 rpm for 30 sec.
- Bake for 1 min on hot plate at 115 °C.
- Expose edge bead removal patterns for 1 min.
- Develop in AZ351 for 1 min.
- Expose anode patterns.
- Develop in AZ351 for 50-60 sec.

- Wet etch SiO2 in 5:1 Buffered Oxide Etch; typical etch rate 3 nm/sec.
- GaAs oxide etch in HCl/H_2O_2 (1:1) for 20 sec., rinse in H_2O for 20 sec
- Immediately after drying, load into e-beam evaporator.
- Deposit Ti/Pt/Au with the respective thickness of 60/20/100 nm.
- Lift-off in acetone.

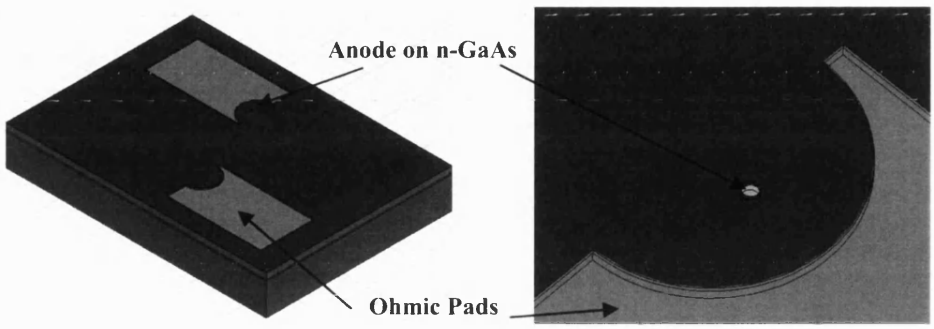

Fig. 5.10 Wet etching of SiO_2 to open contact on n-GaAs.

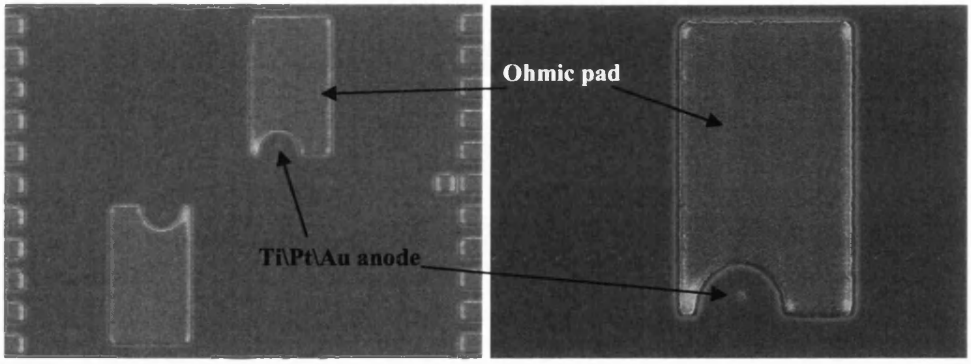

Fig. 5.11 SEM pictures of e-beam evaporated Ti\Pt\Au anode.

The post bake at 90 °C was found to be enough to damage the 1 μm size anode by collapsing the resist, resulting in no via in SiO_2.

Step 5: Fingers and pads are evaporated using Edwards 306 thermal evaporator. 20 nm of titanium and 1 μm of gold are deposited on the SiO_2 and on the anodes. Fig. 5.12 presents these process steps. The cleaning procedure described in step 2 is repeated before spinning the resist.

- AZ1813 spin at 3000 rpm for 30 sec.
- Bake for 1 min on hot plate at 115 °C.
- Expose edge bead removal patterns for 1 min.

- Develop in AZ351 for 1 min.
- Expose finger and pad contact patterns.
- Develop in AZ351 for 50-60 sec.
- Ti\Au evaporation.

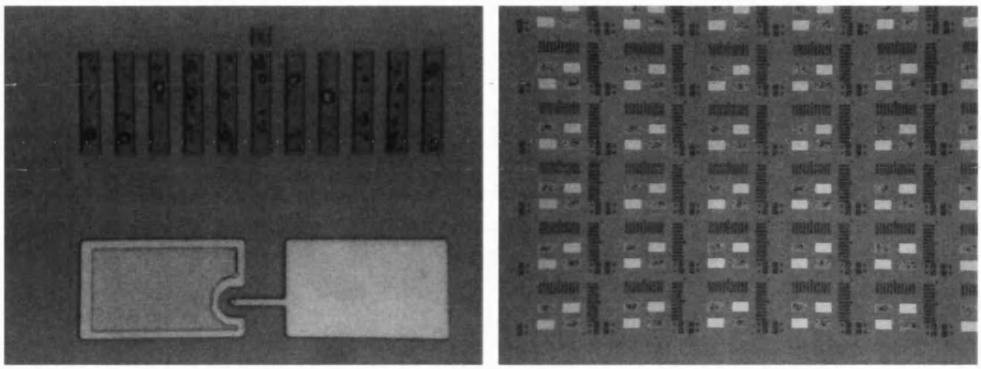

Fig. 5.12 Photograph of devices after Ti\Au deposition to define anode and ohmic pads.

Step 6: In this step the n-GaAs and n^+-GaAs are etched in order to isolate the individual devices. After protecting the pads and anode regions with resist, a BOE is applied to remove the SiO_2 around the pads and fingers before etching the GaAs. Fig. 5.13 presents these process steps. The cleaning procedure described in step 2 is repeated before spinning the resist.

- HMDS spin at 3000 rpm for 30 sec.
- AZ1813 spin at 3000 rpm for 30 sec.
- Bake for 1 min on hot plate at 115 °C.
- Expose edge bead removal patterns for 1 min.
- Develop in AZ351 for 1 min.
- Expose protection patterns.
- Develop in AZ351 for 50-60 sec.
- Post bake for 2 min on hot plate at 90 °C.
- Wet etch SiO_2 in 5:1 Buffered Oxide Etch.
- GaAs oxide etch in HCl/H_2O_2 (1:1) for 20 sec., rinse in H_2O for 20sec
- GaAs Etch in $H_2SO_4/H_2O_2/ H_2O_2$ (1:8:100). Typical etch rate 4.2 nm/sec

For this GaAs wet etch, extra care had to be taken to avoid under-etching the Schottky contacts by over etching. This etch was control by measuring the resistance between two adjacent contacts. The current path would favour that through the n^+-

GaAs layer rather than the diodes if the air channel had not etched. The resistance would start at a few ohms (corresponding to the ohmic contact resistance) to open circuit. After achieving this open circuit, the pad to pad capacitance was then measured.

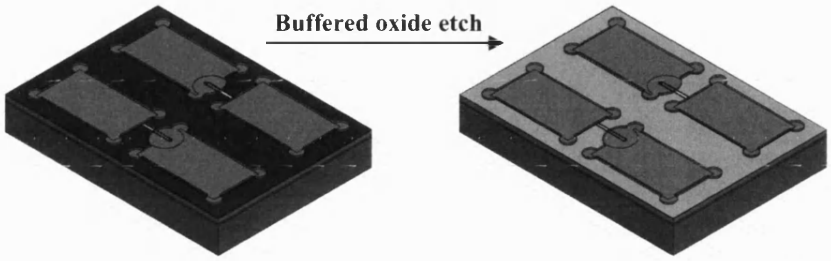

(a) (b)

Fig. 5.13 Design of device showing resist protection and (b) device after BOE.

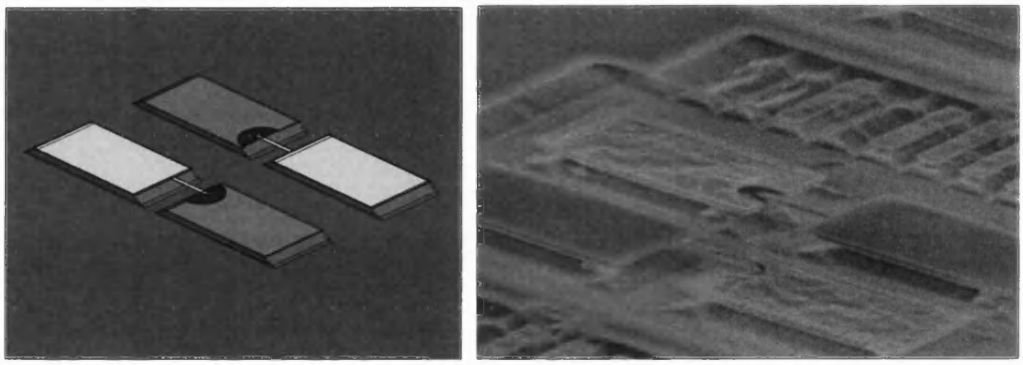

(a) **(b)**

Fig. 5.14 Design of anti-parallel Schottky diode after air-bridge etch and (b) SEM photograph of a completed device.

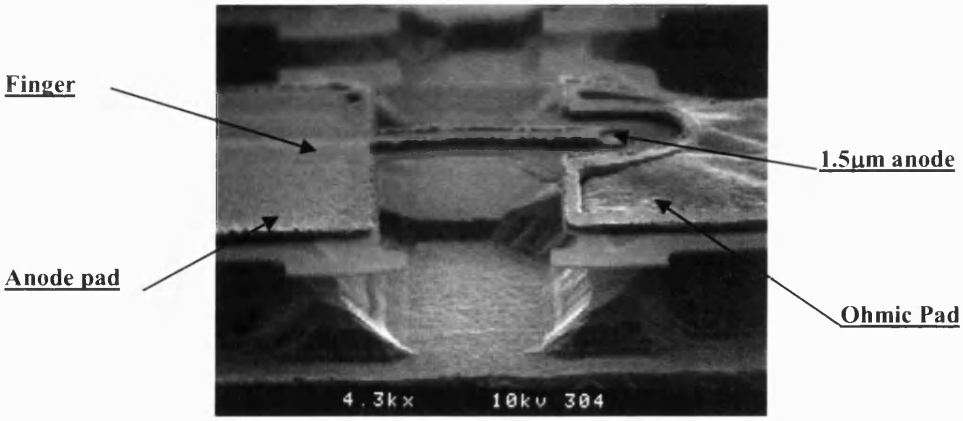

Fig. 5.15 SEM photograph of air-bridge Schottky diode.

Step 7: After finishing the air-bridge each device was characterised. Chapter 7 reviews these measurements. The sample was then prepared to be thinned and diced into individual chips. The devices were thinned down to a thickness of 15 μm. The sample was first mounted on a silicon carrier. Using a dicing saw the sample was diced to separate each chip to a depth of 50 μm. Fig. 5.16 (a) presents the chip before being diced and Fig 5.16 (b) the sample diced. After this step the sample was mounted upside-down on a silicon carrier. Using the same dicing saw, the sample was thinned down from the back until the 50 μm trench could be seen (Fig. 5.17). The sample was then re-measured to verify the thickness and the remaining GaAs thinned down to achieve a 15 μm thinned device. The chips were then separated and cleaned with acetone and iso-propanol. It was found that the fingers were not damaged after the thinning step.

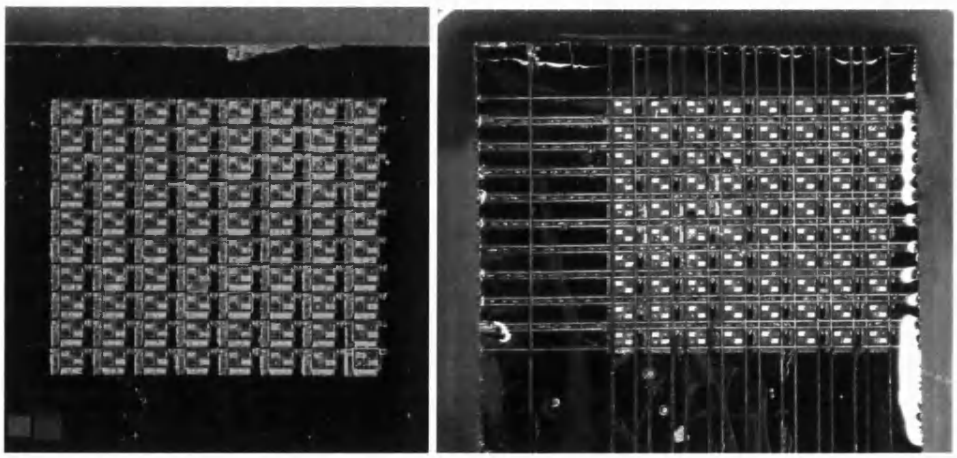

(a) **(b)**

Fig. 5.16 (a) Photograph of device before being diced. (b) photograph of device being diced to thickness of 50 μm.

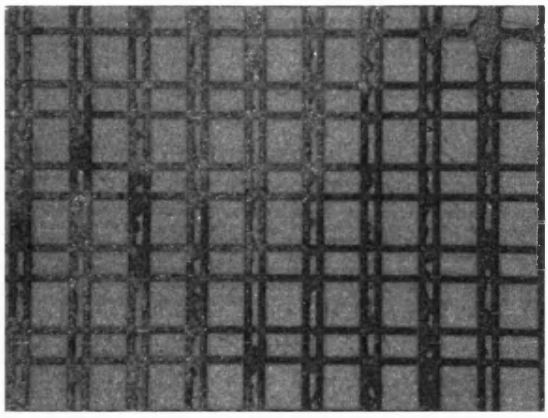

Fig. 5.17 Photograph of device from the back after being diced to a thickness of 15 μm.

References – Chapter 5

[5.1] C. J. M. Smith, S. K. Murad, *et al.*, "Use of polymethylmethacrylate as an initial pattern transfer layer in fluorine- and clhorine-based reactive ion etching", *J. of Vacuum Science & Technology B*, p113-117, January 1999.

[5.2] J. M. Miranda, C.-I. Lin, M. Brandt, M. Rodriguez-Girones, H. L. Hartnagel and J. L. Sebastian, "Influence of reactive ion etching on the microwave trap noise generated in Pt/n-GaAs Schottky diode interfaces", *IEEE Electron Device Letters*, Vol. 21, pp. 515-517, November 2000.

[5.3] Q. P. Pham, W. M. Kelly, and J. O'Brien, "Noise reduction in sputtered W/GaAs Schottky junctions," *Int. J. of IR and MM waves*, vol. 12, pp. 1079-1085, 1991.

[5.4] R. Williams, "Modern GaAs processing methods," Artech House, Inc. 1990.

[5.5] F. A. Perez, A. Singh, G. Aroca, "High temperature I-V characteristics of the as-deposited and thermally annealed W/n-GaAs Schottky junctions fabricated by RF sputtering," Devices, Circuits and Systems, *Proceedings of the 1998 Second IEEE International Caracas Conference*, 2-4 March 1998, pp. 79-82.

[5.6] A.K. Sinha, J.M. Poate, "Effect of alloying behaviour on the electrical characteristics of n-GaAs Schottky diode mettallized with W, Au and Pt", *Appl. Phys. Lett.*, vol 23, p.666, 1973.

[5.7] N-J. Wu, T. Hashizume and H. Hasegawa, "Formation of oxide-free nearly ideal Pt/GaAs Schottky barriers by novel in situ photopulse-assisted electrochemical process", *Jpn. J. Appl. Phys.*, Vol. 32, p. 2626-2631, June 1993.

[5.8] S. T. G. Wootton, "An integrated micromachined 1.6 Thz Schottky diode mixer", PhD Thesis, University of Bath, 1998.

[5.9] R.E. Muller *et al.*, "Electron beam lithography for the fabrication of air-bridged, submicron Schottky collectors," *J. Vac. Sci. Technol.*, Nov/Dec 1994.

[5.10] T.-H. Lee *et al.*, "A novel biased anti-parallel diode structure for subharmonic mixing", *IEEE Microwave Guided Wave Lett.*, vol. 4, pp. 341-343, Oct. 1994.

[5.11] A. E. Geissburger, I. J. Bahl *et al.*, "A new refractory self-aligned gate technology for microwave power FET's and MMICs," *IEEE Trans. Electron Devices,* vol. 35, pp. 615-622, May 1988.

[5.12] C. A. St. Jean, *et al.*, " Novel fabrication of Ti-Pt-Au/GaAs Schottky diodes," *IEEE Transactions on Electron Devices*, vol. 47, no. 7, pp. 1456-1468, July 2000.

Chapter 6

Integrated Membrane Mixer Fabrication

6.1 Bath membrane mixer diode

After developing the planar Schottky diode fabrication process, the next step was to extend the process to integrate the diode and the RF circuit on a GaAs membrane creating a monolithic device. The fabrication of the membrane mixer is presented in this section. Different approaches were investigated to fabricate the membrane. The advantages and difficulties encountered with each method are presented. Two different types of gas: $SiCl_4$ and Cl_2 have been used and studied for the GaAs dry etch process.

6.1.1 Mask Design

The photomask used for the integrated membrane mixer was designed using CAD software packages. Seven masks are necessary for the different fabrication steps. Fig. 6.1 presents the mask layout.

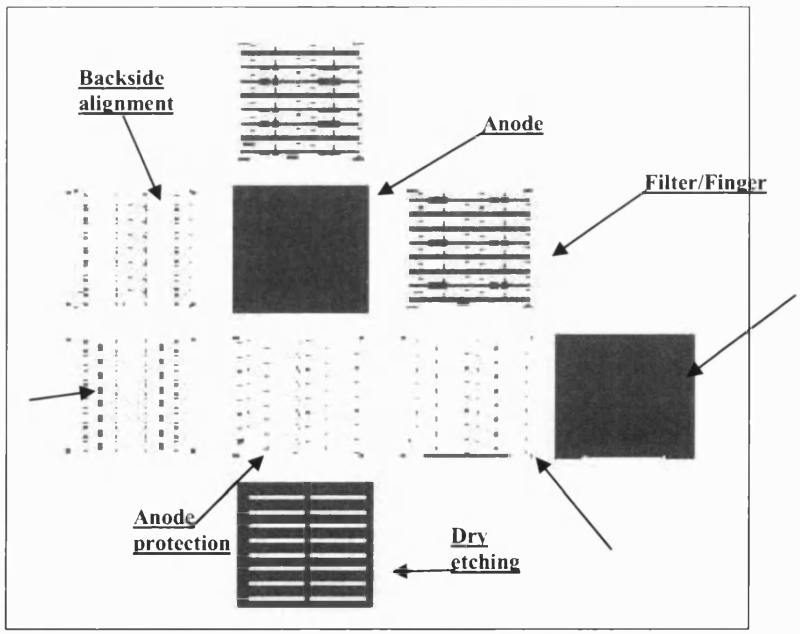

Fig. 6.1 Mask Layout for the fabrication of membrane mixer.

Mask definition:

Ohmic: Layer defining the ohmic contacts on the GaAs.

Anode: Layer defining the 1 to 3 μm anode.

Filter/Finger: Layer defining the low-pass and band-pass RF filter and diode fingers.

Anode protection: Layer protecting the anode during air-bridge wet etching.

Backside alignment: Opening to open backside alignment opening

Membrane: Opening to thin down area under diode, align using backside alignment

Dry etching: Layer protecting the device during deep dry-etch.

6.1.2 Final process for Bath membrane mixer

The wafer layer structure used in the membrane device fabrication was similar to that used for the planar Schottky diode, previously shown in Fig 5.6: [100] SI GaAs substrate 550 μm thick, 1 μm Al (0.6) Ga (0.4) As etch stop layer, 4 μm highly doped ($4x10^{18}$ cm^{-3}) n^+ GaAs layer, 0.3 μm low doped ($4x10^{17}$ cm^{-3}) n GaAs layer and capped with a 0.25 μm SiO_2 electrically insulating layer.

The GaAs wafer was cut into 18x12 mm samples using a diamond scribe. The diode fingers were once more aligned perpendicular to the [110] GaAs crystal direction to give the correct undercut profile. The process to fabricate the Schottky diodes was kept the same as that described in Chapter 5. For the membrane devices, the filter and contact fingers were defined at the same time (Fig. 6.2 (c)). Following this step the air-bridge was etched and the filters were defined in the n/n^+ GaAs layer (Fig. 6.2 (d)). The sample was then coated with a 6 μm thick Microposit 220 photoresist to allow long dry etching. The GaAs around the device circuits was etched to a depth of 50 μm below the front surface using RIE in the Plasmalab 80. The sample was then front-side mounted parallel to a glass carrier on a hotplate (140 °C) using Crystal Bond glue. The planarity of the device was checked at room temperature before the lapping process. The lapping process was performed using a Logitech PM5 grinding/ polishing jig and grinding was performed on a glass plate using an alumina solution seeded with 3 μm particles. The sample was lapped down, until the device outlines were visible. The individual mixer circuits were then carefully removed and rinsed in acetone and IPA.

The membrane fabrication steps are presented in Fig. 6.2.

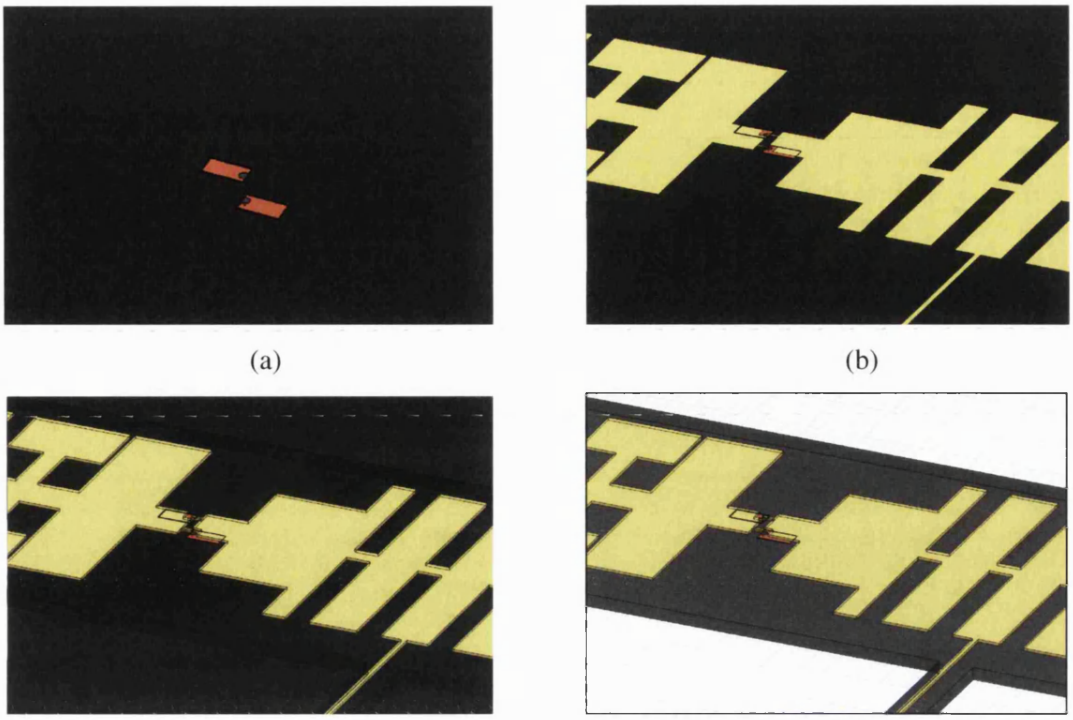

Fig. 6.2 (a) Ohmic and anode fabricated as described in chapter 5; (b) finger and filter defined and evaporated at the same time; (c) device after 50 µm dry etch; (d) sample after lap down.

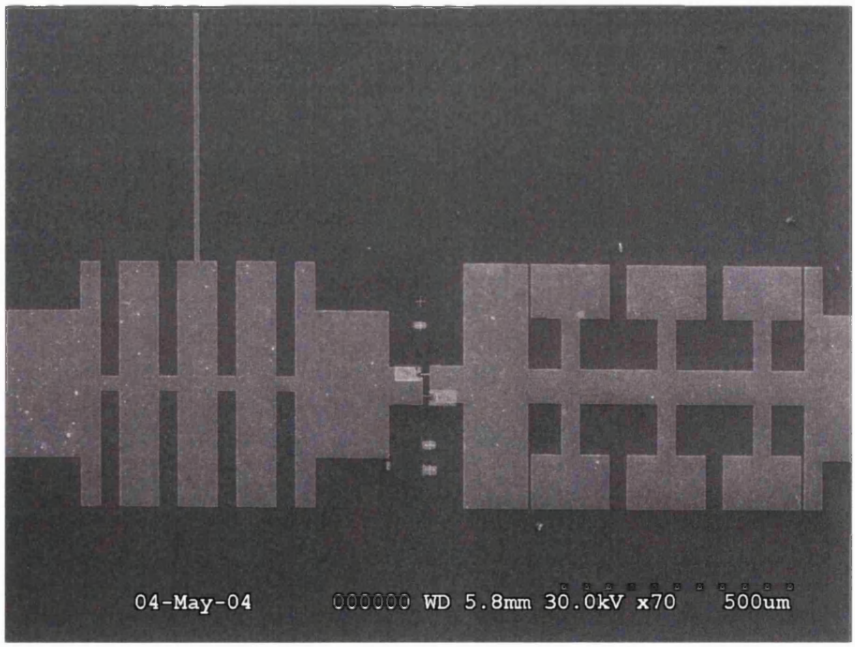

Fig. 6.3 SEM photograph of membrane device before air-bridge etch.

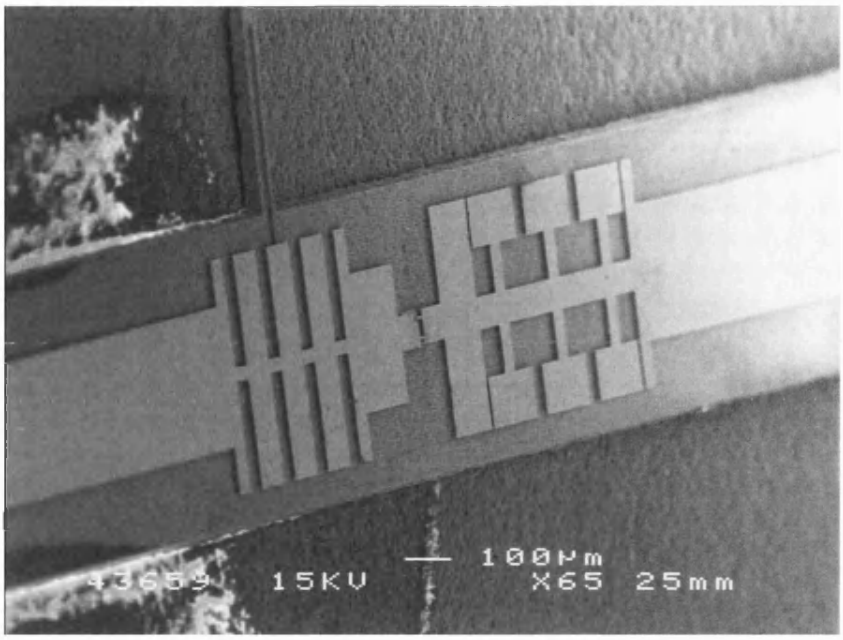

Fig. 6.4 SEM photograph of membrane device after lap down.

6.1.3 GaAs dry etch process

The GaAs dry etch process was developed in the nanofabrication facilities during this project. The requirements for this process were to achieve a deep dry etching 30 to 50 μm deep, fast etch rate, smooth surface profile and good selectivity with metal or photoresist masks.

Initial dry etching was carried out using chlorine and argon gases which resulted in very rough surfaces as shown in the SEM photograph in Fig. 6.5.

The problem was alleviated when $SiCl_4$ was used in place of chlorine in the RIE chamber. The $SiCl_4$ process was optimised by varying the chamber pressure, RF power, $SiCl_4$ and Ar flow.

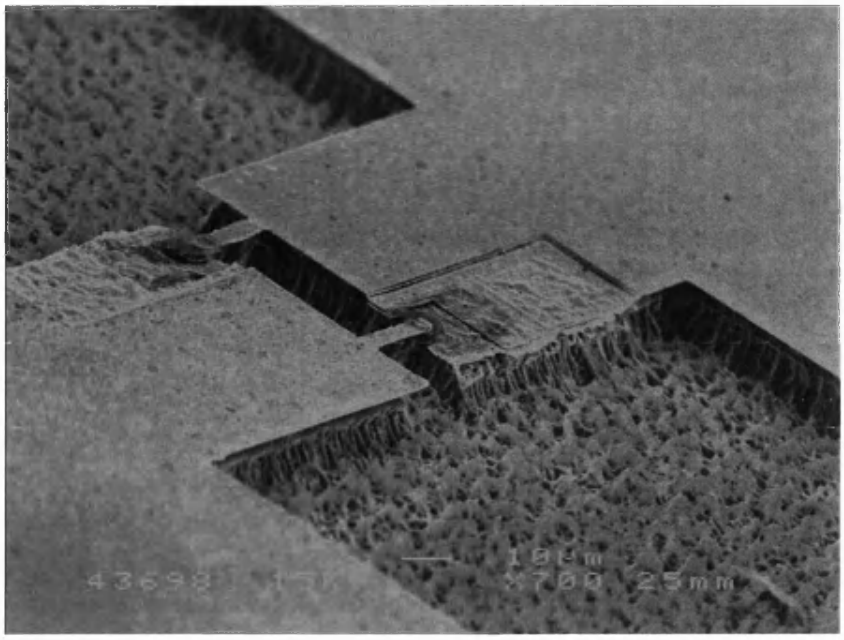

Fig. 6.5 SEM photograph of very poor dry etched surface using chlorine and argon gases.

The process parameters for the GaAs deep etch were: 10mTorr chamber pressure; 100 Watt RF power; 16 sccm $SiCl_4$; 4 sccm Ar.

The etch rate for this process was found to be around 0.4 μm/min and the selectivity to Microposit 220 photoresist 30:1. 125 minutes were needed to etch 50 μm of GaAs. To avoid excessive heat in the chamber, the etches were performed for 40 min and stopped for 30min to allow the chamber to cool down.

This resulted in a smooth mirror finish to the etched surface and vertical sidewalls (Fig. 6.6 and Fig. 6.7).

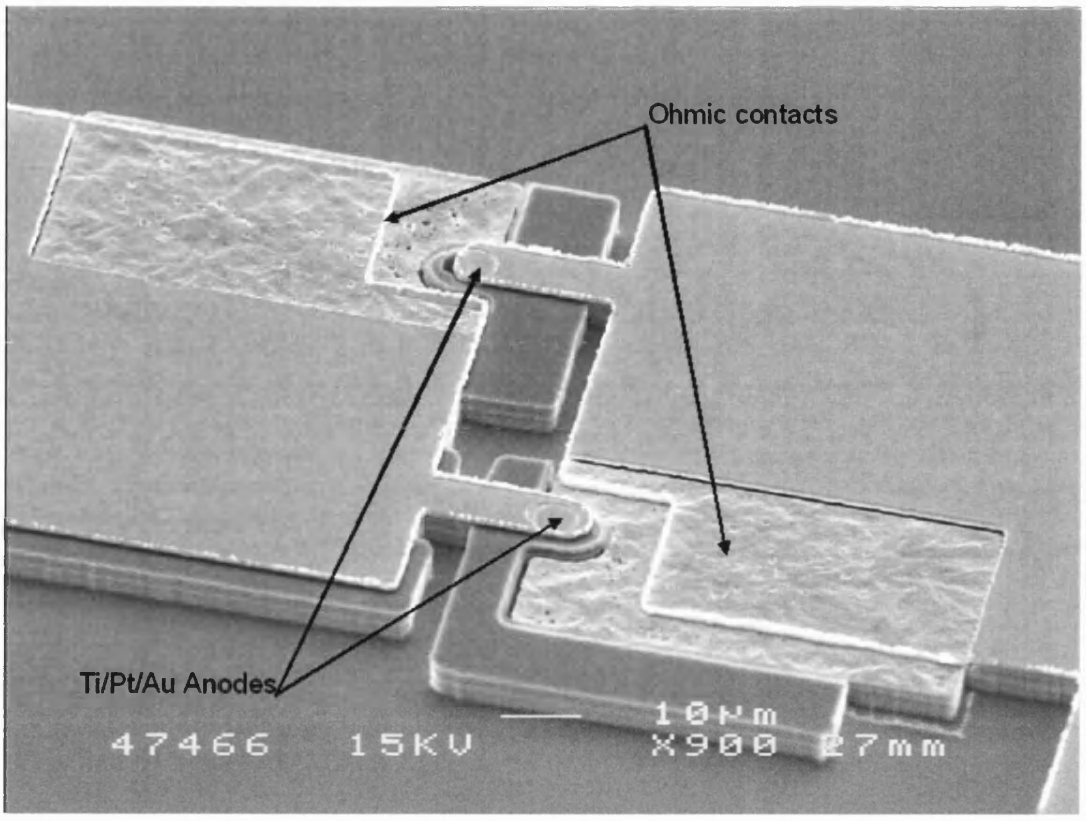

Fig. 6.6 SEM photograph of a 6 μm dry etch to remove the n and n^+ GaAs layer.

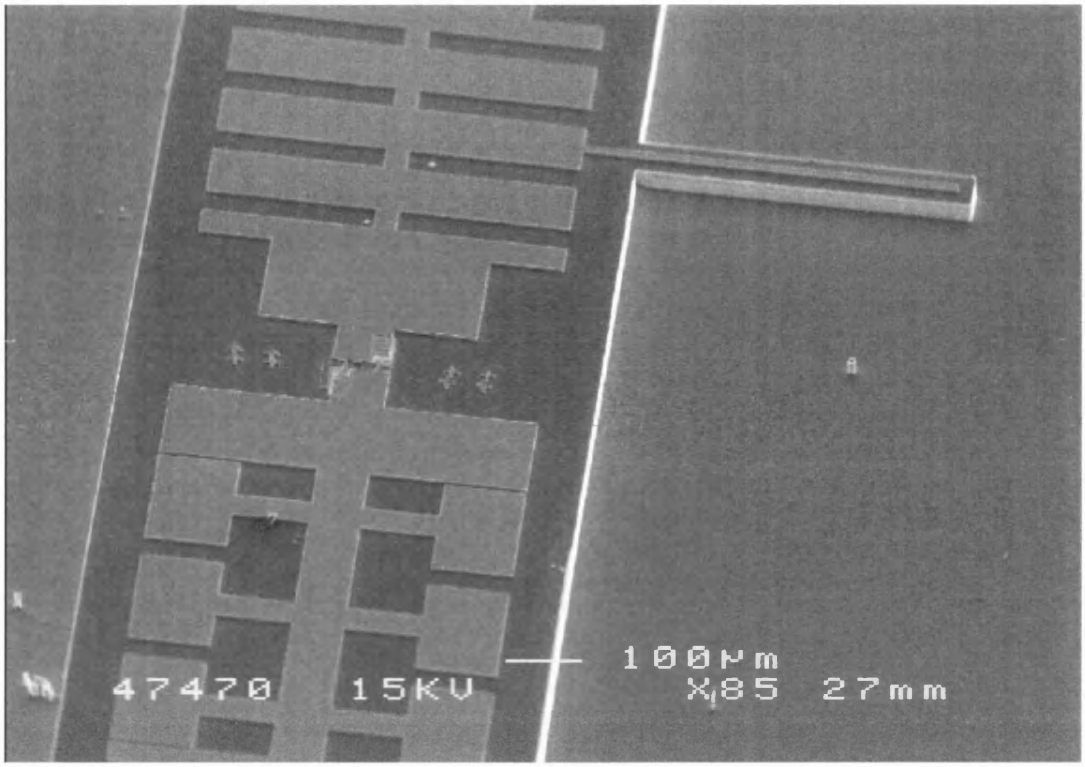

Fig. 6.7 SEM photograph of a 50 µm dry etched surface using $SiCl_4$ and argon gases.

6.2 Bath-RAL-ODP membrane mixer diode

This project aimed to fabricate a fixed-tuned membrane mixer using the Schottky diode process developed at the University of Bath with state-of-the-art simulation and design performed by the University of Paris and the mixer-block designed and fabricated by the Rutherford Appleton Laboratory.

The fabrication scheme from the first membrane mixer presented in section 6.1 was re-evaluated for this mixer design. The filter metallisation was deposited directly onto the semi insulating GaAs to avoid any parasitic modes propagating in the doped GaAs. Anisotropic chemical etching was used to produce a sloping profile of the GaAs between the filter plane and the top of the device mesa to allow a continuous layer of metallisation connecting both regions

The following section presents the mask design and the final process used to fabricate the membrane mixer.

6.2.1 Mask Design

The photomask used for the integrated membrane mixer was design using CAD software packages. Seven masks are necessary for the different fabrication steps. Fig. 6.8 presents the mask layout.

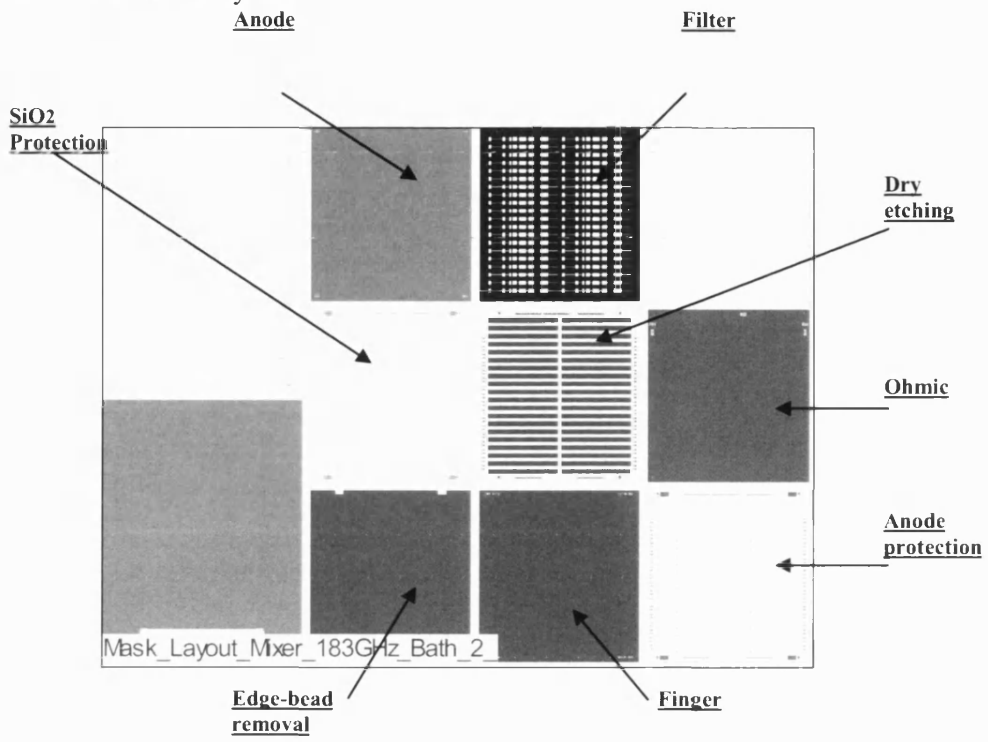

Fig. 6.8 Mask Layout for the fabrication of Integrated Mixer.

Mask definition:

Ohmic: Layer defining the ohmic contacts on the GaAs.

Anode: Layer defining the 1 to 3 μm anode.

Finger: Layer defining the diode fingers.

SiO_2 protection: Layer protecting the diode SiO_2 during HF wet etching.

Anode Protection: Layer protecting the anode during air-bridge wet etching.

Filter: Layer defining the RF filters.

Dry etching: Layer protecting the device during deep dry-etch.

6.2.2 Final process for Bath-RAL-ODP membrane mixer

The rest of this section is devoted to the fabrication schemes that were developed for the Bath-RAL-ODP membrane mixer. Concise notes describing the steps performed in reaching the sequence of illustrated stages accompany each processing diagram. For planar stages including ohmic and anode formation, complete processing details can be found in Chapter 5.

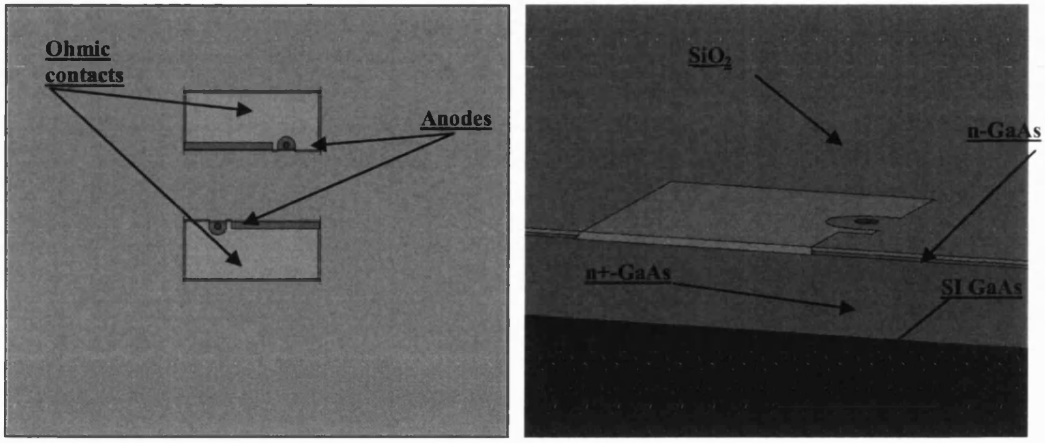

(a) (b)

Fig. 6.9 3D representation of ohmic contacts and anodes on GaAs

1. To form the ohmic contact, Ge/Au/Ti/Au is evaporated on the n^+-GaAs and annealed at 405 °C for 6 minutes (Fig. 6.9(a)).
2. Ti/Pt/Au is deposited using E-beam evaporation to form the anode (Fig. 6.9(b)).
3. Shipley S1813 resist was used to define finger mask and 1μm of Cr/Au is evaporated using thermal evaporator. The Ti was replace by Cr due to it lower melting point and ease to use with thermal evaporator.
4. Ohmic pads, anodes and fingers are protected using S1813 resist before wet etching the SiO2 (Fig. 6.10(a)).
5. The devices are air-bridged using GaAs wet etching (Fig. 6.10(d)). The GaAs wet etch creates slopes perpendicular to the pads which are used as electrical transitions between the mesa and the filters (Fig. 6.10(e) and Fig. 6.11).
6. A new liftoff photoresist mask is applied to define the RF filter circuit on the S.I GaAs. Cr/Au respectively 0.3 μm and 1 μm are deposited using the thermal evaporator.

7. Microposit 220-7.0 resist was used in the final deep dry etch around the device circuit. The resist was spin coated to a thickness of 5.5 μm which was adequate for such a long etch. The selectivity between the resist and GaAs in the $SiCl_4$ RIE environment was between 10:1 and 20:1 depending on power, gas throughput, argon levels and chamber pressure. The device circuits were etched down 45 μm around the device providing the membrane ready for lapping (Fig. 6.12).

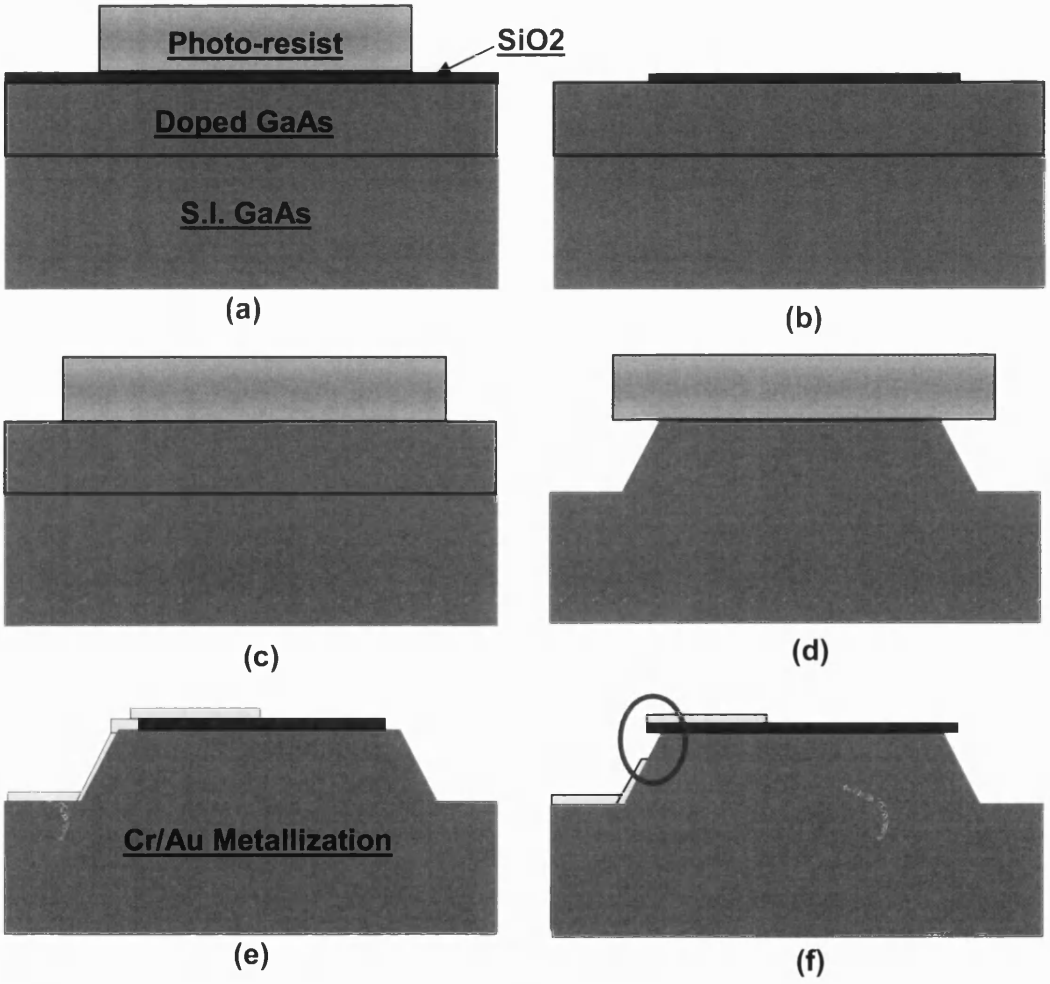

Fig. 6.10 Processing overview of steps 4 and 5 showing the various layers in the GaAs wafer.

To alleviate over hanging SiO_2 during GaAs wet etching due to under-etch, (Fig 6.10 (f)), two different masks are used for the SiO_2 etching and air-bridge etching. To avoid micro-masking, the under etch was characterised for our GaAs wafer and was found to be 0.02 μm/min.

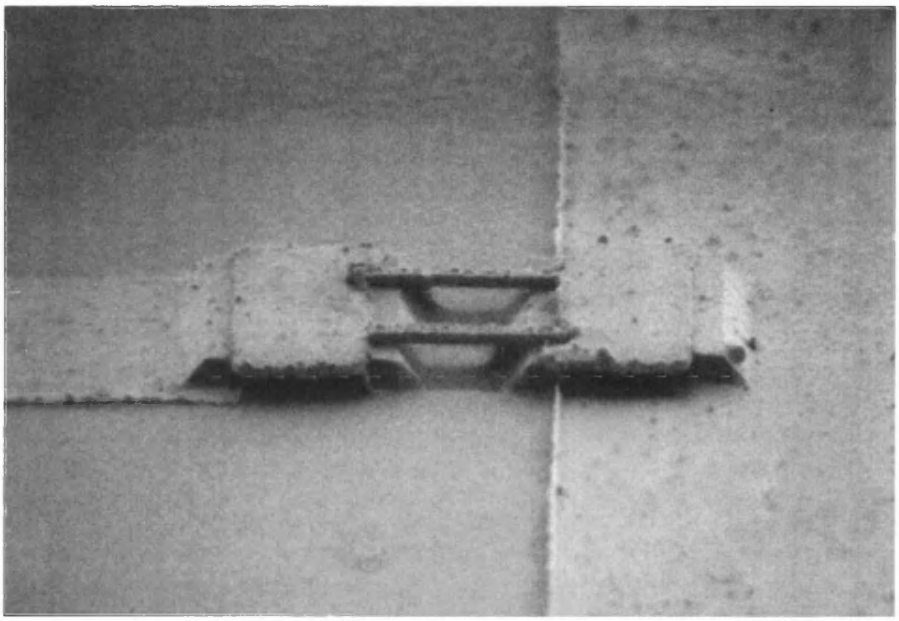

Fig. 6.11 SEM photograph of transition between SI GaAs and the Schottky diodes mesa.

8. With all top-side processing complete, the wafer sample was then front-side mounted parallel to a glass carrier using a robust Crystal Bond glue. The sample was then lapped down until the device outlines were visible. The integrated mixer circuits were then carefully removed by washing with acetone and isopropanol.

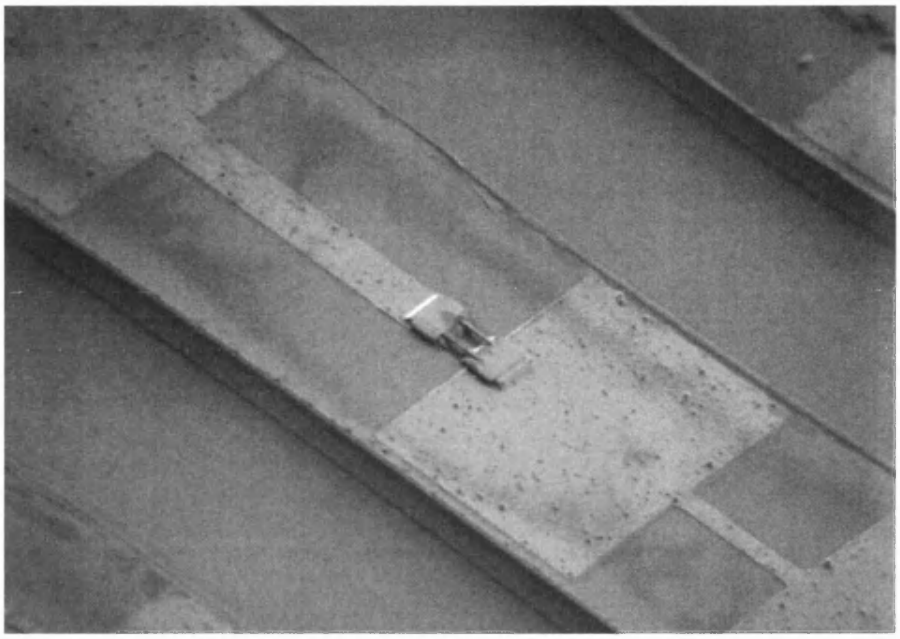

Fig. 6.12 SEM photograph of integrated mixer circuit after deep GaAs RIE etching.

This process gives a novel way to connect the RF filter located on the SI GaAs with the mesa structure without the use of air-bridges.

Chapter 7

Mixer Measurements

This chapter presents the DC and RF measurements of the best planar Schottky diodes produced during this project. The DC and RF performance are compared with the current research in the field. Furthermore, RF experimental setup and mixer performance results are given and evaluated against commercially available diodes.

7.1 Flip-Chip Diode Mixer Measurements

7.1.1 DC characterisation of Flip-Chip diodes

Fabrication of over 20 batches of diodes has been necessary to develop a reliable and high quality Schottky diode process. In order to acquire and store their data, an automated measurement system was developed under the LabView environment. The Agilent 4279A C-V meter, Keithley 220 current source and Keithley 617 electrometer were controlled through a GPIB interface. The Schottky diodes were tested on the probe station. Two micromanipulators with 5 μm gold tips were used to probe the devices.

Fig. 7.1 presents the LabView environment for the I-V measurements. Ten measurements were made for each device before being averaged. The ideality factor and the series resistance were then calculated.

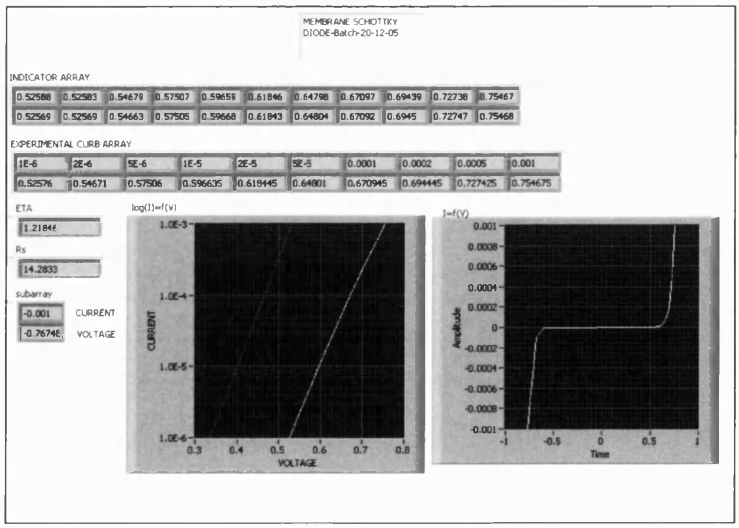

Fig. 7.1 LabView window for I-V measurements.

7.1.2 DC characteristics of final flip-chip device

One major issue occurred during the wet etching of the air-bridge: it was found that 25% of the diodes were under-etched in the anode region. This under-etch removes and damages the anode. Fig. 7.2 shows the under-etch issue. The problem comes from the weak adhesion between the SiO_2 and the GaAs. Table 7.1 presents the yield of one quarter of the flip-chip diode chip. In the Table 7.1, 1 represents a working diode and 0 an under-etched nonworking diode. Two diodes were present for the anti-parallel configuration diode1--diode2.

	Flip-Chip Devices							
	A	B	C	D	E	F	G	H
1	1--1	1--1	1—1	1--1	1--1	1--1	1—1	1--1
2	1--1	1--1	1—1	1--1	1--1	1--1	1—1	1--1
3	1--1	1--1	0—0	1--1	1--1	1--1	1—1	1--1
4	1--1	1--1	0—0	1--1	1--1	1--1	1—1	1--1
5	1--1	1--1	0—0	1--0	1--1	0--0	0—1	1--1
6	1--1	1--1	1—1	1--1	0--0	1--1	1—1	1--1
7	1--1	1--1	1—1	1--1	0--0	0--0	1—0	1--1
8	1--1	1--1	1—1	1--1	1--1	1--1	0—1	1--1
9	1--1	1--1	1—1	0--0	1--1	1--0	1—0	1--1
10	1--1	1--1	1—1	1--1	1--1	1--1	1—1	0--1

Table 7.1 Yield of flip-chip devices on a quarter sample.

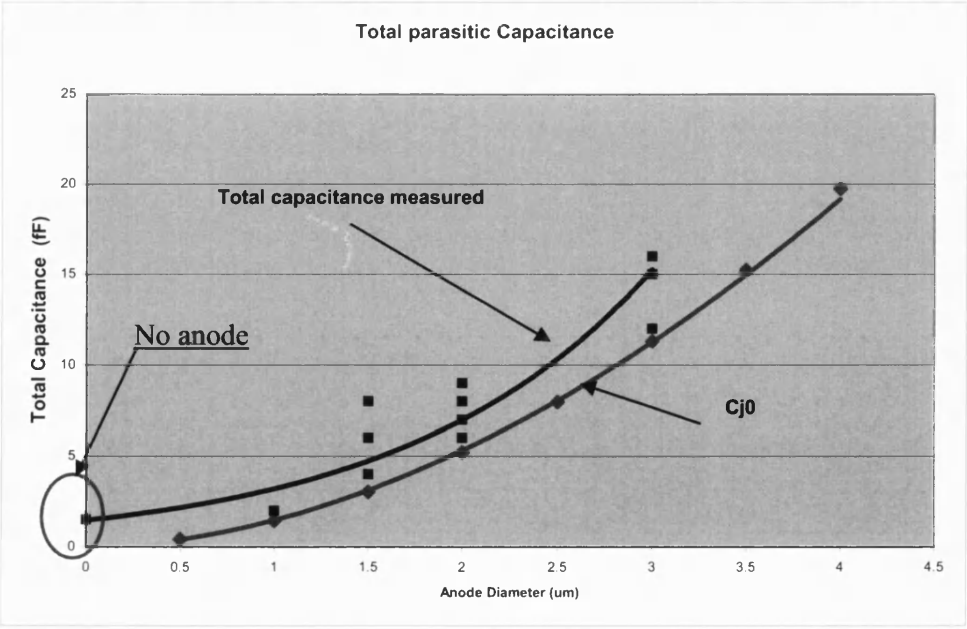

Fig. 7.2 Measured and simulated Capacitance.

This yield could be improved by implementing a 15 min post bake at 120 °C before the air-bridge etch [7.1]. Furthermore, a better control of the quality of the SiO_2 deposited could also lead to higher yield as it was found that weak adhesion was present between the SiO_2 and the GaAs.

Fig. 7.2 presents the total capacitance measured as a function of the anode diameter. A diode structure with no anode was also fabricated and a capacitance of 1.6 fF was measured. This value confirms the 3D EM modelling of the parasitic capacitance from section 4.1.2.

Table 7.2 gives a summary of the best performing diodes that were fabricated during this project. The device UBFC-G2 was used for mixing application which are presented in section 7.2. The left and right diodes represents each diode characteristics in the anti-parallel configuration.

Batch	A_d (μm)	t_e (μm)	N_d (cm-3)	Φ_b	η	R_s (Ω)	I (V)	C_{j0} (fF)	C_T (fF)
UBFC-A7_Diode1 Left	1.5	0.3	$4x10^{17}$	0.81	1.22	20.6	3.10^{-14}	1.86	5
UBFC-A7_Diode1 Right	1.5	0.3	$4x10^{17}$	0.83	1.21	17.7	$1.9.10^{-14}$	1.86	6
UBFC-G2_Diode1 Left	1.5	0.3	$4x10^{17}$	0.83	1.23	16.3	$3.9.10^{-14}$	1.86	4
UBFC-G2_Diode1 Right	1.5	0.3	$4x10^{17}$	0.83	1.23	19	$2.6.10^{-14}$	1.86	4

Table 7.2 Summary of state-of-the-art diode characteristics fabricated during this project.

Diode Type or Structure	A_d (μm)	t_e (μm)	η	R_s	C_{Total} (fF)	Ref.
Ti/Pt/Au	1	-	1.40	13.0	-	[7.2]
Ti/Au	0.9	-	1.13	10.0	-	[7.3]
Ti/Pt/Au	1.4	0.1	1.19	4.9	-	[7.4]
Ti/Pt/Au	6	0.4	1.12	4.6	-	[7.5]
Ti/Pt/Au	2	0.2	1.19	7	26	[7.6]
QVD	0.8	0.1	1.12	25	20	[7.7]
UVa-SD1T7-D20	0.8	-	1.3	14	6.5	[7.8]

Table 7.3 Comparing DC characteristics of some state-of-the-art Schottky diodes.

Table 7.3 shows DC diode characteristics for some state-of-the-art Schottky diodes produced using a similar processing technique by leading researchers in the field. The quality of the diodes produced in this project is comparable to those of leading research.

7.1.3 RF Measurements with RAL Mixer Design

The flip-chip diodes fabricated during this project have been tested at 190 GHz with the help of Dr. B.E.J. Alderman at the Rutherford Appleton Laboratory (RAL).

The mixer block used during the RF test was designed by Dr. Steve Marsh and fabricated at the RAL. The design is based on a fixed-tuned sub-harmonically pumped (SHP) mixer. The RF and LO waveguides have optimised fixed-tuned backshorts.

The diode is first flip-chip mounted on a 50 μm quartz substrate using PbSn solder. The quartz circuit consist of a microstrip RF and LO antenna, a low pass filter, band-pass filter and DC grounding. Fig. 7.3 presents the diode UBFC-G2 assembled on the quartz filter.

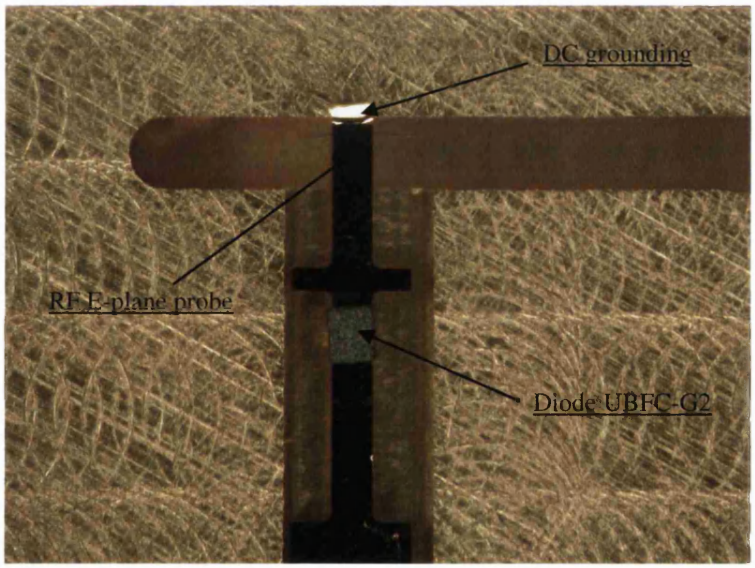

Fig. 7.3 Photograph of the UBFC-G2 diode flip-chip mounted onto quartz circuit.

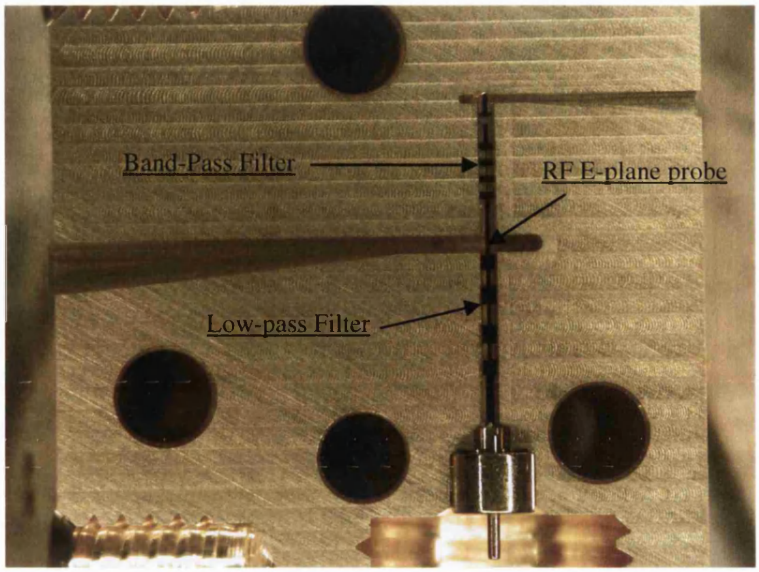

Fig. 7.4 Photograph of 190 GHz fixed-tuned SHP mixer.

The internal view of the fixed-tuned mixer is presented in fig. 7.4. The block includes a WR-10 LO waveguide and a WR-5 RF waveguide. Both waveguides were tapered to improve the impedance matching with the microstrip antenna. The DC grounding was done using a thin sheet of gold soldered to the filter metallisation on the quartz substrate, clamped between the two halves of the mixer block. The IF output was connected to an SMA connector with a 25 μm diameter gold wire. The gold wire was contacted using silver-loaded epoxy. Figure 7.5 presents the mixer block assembled with dowel pins.

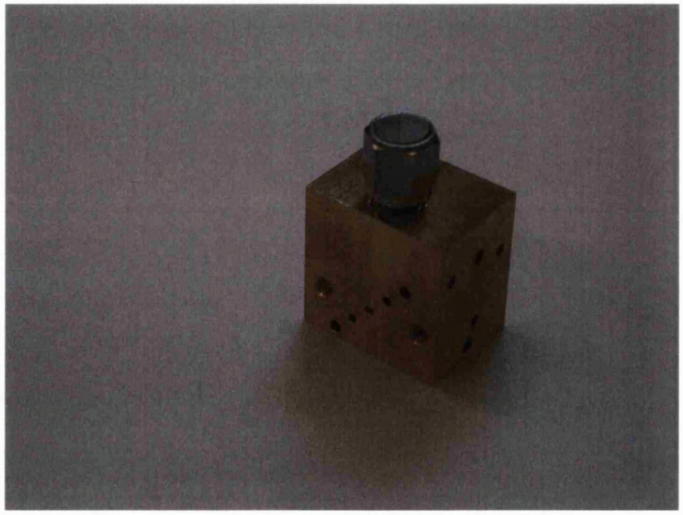

Fig. 7.5 Photograph of 190 GHz fixed-tuned SHP mixer.

The 190GHz SHP mixer has been tested at room temperature. Figure 7.6 presents the measurements setup. The RF signal was coupled into the mixer block with a WR-5 RF waveguide output which was connected to a Picket-Potter feed horn. The LO signal was provided by a mechanically tuneable Gunn oscillator. An attenuator was place between the mixer and the oscillator to control the power level. The power level for each frequency was calibrated using an Erickson power meter [7.9].

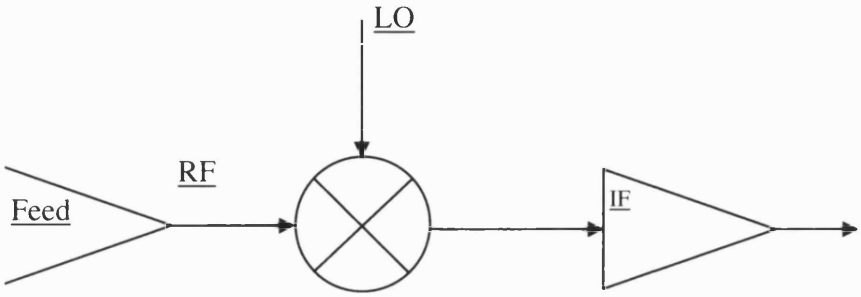

Fig. 7.6 Schematic of measurement test setup.

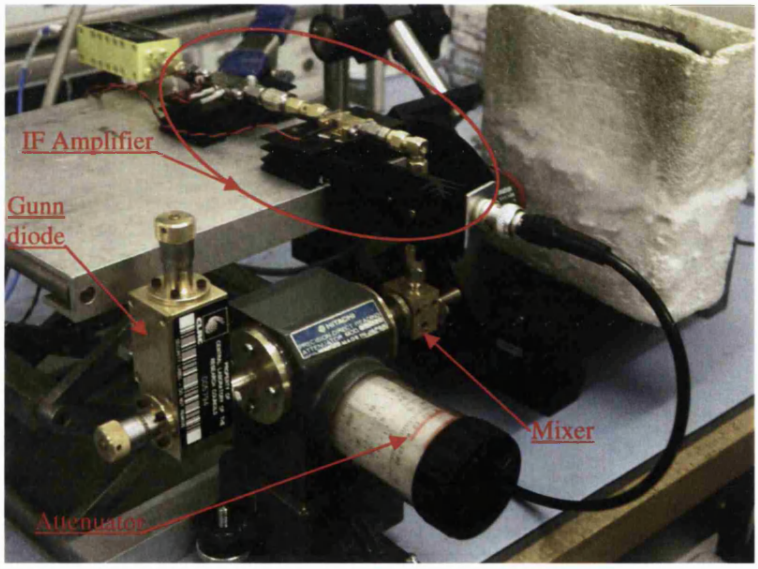

Fig. 7.7 Photograph of 190 GHz mixer measurements setup.

The system noise temperature was measured using the Y-factor method [7.10], alternating between room temperature and 77 K black-body loads.

The power ratio between the hot load and cold load allow the DSB noise temperature to be determined [7.11]:

$$T_r = \frac{T_h - Y\,T_c}{Y - 1} \tag{7.1}$$

where $Y = \frac{P_h}{P_c}$, T_r is the system noise temperature DSB in K, T_h is the effective temperature of the hot load (293 K, ambient laboratory temperature), T_r is the effective temperature of cold load (77 K, liquid nitrogen), P_h is the IF power measured in response to the ambient load and P_c the IF power measured in response to the cold load.

The IF powers were measured with a square law detector at an IF frequency of 3 GHz. The power was amplified with a series of three Miteq low-noise amplifiers, operated at room temperature with an IF bandwidth of 2GHz.
A plot of the system noise temperature versus frequency is shown in fig. 7.8.

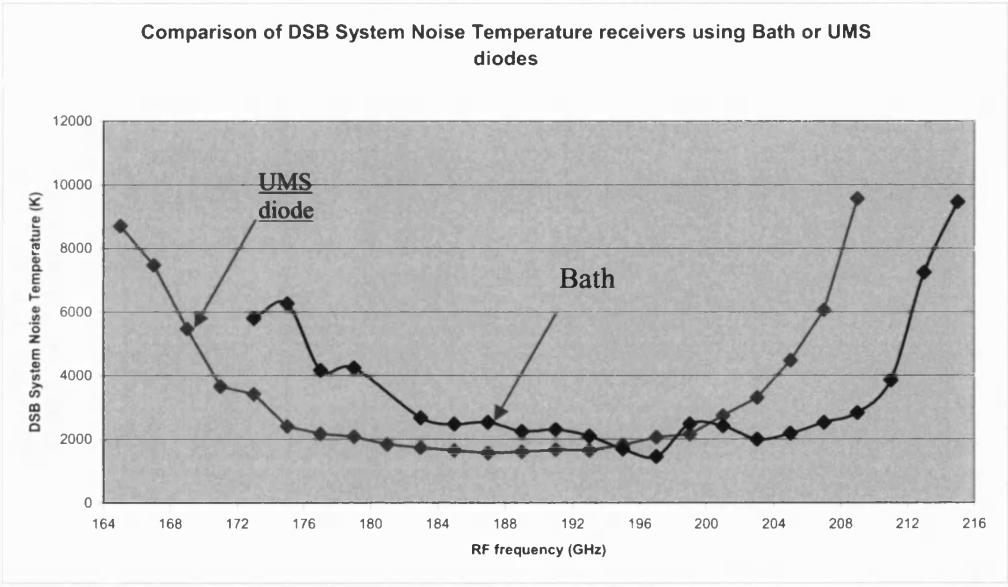

Fig. 7.8 190 GHz receiver results using Bath diode or UMS diode.

The best results achieved at 197 GHz were obtained using the UBFC-G2 diode. A system noise temperature of 1350 K DSB and a mixer conversion loss of 7.5dB DSB were measured using 5 mW LO power.
A commercial diode from United Monolithic Semiconductors (UMS) was also tested using a second similar block and RF circuit. This test provided the opportunity to compare the performance of the diodes fabricated during this project with commercially available diodes. Fig 7.8 presents the system noise temperature using UMS diodes. From the plot fig. 7.8 we can see that the noise temperature results for

both diodes are very similar in performance and bandwidth. The centre of frequency response for UBFC-G2 diode is shifted to around 196 GHz compared to 187 GHz for the UMS diode. This shift can be explained due to the mixer block design and the fixed backshorts, which were tuned to match the UMS diode impedance characteristics.

It is interesting to mention that the UMS diodes are not commercially available with antiparallel configuration. The diodes are fabricated in series and had to diced and put in an antiparallel configuration on the quartz substrate. This step requires time and specialised skills. Furthermore the commercial Schottky diode chips have a thickness of 100μm restricting the diode operation to 110GHz. For this reason the UMS diodes used in this mixer block were thinned down to a thickness of 30μm.

These measurements have demonstrated the ease of use and the excellent quality of the Schottky diodes fabricated during this project for applications in the sub-millimetre region. Following these results, the company Radiometer Physics GMBH (RPG) also tested a few diodes to establish future collaboration. RPG reported results of 950 K DSB system noise, 700 K mixer noise and 6 dB conversion loss at 150GHz. The diodes also proved to be robust and insensitive to large LO power.

7.2 Measurements on the integrated Subharmonic Mixer

The fabrication of the first integrated subharmonic planar Schottky diode mixer raised several issues related to the infancy of the first mask design. In order to minimise the parasitic capacitance of the device, the 16 devices present on the sample were air-bridged using GaAs wet-etching as presented in Chapter 6. The first problem encountered was the poor adhesion of silicon dioxide on the GaAs. Fig. 7.9 illustrates this poor adhesion by showing the diffusion of the gold film between the GaAs and the silicon dioxide. Fig. 7.10 is another example and result of this poor adhesion showing the inhomogeneity of GaAs wet-etching during air-bridge step.

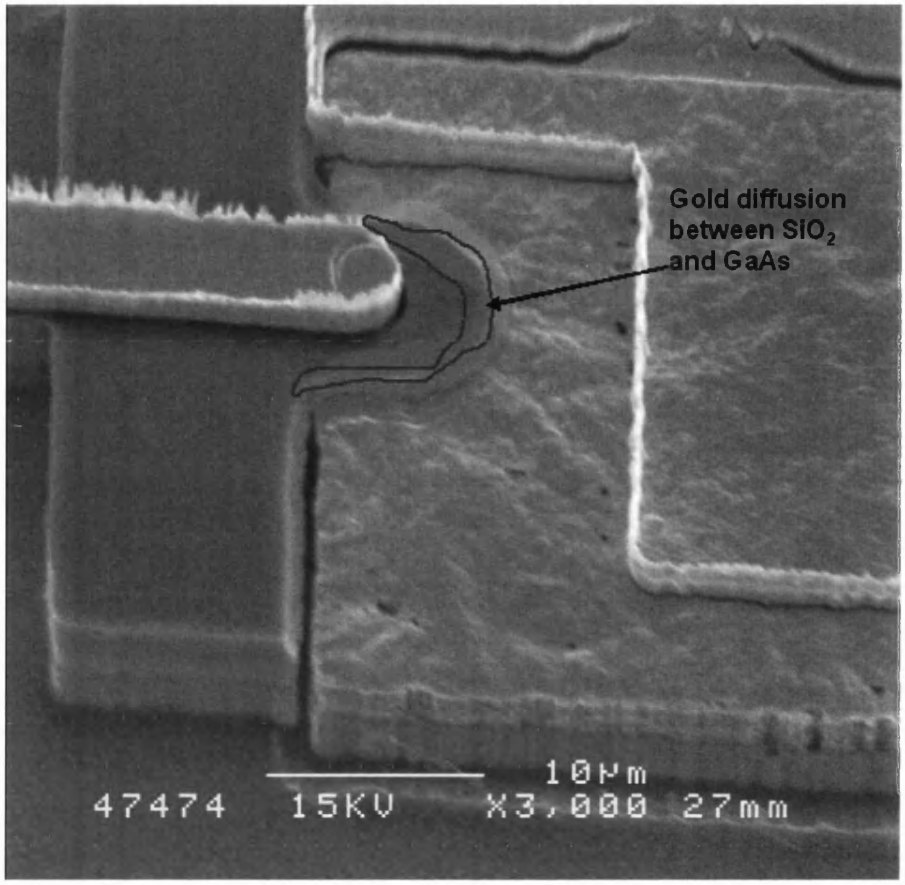

Fig. 7.9 Diffusion of ohmic contact between layer between SiO_2 and GaAs film.

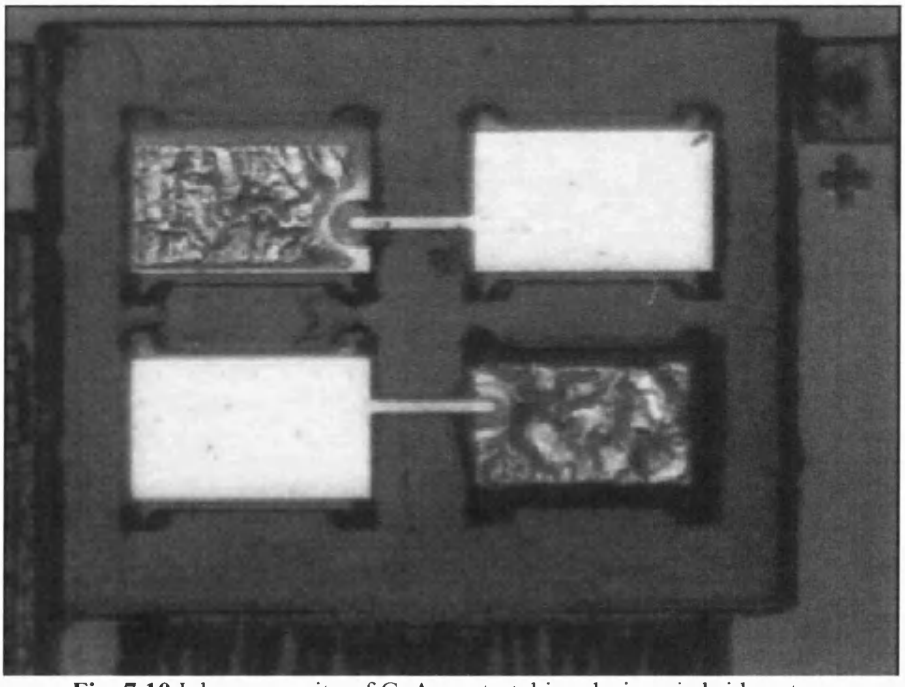

Fig. 7.10 Inhomogeneity of GaAs wet-etching during air-bridge step.

For this reason the capacitance of the device was monitored during the air-bridge step and wet-etching was stopped when the capacitance reached a minimum.

After being lapped-down, the devices were released from the mounting Crystal Bond glue and each chip individually cleaned using acetone and isopropanol. Next, a selected chip was mounted in the mixer block. Fig. 7.11 presents the mixer block and the different connections.

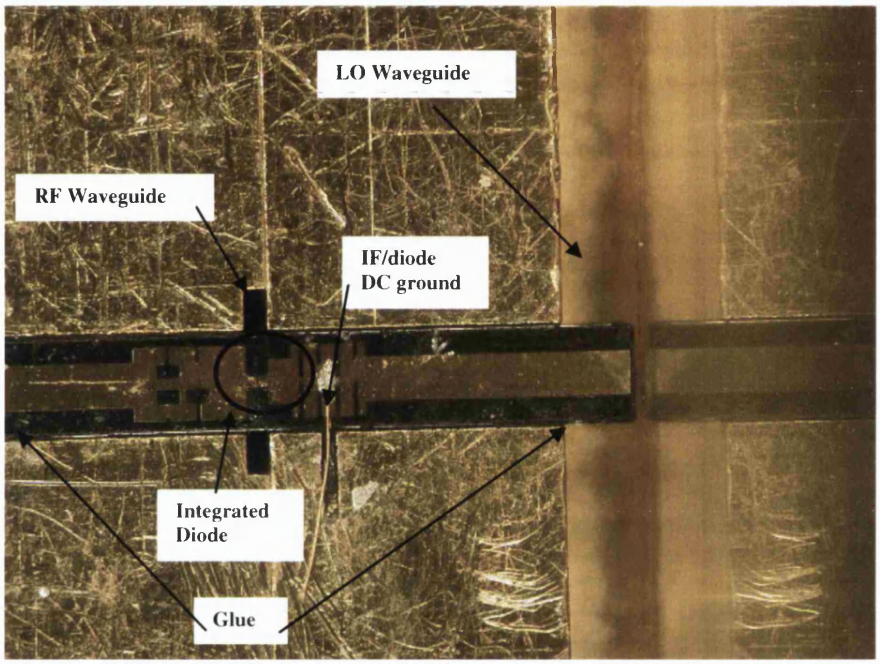

Fig. 7.11 Integrated SHP mixer in mixer block.

After release the samples exhibited a warpage of 50 µm. This warpage is believed to be caused by the stress on the deposited SiO_2 and different thin film metals. During a visit to the Jet Propulsion Laboratory, Peter Siegel confirmed that integrated membrane devices with a thickness of 5 to 10 µm were possible with a good control of film stresses. Due to the warpage on the device, each end had to be glued to keep the device flat inside the cavity. The device was also connected to the SMA connector using wire bond connection and conductive epoxy. As presented in Chapter 6 a GaAs stub was designed to provide a DC. Unfortunately, an excess under-etch occurred during air-bridge resulting in a deteriorated stub making it difficult to use. For this reason a wire bond connection was used to ground the device using conductive epoxy. The conductive epoxy was thermally cured at 90 °C in an oven for 30 min. Fig. 7.12 shows the device in the mixer block.

The DC measurements of the device are presented in Table 7.4 and Fig. 7.12. These measurements were made directly from the SMA connector, therefore including the filter resistance in the diode characteristics. These values indicate very good devices when compared to recent reported values for antiparallel Schottky diodes by VDI [7.8].

Integrated Mixer device	A_d (μm)	t_e (μm)	N_d (cm-3)	Φ_b	η	R_s (Ω)	I (V)	C_{j0} (fF)	C_T (fF)
UB-ID-A2_Diode1	1.5	0.3	$4x10^{17}$	0.81	1.27	18.4	$2.3.10^{-14}$	1.86	7
UB-ID-A2_Diode2	1.5	0.3	$4x10^{17}$	0.83	1.26	15.6	$4.7.10^{-14}$	1.86	9

Table 7.4 Comparing DC characteristics of some state-of-the-art Schottky diodes.

RF measurements were performed on this integrated subharmonic mixer. The WR-10 local oscillator waveguide was connected to a 92-98 GHz Gunn diode delivering up to 10 mW of RF power. The WR-5 signal waveguide was connected to a classic 200 GHz feed horn antenna. The RF signal was provided by a black body radiator. The system noise temperature was measured using the Y-factor method, alternating between room temperature and 77 K the black-body load in front of the feed horn.

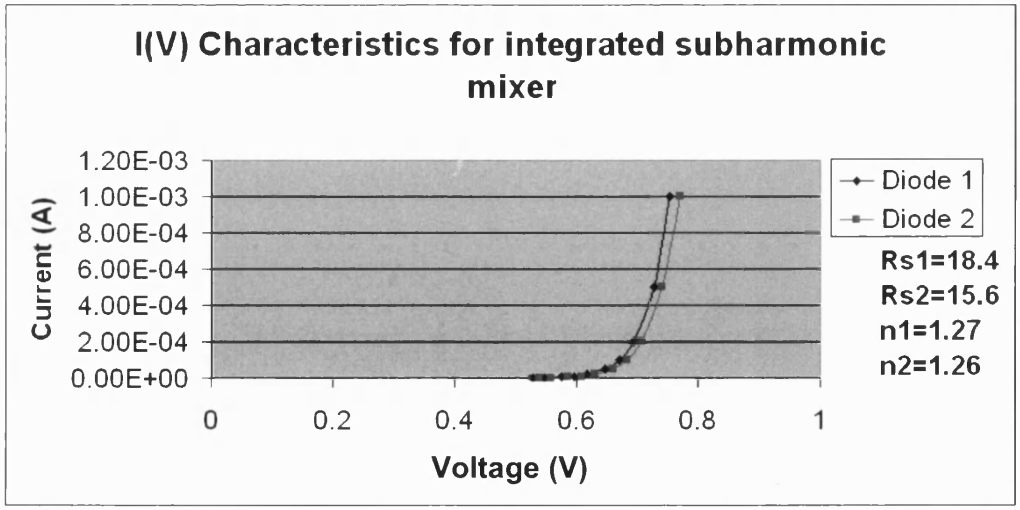

Fig. 7.12 I(V) characteristics of antiparallel pair diode integrated with mixer circuit.

Although it was possible to detect changes in the IF output when the mixer was operating, these changes were too small to be measured reliably. After investigation on the different parts of the mixer block it was found that the RF and LO backshorts had been damaged, which could cause serious problems with coupling of the signal and local oscillator power. A second reason for the weak signal measurements was potentially due to a problem with the filter pattern. In order to reduce the series resistance of the diode as well as reducing the resistance due to skin effect, it was decided for the final device to evaporate 1 μm of gold during the finger and filter fabrication. This long and thick evaporation was carried out using a thermal evaporator. Due to the long time required to evaporate the gold, the evaporation chamber rose to a temperature close to 140 °C, which caused some deterioration of the resist, making it extremely difficult to perform the lift-off. The low-pass filter was for this reason not perfectly defined and would have resulted in leakage of the RF signal as well as the local oscillator signal. Fig. 7.13 shows the damaged LO backshort and Fig. 7.11 and Fig. 7.13 the low-pass filter not correctly defined.
A second batch of devices was fabricated and the temperature was kept below 100 °C during the thermal evaporation by allowing the chamber to cool down every 25\0 nm of gold deposition. Two new backshorts have been ordered and the Terahertz group is planning to measure the device.

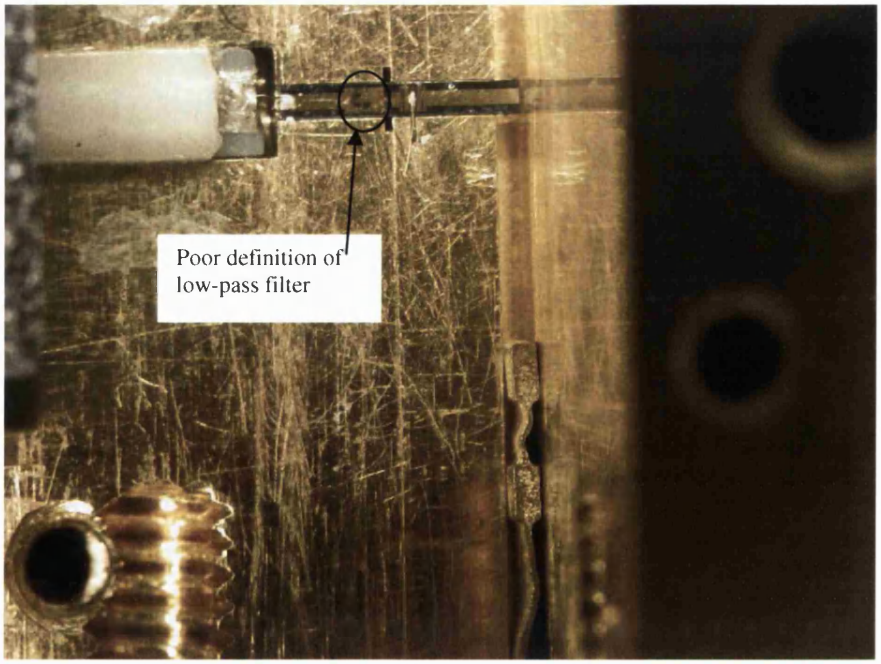

Fig. 7.13 Different encounter problem on mixer block and low-pass filter.

7.3 Measurements on the fixed-tuned integrated Subharmonic Mixer

The fabrication steps for the fixed-tuned integrated mixer were described in Chapter 6. A large part of those measurement were done at the Rutherford Appleton Laboratory with great help from Bertrand Thomas.

The DC characteristic of the anti-parallel integrated diodes fabricated during this work are presented in Table 7.5. These characteristics represent the typical values found across the 32 devices present on chip. Out of the 64 diodes (2x32 antiparallel diodes) only a few were not working. All these measurement were performed after air-bridge etching and by probing directly onto the diode pads located on top of the mesa. Fig. 7.14 shows the 40 devices (including 8 test structures). The devices were processed on a 1cm by 1.5 cm GaAs chip.

Integrated Mixer device	A_d (μm)	t_e (μm)	N_d (cm-3)	η	$R_s(\Omega)$
MB16_Diode1	1	0.3	$4x10^{17}$	1.21	17.5
MB16_Diode2	1	0.3	$4x10^{17}$	1.21	13.6
MB16_Diode1	2	0.3	$4x10^{17}$	1.19	14.4
MB16_Diode2	2	0.3	$4x10^{17}$	1.17	17.49

Table 7.5 Typical Diode DC characteristics for the fixed-tuned integrated mixer.

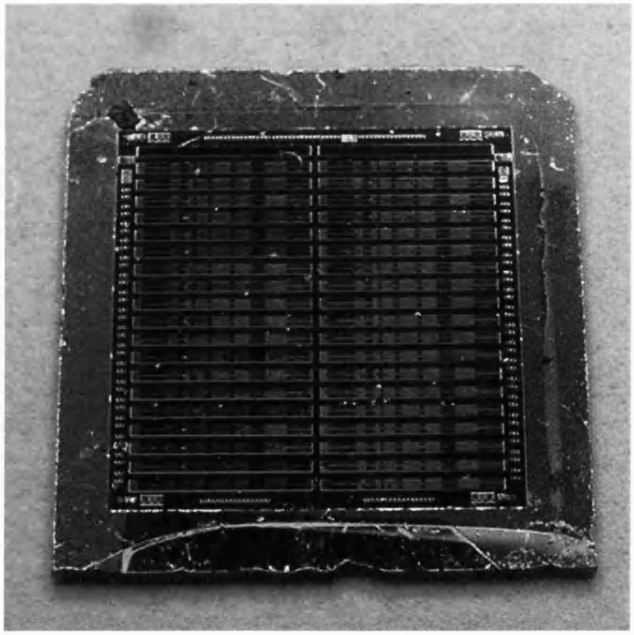

Fig. 7.14 Full GaAs chip consisting of 32 integrated mixers.

Due to the reduced length of the chip compared to the integrated mixer presented in section 7.2, less warpage was found on the fixed-tuned (F-T) mixer device. This made the assembly of the chip in the mixer block easier. The IF and DC ground for this device was design to be located at the end of the device opposite to the SMA connector. This connection was made using conductive glue (Fig. 7.15).

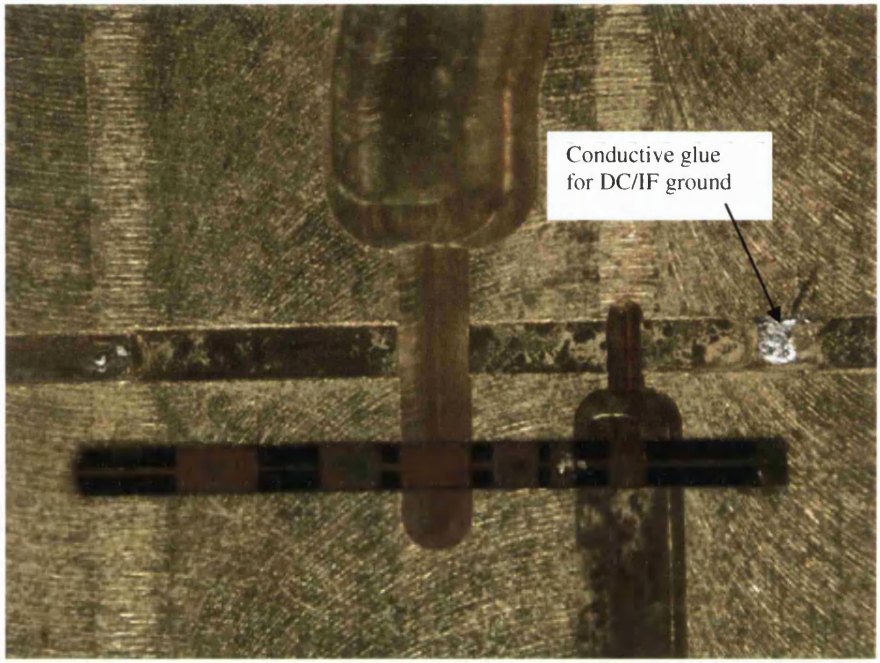

(a)

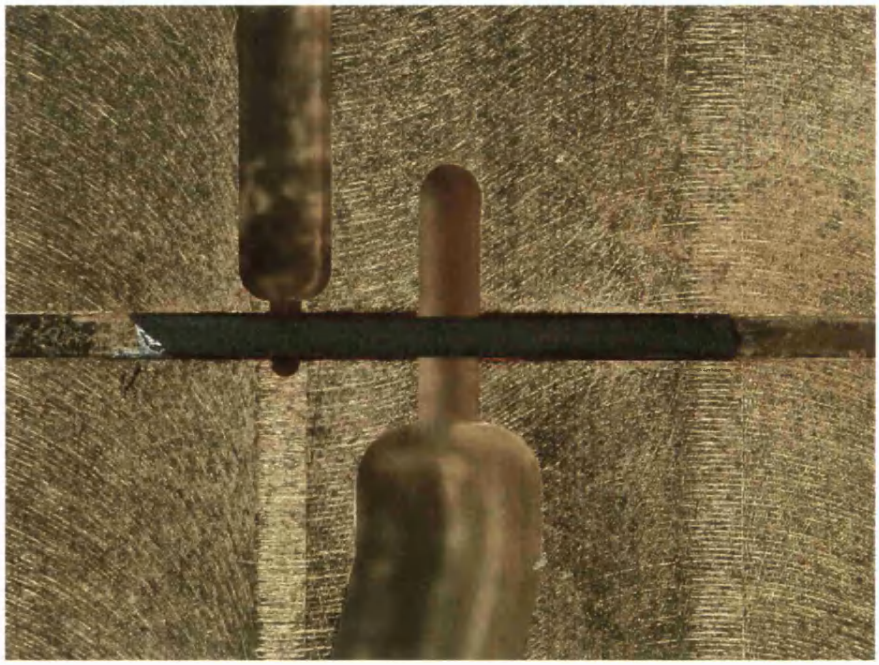

(b)

Fig. 7.15 (a) shows the F-T mixer before being flipped in the channel, (b) shows F-T inside the channel.

The IF connection output was connected to a quartz substrate providing a microstrip transmission line to connect to the K-connector (Fig. 7.16).

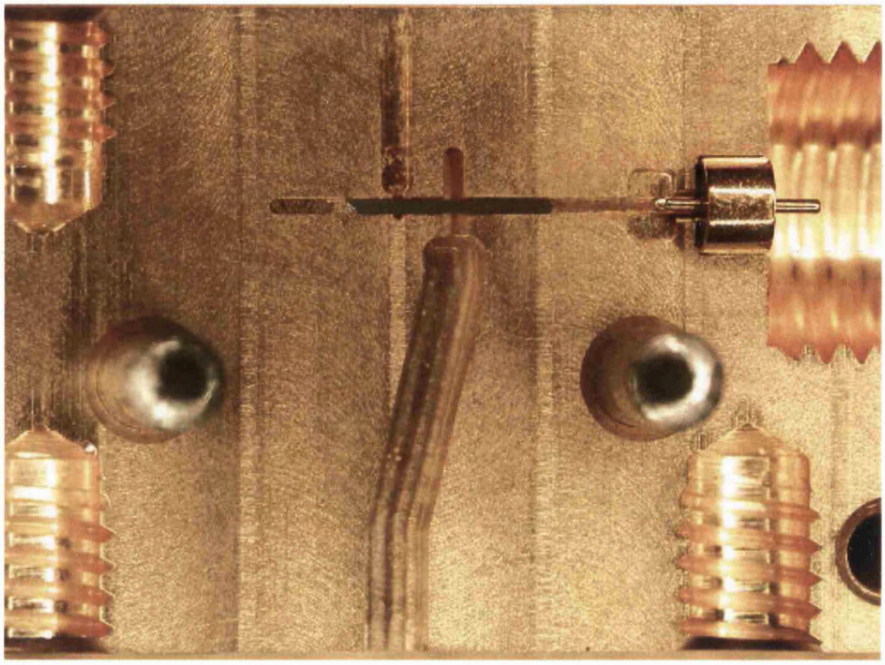

Fig. 7.16 Complete integrated fixed-tuned circuit mounted in mixer block and connected to IF K-connector.

The mixer circuit was measured at DC directly from the K-connector. During those measurements it was found that the device had a different response than the measurements under probe station. By inspecting the device under an SEM it was found that the device had suffered under-etching in the region of the slope connecting the filter to the mesa (Fig. 7.17).

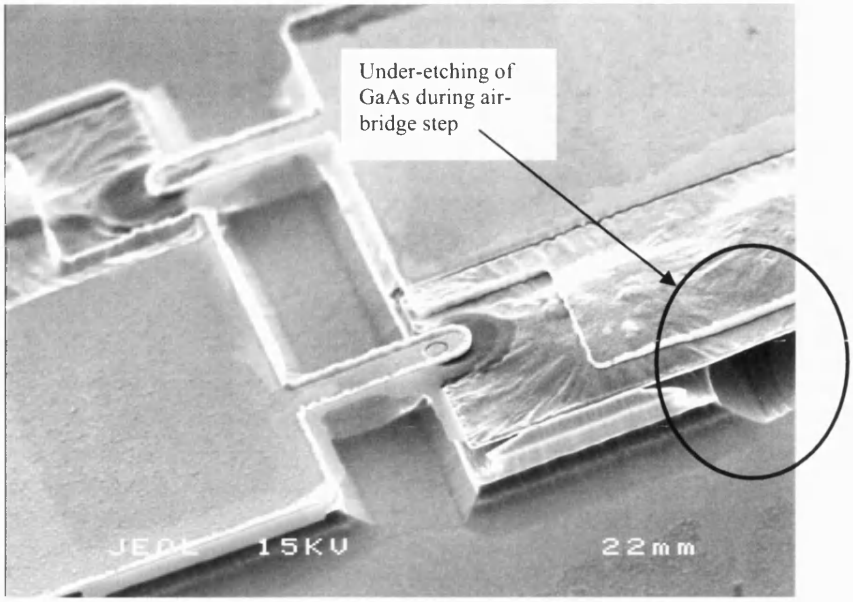

Fig. 7.17 Complete integrated fixed-tuned circuit mounted in mixer block and connected to IF K-connector.

The I(V) characteristic of the device showed an open circuit going from each end of the filter. The problem was partially solved by applying conductive glue on each side of the mesa to fix this discontinuity.

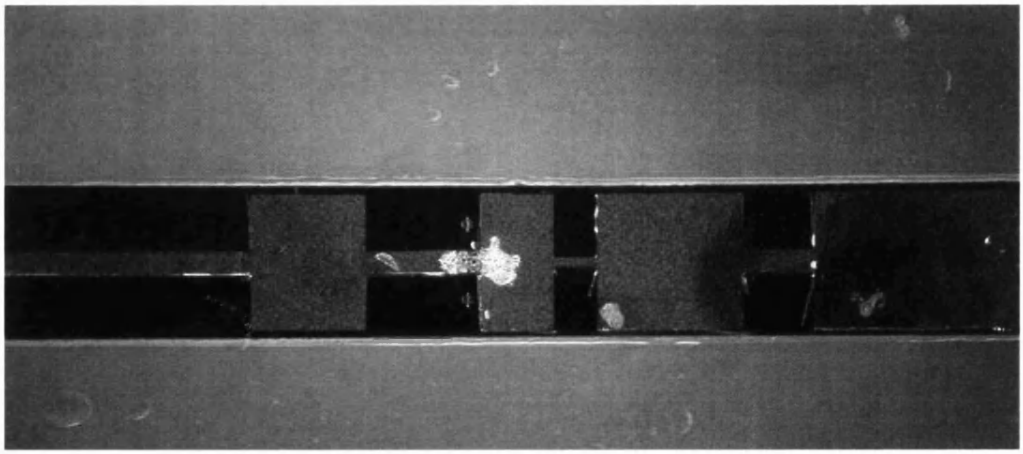

Fig. 7.18 Integrated fixed-tuned mixer circuit with conductive glue on each side of mesa.

Fig. 7.18 shows an integrated fixed-tuned device with the conductive glue on each side on the mesa. The I(V) characteristics was measured after baking the conductive glue (Fig. 7.19). The open circuit problem was fixed using the conductive glue, but the circuit presented a large series resistance for one diode.

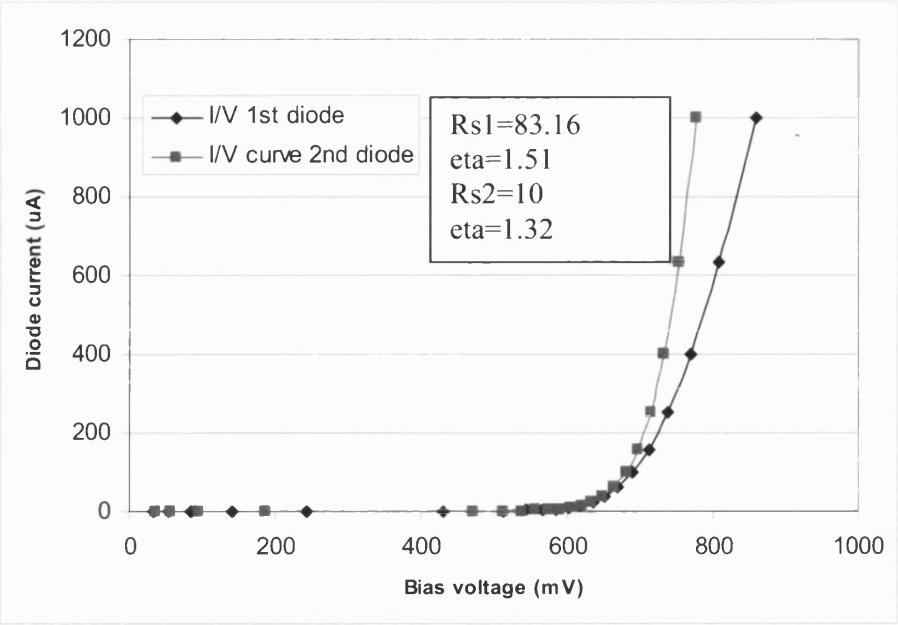

Fig. 7.19 Plot of the I(V) characteristic of the diode after fixing the discontinuity.

The system noise temperature of the integrated fixed-tuned mixer was measured using the Y-factor method presented in section 7.1. Fig. 7.20 shows the mixer block including the RF feed horn, and Fig. 7.21 the RF measurement set-up.

The DSB measurements function of frequency are presented in Fig. 7.22. The results show a minimum system conversion loss of 8900 K at 179 GHz. This large noise response was due to the high series resistance of one of the device after fixing the discontinuity.

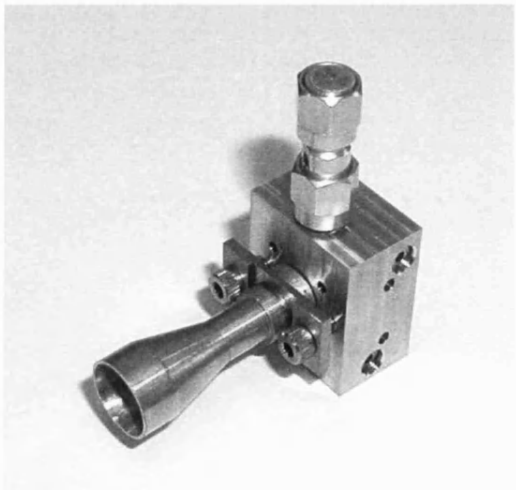

Fig. 7.20 183 GHz fixed-tuned subharmonic mixer block.

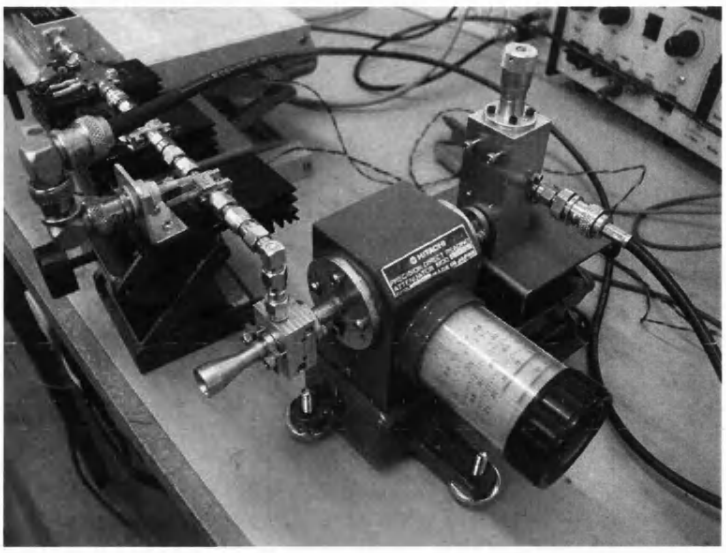

Fig. 7.21 RF measurement set-up.

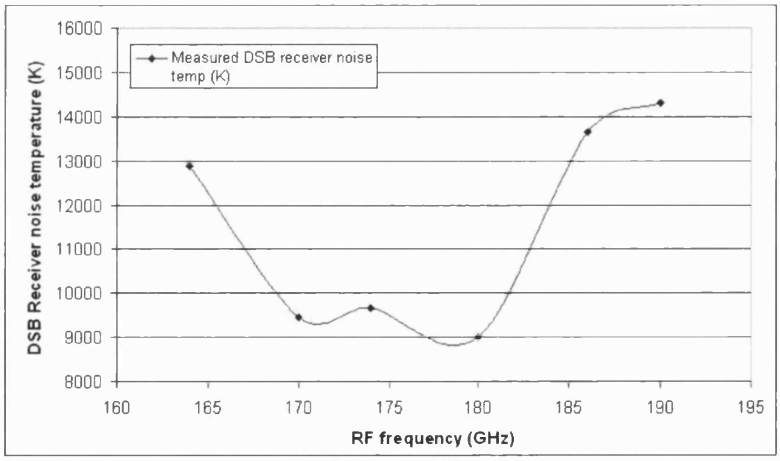

Fig. 7.22 DSB measurement of the integrated subharmonic fixed-tuned mixer.

References – Chapter 7

[7.1] Private conversation Dr. Alex Margomenos

[7.2] I. Mehdi, P. Siegel, M. Mazed, "Fabrication and characterization of planar integrated Schottky devices for very high frequency mixers," High Speed Semiconductor Devices and Circuits, *Proceedings IEEE/Cornell Conference on Advanced Concepts*, 2-4 August 1993, pp. 94-102.

[7.3] S. M. Marazita, *et al.*, "Integrated GaAs Schottky mixers by spin-on-dielectric wafer bonding," *IEEE Transactions on Electron Devices*, vol. 47, no. 6, pp. 1152-1157, June 2000.

[7.4] I. Mehdi, *et al.*, "Planar GaAs Schottky diodes integrated with quartz substrate circuitry for waveguide subharmonic mixers at 215 GHz," *Microwave Symposium Digest*, IEEE MTT-S International, vol. 2, WE2E-5, 23-27 May 1994, pp. 779-782.

[7.5] C. A. St. Jean, *et al.*, "Novel fabrication of Ti-Pt-Au/GaAs Schottky diodes," *IEEE Transactions on Electron Devices*, vol. 47, no. 7, pp. 1456-1468, July 2000.

[7.6] I. Papapolymerou, *MMIC passive and active structures*, Ph.D. thesis, University of Michigan, 1999

[7.7] C-I. Lin, *et al.*, "Planar Schottky diodes for submillimeter wave applications," *Terahertz Electronics Proceedings*, IEEE Sixth International Conference, 3-4 September 1998, pp. 135-138.

[7.8] B. Thomas, *Etude et réalisation d'une tête de réception hétérodyne en ondes submillimétriques pour l'étude des atmosphères et surfaces de planètes*, Ph.D. Thesis, University Paris 6, 2004

[7.9] N.R. Erickson, "A fast and sensitive submillimeter waveguide power meter," in *Proc. 10th Int. Symp. Space THz technology,* Charlottesville, SC, 1999, pp. 501-507.

[7.10] D. M. Pozar, "Microwave engineering," John Wiley and Sons Inc., New York, 1998.

[7.11] Stephen A. Maas, " Microwave mixers ", Artech House Inc., 1986

Chapter 8

Summary and Discussion

8.1 Overview

The demand for submillimetre-wave mixers has been steadily increasing not only for the traditional scientific applications such as radio astronomy and atmospheric remote sensing, but also for a wide range of potential military and commercial applications such as compact range radar, ultra broad band and secure communications, medical diagnostics, remote detection of battlefield toxins and collision avoidance systems for ground vehicles and aircraft. Several approaches have been developed and many successful mixers have been built in this frequency range in the past 20 years. However, they all suffer one or more drawbacks, such as high cost, low reliability and repeatability, lengthy and difficult fabrication and assembly, poor sensitivity, narrow bandwidth and reliance on mechanical tuners. At the University of Bath our goal is to develop a terahertz technology base that avoids all of these problems. Thus, we strive to make the terahertz frequency band as useful for scientific, military and commercial applications as the microwave and infrared bands are today.

There are three recent innovations that are being used to make this goal a reality.

1) The development of very advanced and commercially available computer aided design tools suitable for simulating both the linear and nonlinear parts of the submillimetre-wave circuits.

2) The development of easy and reliable processes to fabricate high quality Schottky diodes to operate up to THz frequencies

3) The development of integrated Schottky diode technologies that allow enhanced performance, reliability and repeatability.

The primary goal of this dissertation has been to use these three innovations to advance the state-of-the-art of submillimetre-wave mixers. Although, the primary research emphasis has been to integrate Schottky diodes for fixed-tuned mixers, significant work has also been performed on the circuit design of subharmonic

mixers and on the optimisation and development of a reliable and high yield process to fabricate state of the art Schottky diodes.

In the area of Schottky diode fabrication the primary contributions have included:

1) The development and demonstration of a process capable of producing state of the art Schottky diodes with an extremely high yield.

2) The demonstration of a 183 GHz fixed-tuned subharmonic mixer using the antiparallel flip-chip diodes developed during this research.

In the area of diode integration the primary contributions have included,

3) The design and modelling of a first integrated mixer with different RF circuit geometry.

4) The development of a process to integrate the Schottky diode on a thin GaAs substrate

5) The fabrication, assembly and testing of a 200 GHz integrated mixer.

6) The design, modelling and fabrication of 183 GHz fixed-tune integrated mixer.

The remainder of this chapter will describe the contributions of this research in somewhat greater details and summarise the goals of future research.

8.2 Summary of Research Accomplishments

8.2.1 Antiparallel Schottky diodes

A variety of processes have been developed during this research to enable the fabrication of submicron Schottky diodes. A e-beam lithography process was developed to open vias of a diameter of 0.5 μm to 1 μm. In order to keep the small feature size a successful dry etch process was developed to etch silicon dioxide using PMMA e-beam resist as an etching-mask. The process showed enough selectivity to dry-etch 0.5 μm of silicon dioxide using a double layer of PMMA resist.

A number of deposition methods were attempted in developing Schottky diodes with low ideality and low series resistance. Diodes made with sputtered tungsten anodes (section 5.2.1) gave fairly good performance and high homogeneity and yield. A second advantage found using the tungsten sputtered diode was high thermal stability of the diodes. It is believed that further work concentrated on sputtered tungsten anodes with thicker tungsten deposition and thicker gold capping layers could equal or exceed their evaporated refractory counterparts. Electroplated platinum anodes

(section 5.2.2) gave promising results but could not deliver the uniformity and yield needed for this project. With improved electroplating equipment some of these problems could be alleviated but the yield and thermal stability of the I/V characteristics of these devices was also of concern.

Evaporated titanium anodes presented in section 5.2.3 with thick gold capping layers proved to produce the best all-round diodes. Processing recipes were fine tuned to give low ideality, low series resistance essential for efficient high frequency mixing. As the thickness of the gold capping layer seemed to have a direct effect on the properties of the diode (i.e. R_s) it is believed that an electroplated gold layer > 1 um may increase the performance of these devices further. Furthermore, the e-beam evaporator which was used for many different metals by several users made the reproducibility of good series resistance and low ideality more difficult.

Poor adhesion at the SiO_2/GaAs interface produced many problems during processing and the failure of many devices. During GaAs wet-etching on the air-bridge step, it was fund that the poor adhesion of the SiO_2 with GaAs produced diodes with a large under-etch. These effects were compensated with sample dehydration, adhesion promoter, and post baking the resist. But different type of passivation layer such as Silicon Nitride could be tested to improve this adhesion along with low pressure chemical vapor deposition (LPCVD).

Measured diode DC characteristics gave excellent correlation with predicted parasitic capacitance values modelled in Chapter 4. Diodes produced in this work were comparable to those of other leading research groups. Schottky diodes fabricated during this project were tested at in a Rutherford Appleton Laboratories subharmonic mixer at 183 GHz. A system noise temperature of 1350 K DSB and a mixer conversion loss of 7.5 dB DSB were measured using 5 mW LO power. The Schottky diode fabricated during this project gave comparable performance than commercial UMS diodes. It is interesting to note that the UMS diodes are not commercially available with antiparallel configuration. The diodes are fabricated in series and had to be diced and put in an antiparallel configuration on the quartz substrate. This step requires time and skills. Furthermore the commercial Schottky diode chips have a thickness of 100μm restricting the diode operation to ~110 GHz. For this reason the UMS diodes used in this mixer block were thinned down to a thickness of 30 μm. These measurements have demonstrated ease of use and the excellent quality of the Schottky diodes fabricated during this project for applications in the sub-millimetre

region. Following these results the company Radiometer Physics GMBH (RPG) also tested few diodes to establish future collaboration. RPG reported results of 950 K DSB system noise, 700 K mixer noise and 6 dB conversion loss at 150GHz. The diodes also proved to be robust and insensitive to large LO power.

8.2.2 First Integrated Subharmonic mixer

Following the good mixer performance of the antiparallel flip-chip diodes developed during this research, an integrated subharmonic mixer was designed and modelled. Linear and nonlinear modelling circuits have been developed (section 4.2) to predict the conversion loss of the first integrated mixer. SSB minimum conversion loss of 9.6 dB was predicted at a frequency of 178 GHz with an LO power of 4.6 mW and with a 10 % instantaneous bandwidth. The presence of a 3 μm membrane under the Schottky diode was modelled and was proved to increase by 16 % the instantaneous bandwidth.

The different process steps required to fabricate the integrated mixer were successfully developed and are presented in section 6.1.2. A major process step developed during this research was the development of a smooth dry etched GaAs. Etch rates using chlorine gas were good but the roughness results were unacceptable (see section 6.1.4). Using an appropriate mix of $SiCl_4$ and Ar, a dry etch recipe was developed and optimised by varying the RF power and pressure levels. An etching process resulting in mirror-like finishes to the GaAs etched surface was developed. One major parameter and limitation to the dry etching was the requirement to remain below a maximum temperature during plasma etching. Temperatures below 150 ^{o}C were required to avoid hard-baking the photoresist. For this reason, RF power levels had to be carefully selected to avoid this problem during the long etches (up to 3 hours).

A second major process step developed during this research was a release process achieved by a combination of front-dry etching and backside lap-down. The 30 to 50 μm front-side etching enabled us to lithographically define the size of the integrated device. Lapping down the substrate was a relatively straightforward task although care had to be taken during mounting and monitoring the sample planarity. When mounting the sample it was imperative that the backside sample surface was as parallel to the glass carrier as was possible to achieve. Levelling was achieved by heating the wax and applying physical downward pressure to high areas until the

surface profile varied by < 10 um. Etch rates while lapping varied widely and it was important to monitor the last few 100 um carefully. After lapping to a thickness of 50 μm, devices were found to have a small amount of bowing. This bowing could be reduced by a better control of the thin film stress during deposition.

Mounting the mixer circuit inside the mixer block was relatively quick and simple. The only difficulty was to deal with the bowing of the circuit. This bowing was solved by gluing each end of the device in the mixer mount.

The integrated mixer exhibited extremely low series resistance, low ideality and low parasitic capacitance. Unfortunately due to a poor RF back short, the determination of the conversion loss was not possible during this research. We have proved that successful integration of Schottky diode was possible and the diodes characteristics were unchanged following extra photolithography steps and long dry etching. We are planning to fabricate a new mixer block to test and publish a paper on this 183 GHz integrated subharmonic mixer.

8.2.3 Fixed-Tuned integrated Membrane Mixer.

A second generation of integrated subharmonic mixer was designed, fabricated and tested during this research. With the collaboration of LERMA, a suspended fixed-tuned mixer was designed. A combination of linear and non-linear optimisation, using respectively HFSS and ADS, was performed to optimise the diode geometry, filter design, RF and LO E-probe as well as the overall embedding impedance seen by the diode. The performances were computed over the frequency range 160-200 GHz (section 4.3). The expected SSB conversion losses were found to be better than –7 dB between 160 and 196 GHz using 2 mW of LO power, with a best value of –6.1 dB at 183 GHz. Considering additional losses of about 2 dB due to the total conductor and dielectric loss of the horn and waveguide, as well as possible mismatches between the IF output of the mixer and the first IF low noise amplifier, the DSB mixer conversion loss was expected to be approximately 5.1 dB at 183 GHz. The fabrication step used to fabricate this new device had to be redefined to allow the RF passive circuit to lay on the semi-insulating GaAs, reducing potential parasitics capacitance as well as propagation of unwanted modes. The transition between the filter and the mesa were achieved using the GaAs [111] plane as described in Chapter 6. Two complete batches of devices were fabricated during this research and diode characteristics of the devices were measured.

Extra under etching was found during the final step of fabrication of the device around the mesa structure. This mesa under etching of the devices during the air channel formation was a product of mask design infancy and poor adhesion at the SiO_2/GaAs interface. This issue made it difficult to correctly form the air-bridge for the integrated device as well as keeping a good electrical transition between the circuit and the mesa. This problem could be resolved by either improving the passivation adhesion or implementing a new mask with large protection for the diode mesa structure.

The transition between the circuit and the diode-mesa structure was re-established by applying epoxy glue (Chapter 7). This fix proved to give limited results and high series resistance was found remaining on the tested device.

Bertrand Thomas designed and fabricated the mixer block used to measure the fixed-tuned subharmonic mixer. Although measurement did not produce the expected conversion loss and noise temperature simulated due to high series resistance, the device proved to be mixing and showed potential for a new type of device.

8.3 Suggestions for Future Work

The main accomplishment of this research has been the development and demonstration of the integration of state of the art Schottky diode on a GaAs RF circuit micromachining process to fabricate MMIC like device at 200 GHz.

However, some work needs to be done to improve the quality of the passivation film on GaAs. A better film will allow better control on the adhesion on GaAs and consequently better control of the air-bridge wet-etch step, which was found to be a major problem during this research.

Next, this work could be extended to more complex circuits and devices working at frequencies up to 600 GHz. Those devices working at higher frequency would be easily achieved by scaling down the different parts of the circuit using the HFSS and ADS layout used during this research. Not all elements of the mixer could be scaled and optimising would be needed for values such as diode anode area and effective backshort position.

Furthermore the integrated circuit could also be extended to improve component assembly. The incorporation of a beam lead technology would eliminate the need to attach bond wires to the fragile substrate and would also improve alignment and

minimum wire dimension. With such a beam lead technology the component assembly process would consist of the placement of the integrated circuit into the microstrip channel and the "snapping together" of the two block halves. This would be a major advantage.

Finally, further integration could include the combination of components, such as mixers and multipliers, on a single GaAs chip. The objective of this would be to integrate a source, multiplier and mixer on a single chip potentially reducing RF losses between components.

While some work remains, the path is now clear for the development of terahertz components that not only yield excellent performance but are also practical for the full range of scientific, military and commercial applications that can be envisioned.

Acknowledgements